博士論文

Hydrogen storage properties of Metal-Boron-Hydrogen system

金属ホウ化物を用いた金属-ホウ素-水素系複合物質における水素貯蔵特性

中川　鉄水

広島大学大学院先端物質科学研究科

2009 年 3 月

主論文

Abstract

The *M*-B-H systems are composed of metal, boron, and hydrogen as elements. Among them, many metal borohydrides $M(BH_4)_n$ store larger amounts of hydrogen than 5 mass% but complete rehydrogenation of $M(BH_4)_n$ is quite difficult because of their slow kinetics. However, some mixtures of metal hydride $M'H_m$ and $M(BH_4)_n$ are quite easily rehydrogenated compared with $M(BH_4)_n$ itself. The $M'H_m$-$M(BH_4)_n$ mixtures form metal boride $M'B_m$ with metal hydride MH_n during the dehydrogenation reaction. Until now, the mechanism which describes how $M'B_m$ is formed during dehydrogenation reaction and why rehydrogenation reaction of the $M'H_m$-$M(BH_4)_n$ mixtures are easily proceeded when $M'B_m$ exists have not been clarified yet. In this thesis, hydrogen desorption properties of the $M'H_m$-$M(BH_4)_n$ mixtures and hydrogen storage properties of the MH_n-$M'B_m$ mixtures which were milled under hydrogen pressure were investigated in order to obtain the guiding principle of material design. The results obtained in this thesis summarized as follows;

1. The $M'H_m$-$LiBH_4$ (M' = Mg and Ca) mixtures formed $M'B_m$ and LiH during the dehydrogenation reaction at 450 °C under ~0.5 MPa H_2 pressure but did not form $M'B_m$ under inert gas condition. In the case of the MgH_2-$LiBH_4$ mixture, the melting phenomenon of $LiBH_4$ and the decomposition reaction of MgH_2 occurred before forming MgB_2. In the case of the CaH_2-$LiBH_4$ mixture, the melting phenomenon of $LiBH_4$ occurred but CaH_2 did not decompose before forming CaB_6. In addition, $LiBH_4$ did not decompose at 450 °C under ~0.5 MPa H_2 pressure. From these results, it was clarified that the solid-liquid reaction between solid $M'H_m$ (M'

= Mg and Ca, m = 0 and 2, respectively) and liquid $LiBH_4$ proceeded by suppressing the decomposition reaction of $LiBH_4$ during the dehydrogenation reaction to form $M'B_m$. From a thermodynamic point of view, $M'B_m$ should be formed after the dehydrogenaiton reaction under inert gas condition. Therefore, the existence of hydrogen would change the reaction path of forming MgB_2 into the reaction between Mg and $LiBH_4$ from the reaction between Mg and B. However, MgB_2 was not formed by the reaction between MgH_m (m = 0 and 2) and $Zn(BH_4)_2$. This reaction consists of two elementaly steps, which are formation of B_2H_6 emitted from $Zn(BH_4)_2$ and the gas-solid reaction between B_2H_6 and MgH_m (m = 0 and 2) proceeded thereafter. Therefore, the condition of forming $M'B_m$ would be; (1) to suppress the decomposition the $M(BH_4)_n$ by hydrogen pressure, (2) to accelerate the diffusion of B by existence of liquid phase of $M(BH_4)_n$, and (3) no B_2H_6 emission from $M(BH_4)_n$.

2. The hydrogenation reactions of the MH_n-$M'B_m$ (M = Li and Sc, M' = Mg and Ca) mixtures proceeded by milling at room temperature under hydrogen pressure. All the as-milled MH_n-$M'B_m$ mixtures had B-H bonding. The as-milled LiH-MgB_2, ScH_2-MgB_2, LiH-CaB_6, and ScH_2-CaB_6 mixtures desorbed 3.6, 3.4, 1.9, and 1.8 mass% of hydrogen, respectively by heating in TG. They desorbed larger amount of hydrogen than the as-milled MgB_2 (3.1 mass%) and CaB_6 (1.7 mass%), which were milled under the same conditions as the MH_n-$M'B_m$ mixtures. This result indicates that MH_n would have an ability to provide hydrogen to $M'B_m$. For the as-milled LiH-$M'B_m$ (M' = Mg and Ca) mixtures, their hydrogenation reactions did not completly proceed, so a longer milling time or higher temperature would be

required to obtain a complete hydrogenated samples. For the as-milled ScH_2-$M'B_m$ (M' = Mg and Ca) mixtres, it was clarified that ScB_2 and "M'-B-H" compounds (M' = Mg and Ca), which has B-H bonding, were generated in both the samples by milling. From these results, it was found that the "M'-B-H" compounds desorbed hydrogen from the B-H bonding, while ScB_2 does not react with any materials. Finally, it is suggested that MH_n would have an ability to provide hydrogen to $M'B_m$ and hydrogen is stored in the MH_n-$M'B_m$ mixture by forming B-H bonding during milling under hydrogen pressure.

Acknowledgements

I would like to express my sincere thanks and appreciation to my supervisor Prof. Dr. Yoshotsugu Kojima for his helpful guidance, suggestion and encouragement throughout the course of this work.

I would like to express my special thanks to Associate Prof. Dr. Takayuki Ichikawa for a lot of valuable suggestion and discussion in my doctoral course life.

I am much obliged to my co-prompters Prof. Dr. Toshiro Takabatake, Prof. Dr. Tamio Oguchi for useful suggestion and discussion.

I would like to my special thanks to Guest Prof. Dr. Hironobu Fujii and Guest Prof. Dr. Etsuo Akiba for their helpful guidance and suggestion for my work.

I am very grateful to Dr. Tetsuo Homma in Japan Synchrotron Radiation Research Institute (JASRI) in SPring-8 for performing the X-ray absorption spectroscopy in Spring-8 and useful discussion, and I am much obliged to Mr. Shinji Michimura in Prof. Takabatake's laboratory for preparing a sample of scandium diboride ScB_2.

Finally, I would like to express my sincere thanks to the colleagues of Prof. Kojima's laboratory, Dr. Masami Tsubota, Dr. Hiroki Miyaoka, Dr. Paik Biswajit, Dr. Matin Md. Ruful, Mr. Satoshi Hino, Mr. Kyoichi Tange, Mr. Taisuke Ono, Mr. Kosei Nakamura, Mr. Toru Kimura, Ms. Chie Oomatsu, Akira Kubota, Hikaru Yamamoto, and the old colleagues in Prof. Fujii"s laboratory for their useful discussion and valuable help, and I would like to express my special thanks to Ms. Misao Mukouda and Yoko Tamai for their support for my doctoral course life.

Contents

1 Introduction

1-1 Hydrogen storage for energy systems

1-1-1 Hydrogen energy

At present, it is a global challenge to reduce the amount of atmospheric carbon dioxide CO_2. The CO_2 gas is produced by industrial activities and driving car, and would cause greenhouse effect. The Kyoto Protocol was adopted in 1997 under the United Nations Framework Convention on Climate Change (UNFCCC) to reduce the greenhouse gases and 183 states have already ratified as of October 16, 2008 [1-1]. In addition, Albert Arnold Gore, Jr. and the UN's Intergovernmental Panel on Climate Change were awarded the Nobel Peace Prize in 2007 "for their efforts to build up and disseminate greater knowledge about man-made climate change, and to lay the foundations for the measures that are needed to counteract such change" [1-2]. This fact indicates that activity for tackling environmental issues, especially decreasing the CO_2 amount, is regarded as a peace operation. For the target of this kind of activity, many governments aim at "Carbon Neutral" in the world, which means producing net zero carbon (CO_2) emissions by balancing or offsetting carbon releases [1-3]. In Japan, the government aims at "low carbon society", which means not merely the replacement of energy sources with less carbon intensive ones but energy conservation as well [1-4]. To reduce the amount of atmospheric CO_2, there are two kinds of activities. One is to increase the absorption amount by planting and "Carbon Capture and Storage" (CCS), which is storing captured and compressed CO_2 in deep geological formations, in deep ocean masses, or in the form of mineral carbonates. Second is to decrease the emission amount of CO_2 by exchanging fossil fuel to alternative and renewable energy resources.

The fossil fuel has another serious problem which is exhaustion. Even from this viewpoint, exchanging fossil fuel to alternative energy resources is a particularly acute issue.

Hydrogen energy is one of the candidates for the secondary energy to be efficiently converted from the alternative energies, such as solar power, hydroelectric, wind power, and ocean energy because it has some advantages as follows:

1) No pollution gas such as CO_2 and NO_x is essentially emitted from hydrogen in all processes when hydrogen is utilized by combustion engines or fuel cells.
2) Hydrogen energy is renewable because hydrogen can be produced by the electrolysis of water or the steam reforming of fossil fuels.
3) Hydrogen is a highly abundant element on earth although less than 1.0 % is existing as molecular hydrogen gas (H_2) and overwhelming majority of hydride (*e.g.* water (H_2O) in the ocean and hydrocarbons).
4) Hydrogen has the highest gravimetric energy density among all combustion fuels. For example, the lower heating value of hydrogen is three times as large as that of gasoline [1-5].
5) The storage and transportation of hydrogen is easier than electricity.

In addition, the establishment of the hydrogen energy system may cause stimulation of economic activities because several new big markets would be created by utilization of hydrogen. One of them is car market. The car companies would develop new cars, which are use for internal combustion system or fuel cell electric vehicle (FCEV).

For realizing the hydrogen energy system, several kinds of technologies have to be established, which are a hydrogen production, storing and transportation, and utilization.

1-1-2 Hydrogen storage and transportation

There are important factors for the hydrogen storage and transportation technique, *e.g.* compact, light weight, safe and low cost. Three potential techniques for the hydrogen storage are considered.

1-1-2-1High pressure hydrogen tank

The compressed hydrogen gas is introduced into a vessel. For onboard storage, the practicable vessel stores hydrogen at 35 MPa and the recent developed vessel can store at 80 MPa of hydrogen [1-6]. The important technique on this method is the production of suitable vessel, which is required to be compact, light weight, high resistance to hydrogen embrittlement and high strength for the hydrogen pressure. The vessels are designed to consist of three layers: (1) an inner polymer liner, (2) over wrapped with a carbon-fiber composite which is the stress-bearing component, and (3) an outer layer with an aramid-material capable towithstand mechanical and corrosion damage. The target that the global industry has set is a 70 MPa cylinder within a mass of 110 kg resulting in a gravimetric and a volumetric density of over 6 mass% and over 30 kg m^{-3}, respectively [1-6].

1-1-2-2Liquid hydrogen

Liquid hydrogen is high volumetric density of the system (70.8 kg m^{-3}) compared with that of the compressed hydrogen (30 kg m^{-3}) and gravimetric density of the system is more than 5 mass % at -253 °C. Liquid hydrogen can exist below the critical temperature (-241 °C), so the cryogenic vessel is kept at -253 °C under ambient pressure. The vessel should be open system in order to prevent the strong overpressure. Moreover,

it should possess a good thermal insulation in order to reduce the boil-off. A large vessel can suppress the boil-off rate because of its small contact area, so liquid hydrogen storage is suitable for mass transportation. However, in advance of liquefaction, conversion from ortho-hydrogen to para-hydrogen is required (normal hydrogen contains 25 % of para-hydrogen and 75 % of ortho-hydrogen at room temperature) because both the melting point and the boiling point of para-hydrogen are about 0.1 °C lower than those of normal hydrogen [1-6]. Ortho-hydrogen releases plenty of heat of ~1.4 kJ mol^{-1} by converting to para-hydrogen, and then the evaporation of liquid hydrogen is induced by conversive heat in case ortho-hydrogen remains in vessel at low temperature. The kinetics of this conversion reaction is too slow, therefore this reaction needs to be accelerated by using catalyst for production. The essential problem of the liquid hydrogen storage for the practical use is high liquefaction energy.

1-1-2-3Hydrogen storage material

Hydrogen storage material is most attractive method because the volumetric hydrogen density is higher than those of high pressure hydrogen and liquid hydrogen [1-5]. Hydrogen storage materials require the following properties for automotive applications.

- High hydrogen gravimetric capacity
- Suitable thermodynamic and kinetic properties, where its absorption/desorption reactions of the hydrogen storage material were controlled under moderate temperature and pressure
- Low cost and abundant resource
- Easy handling

Recently, some hydrogen storage materials are used for vehicle or other equipments [1-7] but no material satisfies all required properties. Therefore, in order to develop the performance of hydrogen storage materials, many investigations have been carried out all over the world.

The targets for hydrogen storage materials for vehicle are proposed by some organizations. Table 1 shows the targets of the New Energy and Industrial Technology Development Organization (NEDO) [1-8], U.S. Department of Energy (DOE) [1-9] and International Energy Agency (IEA) [1-10].

Table 1-1. Target for hydrogen storage materials for vehicle in each organization.

Properties	Units	NEDO	DOE*	IEA
Gravimetric density	mass% H_2	5.5	6.0/9.0	5.0
Operation temperature	°C	< 150	-20~50/-20~50	< 80
Cycle life-time	cycles	2,000	1,000/1,500	-
Target year	year	2007	2010/2015	2006

*Operating temperature of the system

1-2 Essential properties of hydrogen in metals

There are two important properties to improve the hydrogen storage material for practical use, which are thermodynamics and kinetics. In order to control those properties, understanding the mechanisms of the reaction, which are governed by the interaction between hydrogen and metals, is required.

1-2-1 Thermodynamics of hydrogen-metal reaction

The thermodynamics of the hydrogen-metal systems can be understood through the phase diagram. The phase diagram of the metal-hydrogen system is different from that of alloy and the composition of metal-hydrogen phases, and is a unique function of temperature and pressure of the surrounding H_2 gas. Thus, the equilibrium metal-hydrogen phase diagram is constructed from the Pressure-Concentration-Isothermal (PCI) curves as shown in Fig. 1-1 (a), which is obtained by isothermal measurements at several temperatures.

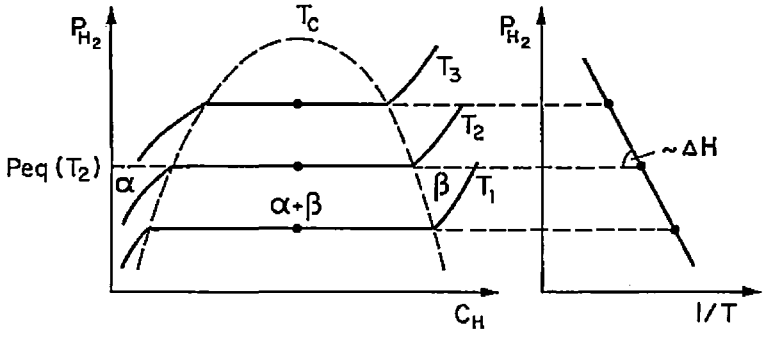

Figure 1-1. (a) PCI diagram and (b) van't Hoff plot [1-11].

In the first stage of hydrogenation which is low hydrogen concentration region shown as left-side slope in PCI curve (Fig 1-1 (a)). Hydrogen starts to dissolve in metal lattice with increasing hydrogen pressure, indicating appearance of the solid solution which is denoted by the α-phase. The crystal structure of the α-phase is almost the same as that of the host metal but its cell volume is expanded. In this region, hydrogen is successively absorbed in metal with increasing hydrogen pressure. The relation between hydrogen gas pressure and hydrogen concentration in this region is described by Sievert's law in the following equation,

$$\sqrt{P} = K_S x, \tag{1-1}$$

where P is hydrogen pressure, K_S Sievert's constant, x hydrogen concentration. This equation shows that the hydrogen concentration increases in proportion to the square root of hydrogen pressure in the low concentration region.

In the second stage which is the horizontal region on the PCI curves in Fig. 1-1 (a), a hydride, which is denoted as β-phase, is locally formed by the occupation of hydrogen in the interstitial sites and changing from the α-phase. When the β-phase is formed, the crystal structure of the host metal is generally changed by forming the bond between hydrogen and metal atoms. In this region, two phases of α- and β- coexists and hydrogen pressure has to be constant although the hydrogen concentration is continuously increased by growing of the β-phase. This phenomenon is described by the Gibbs phase rule in the following equation,

$$f = c - p + 2, \tag{1-2}$$

where f is the degrees of freedom, c and p are the number of components and phases in the system, respectively. In the case of $f = 1$, only one parameter among temperature, hydrogen pressure or concentration, can be chosen and all the rest are uniquely determined. Therefore, the hydrogen pressure as a function of hydrogen concentration in the isothermal condition is kept at constant pressure in the PCI measurement. This constant pressure is called as equilibrium (or plateau-) pressure P_{eq}. In the case of $f \neq 1$, no constant pressure region is appeared such as the low concentration region ($f = 2$) in Fig. 1-1(a). Moreover, all parameters are uniquely determined in the case of $f = 0$. When operation temperature is raised up, the plateau region is disappeared through the critical point T_c, above which the α-phase continuously transforms to the β-phase with increasing hydrogen concentration.

In the final stage which is the region over the plateau area, pressure is further raised and hydrogen concentration continues to increase until the limit. Absorbed hydrogen in this stage is dissolved to the hydrogen holes in the β-phase.

The slope and the width of the equilibrium plateau region are important for hydrogen storage applications. A flat plateau enables the reversible absorption and desorption of hydrogen in a metal and from a metal hydride, respectively, by controlling hydrogen pressure around P_{eq}. The width of the plateau region reveals the available amount of hydrogen. The hydrogen storage capacity depends on the relative thermodynamic stability of hydrogen in the host metal. The hydrogen absorption reaction to form the solid solution or a metal hydride phase is either exothermic or endothermic process, which can be understood by the enthalpy change ΔH. Here, ΔH is defined as a difference in relative stability between dehydrogenated and hydrogenated phases. This value can be directly estimated from the PCI diagram which is obtained by measuring equilibrium pressure at several temperatures as shown in Fig. 1-1 (b).

The thermodynamics for the formation of solid solution between hydrogen and metal can be described in the following way;

The reaction of metal or alloy (M) with gaseous hydrogen in the molar ratio of $x/2$ is expressed in the following reaction equation,

$$M + \frac{x}{2} H_2 \leftrightarrow MH_x . \tag{1-3}$$

Under equilibrium condition, the chemical potential of the molecular hydrogen gas, μ_g, is equal to the chemical potential of the hydrogen atoms in solid solution μ_α.

$$\frac{1}{2}\mu_g(T,p) = \mu_\alpha(T,p,x) . \tag{1-4}$$

Gaseous hydrogen can be considered as an ideal gas at relatively low pressures.

Therefore, the chemical potential of gaseous hydrogen can be described by calculating the partition functions Z_t, Z_r and Z_v for translational, rotational and vibrational motions, respectively, of ideal diatomic molecules, which is based on statistical thermodynamics as follows,

$$\mu_g(T,p) = kT\ln(Z_t \cdot Z_r \cdot Z_v) - E_d, \tag{1-5}$$

$$= kT\ln\left(\frac{p}{p_0(T)}\right) - E_d, \tag{1-6}$$

$$p_0(T) = \frac{16(\pi k)^{\frac{7}{2}} M_0^{\frac{5}{2}} r_0^2}{h^5} T^{\frac{7}{2}}, \tag{1-7}$$

where k is the Bolzman constant, E_d is the dissociation energy of a hydrogen molecule, M_0 is the mass of a hydrogen atom, r_0 is the distance between the hydrogen atoms, h is the Plank's constant, and $p_0(T)$ is the standard pressure which is generally considered as 1.03×10^5 Pa (~0.1 MPa) at -265.45 °C [1-12].

The chemical potential of the hydrogen atoms in metal is defined by the Gibbs free energy, which is expressed by enthalpy H_α and entropy S_α of the solid solution,

$$G(T,p) = H_\alpha - TS_\alpha, \tag{1-8}$$

where S_α is composed of excess entropy of solution $S_{\alpha e}$ and ideal configurational entropy of hydrogen atom in metal $S_{\alpha i}$,

$$S_\alpha = S_{\alpha e} + S_{\alpha i}, \tag{1-9}$$

$$S_{\alpha i} = -k\ln\left(\frac{r!}{x!(r-x)!}\right), \tag{1-10}$$

where r and x is the number of interstitial sites and hydrogen occupying these sites (per metal atom), respectively. By using Strling's approximation,

$$\ln(N!) = N\ln N - N. \tag{1-11}$$

$S_{\alpha i}$ is approximated by,

$$S_{\alpha i} = kr\ln\left(\frac{r}{r-x}\right) - kx\ln\left(\frac{x}{r-x}\right). \tag{1-12}$$

Therefore, the chemical potential of hydrogen atom in the solid solution is described as follows, assuming that the partial enthalpy and entropy of the non-configurational part of the partial entropy of hydrogen in the solid solution are given by h_α and $s_{\alpha e}$, respectively,

$$\mu_\alpha(T,p,x) = \frac{\partial G}{\partial x} = h_\alpha - Ts_{\alpha e} + kT\ln\left(\frac{x}{r-x}\right), \tag{1-13}$$

$$H_\alpha = xh_\alpha,\ S_{\alpha e} = xs_{\alpha e}, \tag{1-14}$$

In the case of low hydrogen concentrations with $x << r$, the following approximation is derived,

$$\ln\left(\frac{x}{r-x}\right) \rightarrow \ln x - \ln r, \tag{1-15}$$

we obtain,

$$\mu_\alpha(T,p,x) = h_\alpha - Ts_{\alpha e} + k\ln x - kT\ln r. \tag{1-16}$$

Taking into account that the chemical potential of hydrogen gas is equal to that of hydrogen in the solid solution, Eq. (1-4) becomes

$$kT\ln\left(\frac{p}{p_0(T)}\right)^{\frac{1}{2}} - \frac{1}{2}E_d = h_\alpha - Ts_{\alpha e} + kT\ln\left(\frac{x}{r-x}\right). \tag{1-17}$$

Finally, we obtain the following equation in the case of low hydrogen concentration in the solid solution,

$$x = K_s(T)\ln\left(\frac{p}{p_0(T)}\right)^{\frac{1}{2}}, \tag{1-18}$$

where

$$K_s(T) = \exp\left(\frac{Ts_{\alpha e} - h_\alpha - 1/2E_d + kT\ln r}{kT}\right). \quad (1\text{-}19)$$

This is known as Sievelt's law.

In the plateau region below critical temperature T_c, thermodynamics of hydride formation is described in the following way;

Here, the following hydrogen absorption reaction between a material A and hydrogen is considered.

$$aA + bH_2 \rightarrow aAH_{2b}. \quad (1\text{-}20)$$

The Gibbs's free energy ΔG of this reaction can be expressed by using enthalpy change ΔH, entropy change ΔS and temperature T in the following equations,

$$\Delta G = \Delta H - T\Delta S, \quad (1\text{-}21)$$

$$= aH_{AH} - aH_A - bH_{H_2} - T(aS_{AH} - aS_A - bS_{H_2}), \quad (1\text{-}22)$$

where H_{AH}, H_A and H_{H2} are the enthalpy of AH_{2b}, A and H_2, respectively. S_{AH}, S_A and S_{H2} are the entropy of AH_{2b}, A and H_2. The standard entropy of gas phase can be separated to standard entropy S^0_{H2}, which is the entropy of hydrogen molecule at 0.1 MPa, and the entropy change of hydrogen gas due to the reaction as given by the following equation,

$$S_{H_2} = S^0_{H_2} - R\ln\left(\frac{p_{eq}}{p_0(T)}\right), \quad (1\text{-}23)$$

where R is the gas constant and p_{eq} is the equilibrium pressure. Considering Eqs. (1-21), (1-22), and (1-23), following equation is defined,

$$\Delta S^o = aS_{AH} - aS_A - bS^0_{H_2}. \quad (1\text{-}24)$$

Generally, the standard enthalpy of simple substance should be zero. In the case of equilibrium condition, ΔG should be zero. Considering above equations, the following equation is finally obtained,

$$\ln\left(\frac{p_{eq}}{p_0(T)}\right)=\frac{\Delta H}{RT}-\frac{\Delta S^0}{R}. \quad (1\text{-}25)$$

This equation is called the van't Hoff equation. The ΔH and ΔS values can be experimentally estimated. The slope and the intercept in the plot of $\ln(p_{eq}/p_0(T))$ versus $1/T$ give ΔH and ΔS values, respectively, as shown in Fig. 1-1 (b). This plot is called the van't Hoff plot. Various enthalpy and entropy changes of the hydrogenation reaction of metals are shown in Table 1-2. For mobile storage, target thermodynamic property is p_{eq} = 1~10 bar at 0~100 °C corresponding to ΔH = 15~24 kJ/mol H_2 [1-5].

Table 1-2. Enthalpy change ΔH and entropy change ΔS for the formation of metal hydrides [1-13].

system	ΔH kJ/mol H_2	$\Delta S^0/R$ (mol H_2)$^{-1}$
Li-LiH	−158	−16.2
Na-NaH	−114	−19.6
K-KH	−118	−20.2
Rb-RbH	−108	−20.4
Cs-CsH	−114	−20.4
Mg-MgH_2	− 74	−16.0
Ca-CaH_2	−182	−16.8
Sr-SrH_2	−198	−18.8
Ba BaH_2	−174	−17.2
Sc-ScH_2	−200	−17.4
Y-YH_2	−226	−17.4
YH_2-YH_3	−178	−16.6
La-LaH_2	−208	−18.2
LaH_2-LaH_3	−168	—
Ce-CeH_2	−206	−17.8
CeH_2-CeH_3	−238	—
Pr-PrH_2	−208	−17.6
Nd-NdH_2	−212	−17.6
Sm-SmH_2	−222	−19.6
Gd-GdH_2	−196	−15.8
Er-ErH_2	−226	−18.8
Ti(hcp)-TiH_2	−130	−12
Zr(hcp) ZrH_2	−188	−18
Hf(hcp)-HfH_2	−130	−12
V-$VH_{0.5}$	− 72	−13
V-VH_2	− 40	−18
Nb-$NbH_{0.65}$	− 92	−16
Nb-NbH_2	− 40	−16
Ta-$TaH_{0.5}$	− 78	−12
Mn(α)-MnH	− 22	−14*
Ni-NiH	− 58	−14*
Pd-$PdH_{0.5}$	− 40	−10
Mg_2Ni-Mg_2NiH_4	− 64	−14.4
TiFe-TiFeH	− 28	−12.4
$CaNi_5$-$CaNi_5H_4$	34	−12.2
$LaNi_5$-$LaNi_5H_4$	− 32	−13

* Assumed value

1-2-2 Kinetics of hydrogen absorption and desorption

There are several steps for proceeding of the hydrogen absorption/desorption reactions in a metal. In the absorption reaction, the following steps would be occurred,

(1) Physisorption of molecular hydrogen on the metal surface.

(2) Dissociation of molecular hydrogen into atomic hydrogen and chemisorption on the metal surface.

(3) Migration of hydrogen atom through the surface layer.

(4) Diffusion of hydrogen through the bulk.

(5) Formation of the solid solution of hydrogen in the metal or hydride formation.

The slowest step dominates the reaction kinetics and is the rate-determining step for the hydrogen absorption/desorption processes. Hence, clarification of the reaction mechanism is quite important in order to improve the kinetics of the hydrogen storage materials. Although desorption can be regarded as the reverse process, the rate-determining step may not necessarily be the same as the reverse process. Thus, for improving the kinetic properties of the hydrogen storage materials, it is important to understand each step.

All hydrogen has to go through the surface of metal in the absorption and desorption process. In the case of the absorption process, a hydrogen molecule is firstly physisorbed on the surface of metal and then dissociated into atomic hydrogen (chemisorption). After that, the atomic hydrogen diffuses into the bulk. For the hydrogen desorption process, a pair of hydrogen atoms encounters each other in the surface of metal and recombines to form a hydrogen molecule. Finally, it leaves the surface as gaseous hydrogen. Therefore, the surface properties of the metal can be a critical role to understand the overall kinetics of the hydrogen absorption/desorption

processes.

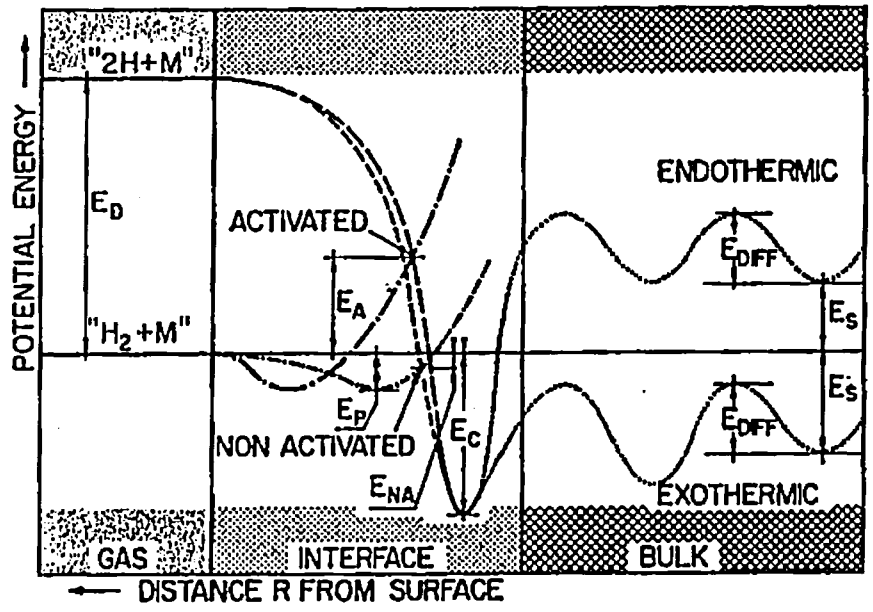

Figure 1-2. A one dimensional potential energy curve for hydrogen molecule and for hydrogen atoms on a clean metal surface [1-14].

Fig. 1-2 shows the potential energy of the hydrogen absorption process which is simplified to a one-dimensional set of potential energy curves for the hydrogen molecule or atoms with a clean metal surface. The dissociation energy of hydrogen molecule ($H_2 \rightarrow 2H$) outside the surface of metal is E_D = 431.4 kJ mol^{-1} H_2 [1-13]. In the first step of the absorption, the hydrogen molecule is physisorbed on the surface of metal with small heat (heat of physisorption, $E_p \approx$ 10 kJ mol^{-1} H_2) as shown in the "H_2 + M"-curve in Fig. 1-2. The deep minimum potential of chemisorption of atomic hydrogen (heat of chemisorption $E_c \approx$ 50 kJ mol^{-1} H_2) is described in the "*2H* + *M*"-curve in Fig. 1-2. For dissociation and formation of the chemisorbed state, hydrogen has to overcome an activation barrier which is defined at the intersection between "H_2 +

M"- and "$2H + M$"-curves in Fig. 1-2. If this intersection is above the zero energy level, positive activation energy E_A is required for chemisorption. In this case, the kinetics of dissociative absorption and recombination are slow and it may control overall kinetics of absorption and desorption, respectively, as the rate-determining step. On the other hand, if the potential energy of the intersection is below the zero energy, the hydrogen molecule is easy to dissociate and recombine by E_{NA} in the interface as shown in Fig. 1-2. The height of the activation barrier depends on the surface elements involved in the metal species and the crystal plane of the metal. Generally, the *d*-orbit which is in the conduction band of metals such as transition metals can easily hybridize with the *s*-orbit of the hydrogen atoms covalently, so energy of the conduction band is lowered. This property realizes the negative enthalpy change for the formation of the solid solution. The chemisorbed hydrogen atoms may have a high mobility on the metal surface, interact with each other and form surface phases at sufficiently high coverage.

The hydrogen atoms adsorbed on the metal migrate to the crystal site through the surface layer. If the amount of adsorbed hydrogen on the metal surface sites increases, the top layer atoms of metal rearrange. In this stage, hydrogen atoms can adsorb on the metal subsurface sites, which is located in the most inner atomic layer of the metal surface sites, in addition to the metal surface site. Finally, the hydrogen atom diffuses into the interstitial sites through the metal lattice. The kinetics of hydrogen absorption and desorption reactions in the bulk may be strongly influenced by the mobility of atomic hydrogen. In the bulk, the hydrogen atoms which are trapped at the interstitial sites can jump to the neighbor site by receiving a heat energy from the phonon in the metal, where the diffusion of hydrogen is permitted due to the tunneling effect. Therefore, temperature controls the local diffusion of hydrogen at the interstitial sites. In

the high-temperature region, diffusion can be described by classic barrier hopping. Thus, the temperature dependence of the diffusion rate can be expressed in the following equation,

$$D = D_0 \exp\left(-\frac{E_{diff}}{kT}\right), \tag{1-26}$$

where D_0 is a pre-exponential factor, k is the Boltzmann constant and E_{diff} is an activation energy of diffusion. This is identical to the empirical rate relationship that Arrhenius identified it for chemical reactions [1-15]. As shown in Fig. 1-3, the activation energy of diffusion E_{diff} and the pre-exponential factor D_0 can be estimated by using the Arrhenius plot. Figure 1-3 shows that the thermal diffusion process of hydrogen in the metal is described in the thermally activated process obeying Eq. (1-26). Table 1-3 lists the E_{diff} and D_0 values for the bcc metals. The hydrogen atoms diffusing in the metal dissolve into lattice and form the solid solution and/or metal hydride. In the case of forming a hydride, the reaction kinetics is mainly limited by the hydrogen diffusion process, nucleation and growth or movement of the interface between the hydride and the metal.

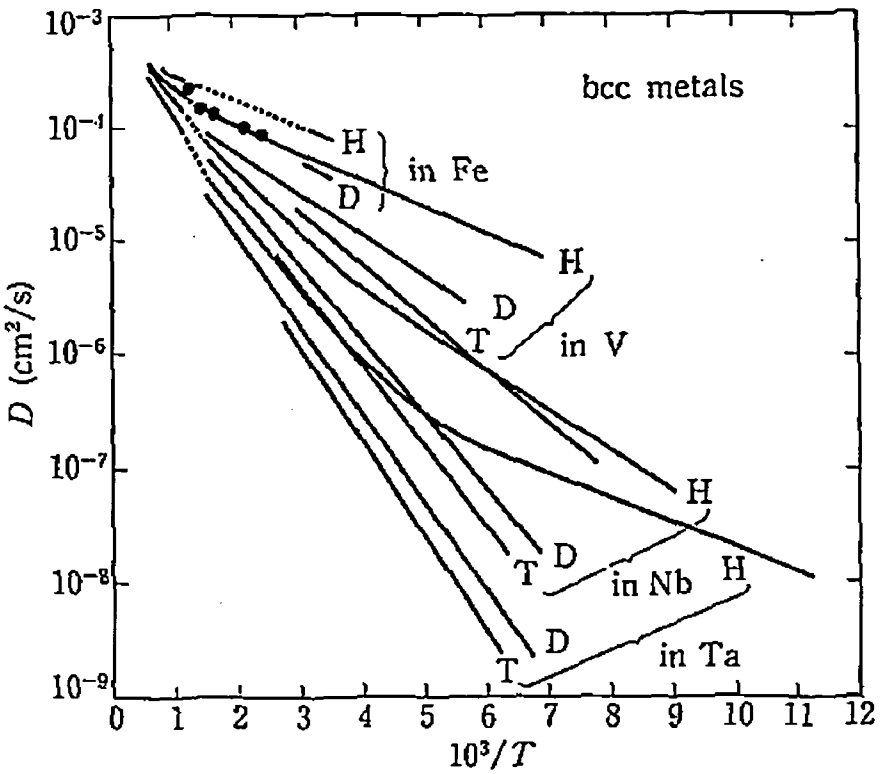

Figure 1-3. Arrhenius plots of bcc metals [1-12].

Table 1-3. Parameters of diffusion coefficient for bcc metals [1-12].

Metal	Isotope	T [K]	D_0 [10^{-4}cm^{2}s^{-1}]	E_a [eV]	Method	Reference
Fe	H	290–1040	4.2	0.040	P[a]	[6.93]
	D	273–317	4.2	0.063	P	[6.94]
V	H	143–667	3.1 ± 0.8	0.045 ± 0.004	G[b]	[6.95]
		810–1380	8.9	0.113	A[c]	[6.96]
	D	176–573	3.8 ± 0.8	0.073 ± 0.004	G	[6.95]
	T	133–353	4.9 ± 1.0	0.092 ± 0.004	G	[6.95]
Nb	H	108–250	0.9 ± 0.2	0.068 ± 0.004	G	[6.95]
		250–560	5.0 ± 1.0	0.106 ± 0.006	G	[6.95]
		873–1390	10	0.144	A	[6.96]
	D	148–560	5.2 ± 1.0	0.127 ± 0.006	G	[6.95]
	T	159–283	4.6 ± 1.0	0.135 ± 0.006	G	[6.95]
Ta	H	90–190	0.028 ± 0.012	0.042 ± 0.006	G	[6.95]
		250–573	4.2 ± 1.2	0.136 ± 0.010	G	[6.95]
		986–1386	10	0.167	A	[6.96]
	D	146–573	3.8 ± 1.2	0.152 ± 0.008	G	[6.95]
	T	166–358	3.8 ± 1.2	0.165 ± 0.008	G	[6.95]

[a]P: Permeation, [b]G: Gorsky effect, [c]A: Absorption.

The most common method to evaluate the kinetic properties of the reaction is simply to measure the concentration of hydrogen absorption or desorption as a function of time. The kinetics of the solid state reaction can be described by the following general relationship,

$$F(\theta) = K(T) \cdot t, \tag{1-27}$$

$$\theta = \frac{C}{C_0}, \tag{1-28}$$

where C is a concentration of reaction at t and C_0 is a final concentration $t=\infty$. The function $F(\theta)$ depends on the rate limiting mechanism of the reaction. $K(T)$ is the rate constant of the reaction which is described as,

$$K(T) = K^0 \exp\left(-\frac{E_a}{RT}\right), \tag{1-29}$$

where K^0 is a frequency factor, E_a is an activation energy of the reaction. This equation indicates that the kinetics of the reaction highly depends on temperature and E_a.

The simplest reaction is the first order one, in which the reaction rate is proportional to the reactant concentration in the following equation,

$$F_1(\theta) = -\ln(1-\theta). \tag{1-30}$$

The relationship can be applied to the absorption and desorption kinetics of the hydrogen metal system when the kinetics is controlled by only the concentration of the hydride. Therefore, the hydrogen absorption and desorption kinetics is imply expressed in terms of concentration and temperature as follows,

$$\text{Absorption: } \frac{d\theta}{dt} = K_{ab}(T) \cdot (1-\theta), \theta: 0 \rightarrow 1, \tag{1-31}$$

$$K_{ab}(T) = K_{ab}^0 \exp\left(-\frac{E_{ab}}{RT}\right), \tag{1-32}$$

$$\text{Desorption: } \frac{d\theta}{dt} = K_{de}(T)\cdot(-\theta), \theta: 1 \rightarrow 0, \tag{1-33}$$

$$K_{de}(T) = K_{de}^{0}\exp\left(-\frac{E_{de}}{RT}\right), \tag{1-34}$$

where K^0_{ab}, E_{ab}, and K^0_{de}, E_{de} are the frequency factors and the activation energies of the absorption and desorption processes, respectively. The activation energy E_a can be obtained from the Arrhenius plot (the slope of $\ln K(T)$ versus $1/T$) by measuring the rate constant $K(T)$ at several temperatures in the following equation,

$$\ln K(T) = \frac{E_a}{RT} + \ln K^0. \tag{1-35}$$

1-3 Hydrogen storage materials

1-3-1 General

In general, there are two kinds of the hydrogen storage materials. One is "physisorption material", in which hydrogen is physically absorbed at low temperature due to the high surface area. For example, the carbon based materials [1-16, 1-18], metal-organic framework-5 (MOF-5) [1-19~1-21] and Zeolites [1-22~1-24] are studied. In this case, a low temperature such as below -196 °C (boiling point of liquid nitrogen) and a high hydrogen pressure are required to absorb a large amount of hydrogen because of their small enthalpy change of physisorption (a few kJ mol^{-1} H_2) [1-16]. The carbon based materials include carbon nano-tubes (CNTs) [1-16, 1-17] and carbon-nano fibers [1-18]. Among them, Züttel *et al.* reported that single-wall CNTs physically absorbed ~3.0 mass% of hydrogen with the specific surface area of ~1300 m^2 g^{-1} at -196 °C [1-16]. MOF-5 is a composition of $Zn_4O(BDC)_3$ (BDC = 1, 4-benzenedicarboxylate) with a cubic three-dimensional extended porous structure, which absorbs hydrogen up to ~4.5 mass% (17.2 hydrogen molecules per formula unit)

at -196 °C and 1.0 mass% at room temperature under 2.0 MPa H_2 [1-20]. Zeolites are a large class of highly aluminosilicate materials, defined by a network of linked cavities and pores on the molecular scale dimensions that rise their molecular sieving properties [1-22]. Zeolites can be absorbed hydrogen over 1 mass% at cryogenic temperatures [1-23] and below 0.3 mass% at room temperature or above 200 °C [1-24].

Another group of hydrogen storage materials is the chemisorption type, in which hydrogen is chemically absorbed in the material with forming chemical bond. Hydrogen is a chemically active element and reacts with almost all the elements as shown in Table 1-4 because of having the moderate electronegativity of 2.2 as shown in Table 1-5, which is a medium value among all the elements. Hydrides are classified into four main groups: ionic hydrides, covalent hydrides, interstitial hydrides, and complex hydrides as follows.

Table.1-4 Hydrides in the periodic table [1-25].

1 A	2 A											3 B	4 B	5 B	6 B	7 B
LiH 3	BeH_2 4											B_2H_6 5	CH_4 6	NH_3 7	H_2O 8	HF 9
NaH 11	MgH_2 12	3 A	4 A	5 A	6 A	7 A	8 A			1 B	2 B	AlH_3 13	SiH_4 14	PH_3 15	H_2S 16	HCl 17
KH 19	CaH_2 20	ScH_2 21	TiH_2 22	VH VH_2 23	CrH 24	Mn 25	Fe 26	Co 27	NiH 28	CuH 29	ZnH_2 30	GaH_3 31	GeH_4 32	AsH_3 33	H_2Se 34	HBr 35
RbH 37	SrH_2 38	YH_2 YH_3 39	ZrH_2 40	NbH NbH_2 41	Mo 42	Tc 43	Ru 44	Rh 45	PdH 46	Ag 47	CdH_2 48	InH InH_3 49	SnH_4 50	SbH_3 51	TeH_2 52	HI 53
CsH 55	BaH_2 56	La~Lu 57~71	HfH_2 72	TaH 73	W 74	Re 75	Os 76	Ir 77	Pt 78	Au 79	HgH_2 80	TlH TlH_3 81	PbH_4 82	BiH_3 83	PoH_2 84	At 85
		Ac~Lu 89~92														
Lanthanoid 57~71		LaH_2 LaH_3 57	CeH_2 CeH_3 58	PrH_2 PrH_3 59	NdH_2 NdH_3 60	Pm 61	SmH_2 SmH_3 62	EuH_2 63	GdH_2 GdH_3 64	TbH_2 TbH_3 65	DyH_2 DyH_3 66	HoH_2 HoH_3 67	ErH_2 ErH_3 68	TmH_2 TmH_3 69	YbH_2 YbH_3 70	LuH_2 LuH_3 71
Actinoid 89~92		AcH_2 89	ThH_2 Th_4H_{15} 90	PaH_3 91	UH_3 92	NpH_2 NpH_3 93	PuH_2 PuH_3 94	AmH_2 AmH_3 95								

Table 1-5 Electronegativity of elements of the periodic table (Pauling) [1-26].

Z	Symbol	X	Z	Symbol	X	Z	Symbol	X
1	H	2.20	33	As	2.18	65	Tb	—
2	He	—	34	Se	2.55	66	Dy	1.22
3	Li	0.98	35	Br	2.96	67	Ho	1.23
4	Be	1.57	36	Kr	—	68	Er	1.24
5	B	2.04	37	Rb	0.82	69	Tm	1.25
6	C	2.55	38	Sr	0.95	70	Yb	—
7	N	3.04	39	Y	1.22	71	Lu	1.0
8	O	3.44	40	Zr	1.33	72	Hf	1.3
9	F	3.98	41	Nb	1.6	73	Ta	1.5
10	Ne	—	42	Mo	2.16	74	W	1.7
11	Na	0.93	43	Tc	2.10	75	Re	1.9
12	Mg	1.31	44	Ru	2.2	76	Os	2.2
13	Al	1.61	45	Rh	2.28	77	Ir	2.2
14	Si	1.90	46	Pd	2.20	78	Pt	2.2
15	P	2.19	47	Ag	1.93	79	Au	2.4
16	S	2.58	48	Cd	1.69	80	Hg	1.9
17	Cl	3.16	49	In	1.78	81	Tl	1.8
18	Ar	—	50	Sn	1.96	82	Pb	1.8
19	K	0.82	51	Sb	2.05	83	Bi	1.9
20	Ca	1.00	52	Te	2.1	84	Po	2.0
21	Sc	1.36	53	I	2.66	85	At	2.2
22	Ti	1.54	54	Xe	2.60	86	Rn	—
23	V	1.63	55	Cs	0.79	87	Fr	0.7
24	Cr	1.66	56	Ba	0.89	88	Ra	0.9
25	Mn	1.55	57	La	1.10	89	Ac	1.1
26	Fe	1.83	58	Ce	1.12	90	Th	1.3
27	Co	1.88	59	Pr	1.13	91	Pa	1.5
28	Ni	1.91	60	Nd	1.14	92	U	1.7
29	Cu	1.90	61	Pm	—	93	Np	1.3
30	Zn	1.65	62	Sm	1.17	94	Pu	1.3
31	Ga	1.81	63	Eu	—			
32	Ge	2.01	64	Gd	1.20			

(1) Ionic hydrides

Ionic hydrides are formed by bonding between hydrogen and alkali metals (Li, Na, and K) or alkali earth metals (Ca, Sr, and Ba). Since the electronegativity of the metals is smaller than that of hydrogen, the metal atom becomes a positive M^{n+} cation and hydrogen becomes negative H^- anion (protide). Those ions combine each other by the electrostatic Coulomb attraction force. The structure of alkali hydrides (LiH, NaH, KH, RbH, and CsH) is the NaCl-type structure. Generally, ionic hydrides are stable, so high temperature is required to release hydrogen in the hydrides. Among them, beryllium hydride BeH_2, calcium hydride CaH_2 and magnesium hydride (MgH_2) have both ionic

and covalent bonding.

(2) Covalent hydrides

Covalent hydrides are formed by bonding between hydrogen and 3B~7B elements which have larger electronegativity than that of hydrogen. In the covalent hydrides, an electron is shared among hydrogen and the host atoms, so no ion exists. Anomalistically, fluorine forms ionic bonding hydride HF with proton H^+ because of having higher electronegativity than hydrogen. Generally, the covalent hydrides form simple molecules such as AlH_3, H_2O, and NH_3 in the form of solid (occasionally they has low melting point), liquid (volatile liquid) or gas phase, respectively, at room temperature. In addition, some of them are easy to form a polymer molecule with hydrogen bridging bond (B and Al) or covalent bonding (Si, Ge and Zn), however they could be easily decomposed even at room temperature because all of them are quite unstable. Since Kariya *et al.* has reported the chemical reaction, $C_6H_6 + 3H_2 \leftrightarrow C_6H_{12}$[1-27~1-29], this kind of reactions also have been paid attention.

(3) Metallic hydrides (Interstitial hydrides)

Transition metals (3A~8A) form metallic hydrides. At high temperatures, 3A~5A transition metals and Pd form interstitial hydrides, in which hydrogen exists at the interstitial site of transition metal. Hydrogen is absorbed into the metal by the exothermic reaction and exists as neutral atom (protium H^0) at the interstitial sites of the metal. On the other hand, 6A~8A transition metals except for Pd absorb a small amount of hydrogen by endothermic reaction and hydrogen in the metal exists as H^+ (proton). The bonding between metal and hydrogen is so weak that hydrogen can diffuse easily in

the metal.

(4) Alloy (Intermetallic compound)

By combining hydride-forming metals *A* (3A~5A transition metals, Mg, and Ca) and non-hydride-forming metals *B* (6A~8A transition metals), the reversible hydrogen storage materials, which are the intermetallic compounds, can be designed. They can generally be written in the formulae of AB_5 (ex. $LaNi_5$), AB_2 (ex. $TiCr_{1.8}$), *AB* (ex. TiFe), and A_2B (ex. Mg_2Ni). Since hydrogen occupies some interstitial sites of the metal, the structure of the sublattice of metal doesn't change and the unit cell volume expands.

$LaNi_5$ with AB_5 type has 1.4 mass% hydrogen capacity and can desorb hydrogen at room temperature under hydrogen pressure of 0.2~0.3 MPa with excellent kinetics [1-25].

$TiCr_{1.8}$ with AB_2 type has the C15 type Laves phase structure at lower temperature and absorbs 2.4 mass% of hydrogen and desorbs hydrogen at −91 °C under hydrogen pressure of 0.1 MPa [1-25]. $TiMn_{1.5}$ and $ZrMn_2$ have also the Laves phase structure (C14 type). They are also absorbs relatively large amount of hydrogen but their equilibrium hydrogen pressure are too high and too low for practical uses, respectively [1-25].

TiFe with *AB* type has a hydrogen storage capacity of 1.8 mass% and desorbs hydrogen at room temperature under hydrogen pressure of 0.3 MPa. The advantage of TiFe is that it is cheaper than other alloys. However, the surface activation treatment, which is to take out metal oxide and/or metal hydroxide on the surface, is required at the initial hydrogenation. It takes long time to perform the surface activation treatment of TiFe, therefore Fe in TiFe has been partially substituted by Mn in order to improve

kinetics at initial hydrogenation [1-30].

Mg_2Ni with A_2B type has a hydrogen storage capacity of 3.6 mass% and desorbs the hydrogen at 250 °C under hydrogen pressure of 0.1 MPa [1-31]. However, this material also needs the surface activation treatment.

Those hydrogen storage alloys can desorb hydrogen at lower temperature than ionic hydrides and covalent hydrides under hydrogen pressure of 0.1 MPa, but the hydrogen storage capacity is essentially less than 3 mass%.

(5) Complex hydrides

Complex hydride is described as $M(XH_m)_n$, which has a bonding between M^{n+} (M = 1A and 2A elements, n = 1 and 2) and XH_m^{n-} (X = 3B~5B elements, m = 2, 3, and 4). Complex hydrides have relatively large hydrogen capacities and have been recently investigated as hydrogen storage materials. However, they usually are air- and moisture sensitive, so handling of the sample under inert atmosphere conditions is required. In the past few years, many composite systems composed of metal hydride MH_n and complex hydride $M(XH_m)_n$ were reported and developed their performances. Details of complex hydrides and the composites are described below.

M-Al-H systems

Bogdanović *et al.* have reported that $NaAlH_4$ or some related chemical substance doped with Ti could reversibly store 3.6 mass% of hydrogen under 180 °C [1-32~1-34]. The hydrogen desorption/absorption reactions of $NaAlH_4$ are described as follows,

$$NaAlH_4 \leftrightarrow 1/3Na_3AlH_6 + 2/3Al + H_2 \leftrightarrow NaH + Al + 2H_2. \quad (1\text{-}36)$$

After that, this system was deeply investigated by plenty of researchers and is regarded

as one of the promising hydrogen storage materials [1-35~1-40]. Recently, the hydrogen storage properties of $Mg(AlH_4)_2$ (9.27 mass%) and $Ca(AlH_4)_2$ (7.84 mass%) have been also reported [1-41, 1-42].

_M_-N-H systems

The *M*-N-H system is based on metal amide $M(NH_2)_n$ such as $LiNH_2$, $NaNH_2$, $Mg(NH_2)_2$, and $Ca(NH_2)_2$. $M(NH_2)_n$ desorbs only ammonia NH_3 but the composites of metal hydride MH_n and $M(NH_2)_n$ desorb and absorb hydrogen. In 2002, lithium nitride absorbing/desorbing a large amount of hydrogen has been reported by Chen *et al.* [1-43] as another candidate of the reversible hydrogen storage materials. The reaction is expressed as follows,

$$Li_3N + 2H_2 \leftrightarrow Li_2NH + LiH + H_2 \leftrightarrow LiNH_2 + 2LiH. \quad (1\text{-}37)$$

The system is so-called as Li-N-H system. According to through the two-step reations in Eq. (1-37), the theoretical hydrogen capacity of this system is reached 10.4 mass%. However, the operation temperature of the first step is very high (430 °C) because of large enthalpy change (~148 kJ/mol H_2) and a very long reaction time is required for complete recovery of Li_3N from the hydrogenated state [1-44]. On the other hand, the second reaction step has small enthalpy change (~44.5 kJ/mol H_2). In addition, the hydrogen capacity of the second reaction is still large (6.5 mass%). Thus, this reaction is considered to be worth one of the rechargeable hydrogen storage system, which is expressed as follows:

$$LiNH_2 + LiH \leftrightarrow Li_2NH + H_2. \quad (1\text{-}38).$$

Ichikawa *et al.* reported that the composite of $LiNH_2$ and LiH doped with 1 mol% $TiCl_3$ prepared by ball a milling method reversibly desorbed and absorbed a large amount of

hydrogen (~5.5 mass%) at around 150~200 °C [1-45]. Furthermore, they also proposed that the hydrogen desorption reaction (1-38) could proceed through the following two-step elementary reaction mediated by ammonia [1-46, 1-47],

$$2LiNH_2 \rightarrow Li_2NH + NH_3 \quad (1\text{-}39)$$

and

$$LiH + NH_3 \rightarrow LiNH_2 + H_2 \quad (1\text{-}40)$$

By analogy with Li-N-H system, some new *M*-N-H systems such as $Mg(NH_2)_2$-LiH systems [1-48~1-51], $Mg(NH_2)_2$-MgH_2 system [1-51, 1-52], and Li-Ca-N-H systems [1-49] have been developed for hydrogen storage.

NH_xBH_x

NH_xBH_x complex is also attractive materials for hydrogen storage material because NH_xBH_x desorbs a large amount of hydrogen by using thermolysis and hydrolysis [1-53, 1-54]. For hydrolysis, NH_3BH_3 desorbs hydrogen by reacting with water and forming boric acid H_3BO_3 [1-55]. For the thermolysis, there are several reactions for each NH_xBH_x as follows [1-56~1-59],

$$NH_4BH_4 \rightarrow NH_3BH_3 + H_2\text{: 6.13 mass\% below -40 °C} \quad (1\text{-}41)$$

$$nNH_3BH_3 \rightarrow -(NH_2BH_2)_n- + nH_2\text{: 6.53 mass\% below 114 °C} \quad (1\text{-}42)$$

$$-(NH_2BH_2)_n- \rightarrow -(NHBH)_n- + nH_2\text{: 6.99 mass\% below 200 °C} \quad (1\text{-}43)$$

$$-(NHBH)_n- \rightarrow nBN + nH_2\text{: 7.5 mass\% over 400 °C} \quad (1\text{-}44)$$

However, these reactions are exothermic and aminoborane NH_2BH_2, borazine $(NHBH)_3$ or diborane B_2H_6 are desorbed in the all dehydrogenation processes, indicating that rehydrogenation of them is difficult. Recently, NH_3BH_3-scaffold nanocomposite, which is NH_3BH_3 impregnated in the pores of scaffold [1-60], and of the NH_3BH_3-based

materials, which are synthesized by reacting between NH_3BH_3 and other hydrogen storage material such as LiH, NaH, and $LiNH_2$ [1-61, 1-62], have been reported.

(6) Hydrides based on layer-structured materials

The layer-structured materials such as graphite C and hexagonal boron nitride hBN are paid attention as the hydrogen storage material. First, the carbon materials have been expected as on of the candidate for the hydrogen storage material because of cheep price, abundant resource and simple handling. Carbon can absorb hydrogen chemically as well as physically. Hydrogenated graphite is synthesized by mechanical ball-milling under hydrogen or hydrocarbon atmosphere [1-63~1-65], which is denoted as $C^{nano}H_x$. This material absorbs ~7 mass% of hydrogen after milling for 80 h. Although, high temperature (more than 700 °C) is required to proceed dehydrogenation reaction of this material [1-63] and hydrocarbons (CH_4 and/or C_2H_6) are also desorbed from $C^{nano}H_x$ during the dehydrogenation reaction. It is experimentally confirmed that the hydrogen atoms are stored in $C^{nano}H_x$ as functional groups (–CH, $-CH_2$, and $-CH_3$) [1-66~1-69]. Recently, $C^{nano}H_x$ has been developed by combining with metal hydride (LiH, NaH, MgH_2, and CaH_2) [1-70, 1-71]. The reaction mechanism of the LiH-$C^{nano}H_x$ composite was clarified that metal carbide Li_2C_2 forms in the dehydrogenated state after the dehydrogenation reaction and hydrocarbons are desorbed in the rehydrogenation reaction [1-72]. hBN absorbs ~2 mass% of hydrogen after milling for 80 h under hydrogen atmosphere and desorbs in the wide temperature range from 100 to more than 900 °C [1-73~1-75]. In addition, the composite of LiH and hBN milled under ammonia atmosphere desorbs ~5.0 mass% of hydrogen at around 200 °C without ammonia emission [1-75].

1-3-2M-B-H system

The metal borohydrides $M(BH_4)_n$ are the quite attractive material for hydrogen storage because boron atom stores four hydrogen atoms by forming $(BH_4)^-$ ion. The most famous borohydride is $LiBH_4$, which has high gravimetric and volumetric hydrogen densities; ~18 mass% and 121 kg H_2/m^3, respectively [1-76]. The synthesis of pure $LiBH_4$ was firstly performed in 1940 by Schlesinger and Brown [1-77] and the thermal analysis of $LiBH_4$ was performed in 1964 by Fedneva *et al.* [1-78]. However, this material had not been paid attention as a hydrogen storage material until the 21st century. The crystal structure of $LiBH_4$ is orthorhombic (space group: *Pnma*) at low temperature and hexagonal (space group: $P6_3mc$) above 115 °C [1-79]. The hexagonal phase at high temperature is the Li superionic conductor [1-80] and the melting point of $LiBH_4$ is 280 °C [1-79] The first investigation of $LiBH_4$ as a hydrogen storage material was reported by Züttel *et al.* [1-81, 1-82], in which the thermal decomposition properties were examined. They reported that $LiBH_4$ desorbed hydrogen up to ~13.5 mass% according to the following reaction:

$$LiBH_4 \rightarrow LiH + B + 1.5H_2. \quad (1\text{-}45)$$

However, the dehydrogenating temperature of $LiBH_4$ was too high for practical use and the reversibility was not realized because of its quite slow kinetics. In order to improve the dehydrogenation kinetics, they also reported that the thermal decomposition of SiO_2-doped $LiBH_4$ has three dehydrogenation steps on $LiBH_4$ with increasing temperature. After that, many studies of additives such as $TiCl_3$, V_2O_5, Al, and so on have been reported [1-83~1-85]. Recently, the intermediate phase of $LiBH_4$ has been theoretically and experimentally predicted to be $LiB_{12}H_{12}$ [1-86, 1-87].

For other borohydride, $NaBH_4$ has very high dehydrogenation temperature but has

been studied for hydrolysis [1-88]. $Mg(BH_4)_2$ is recently paid attention because of having relatively low dehydrogenation temperature (~350 °C) [1-89]. The intermediate state of $Mg(BH_4)_2$ has been also reported to be $MgB_{12}H_{12}$ [1-87]. $Ca(BH_4)_2$ desorbs ~9.6 mass% of hydrogen at 360~450 °C with two dehydrogenation steps [1-90] The systematic research of dehydrogenation temperature on many borohydrides such as $Zn(BH_4)_2$, $Sc(BH_4)_3$, and $Zr(BH_4)_4$ were reported by Nakamori, *et al.* [1-91]. The rehydrogenation of them is quite difficult and there are only few reports of the rehydrogenation reaction for the $M(BH_4)_n$ [1-92~1-96]. For example, Orimo *et al.* reported that the rehydrogenation reaction between LiH and B is proceeded to form $LiBH_4$ under 35 MPa H_2-gas pressures at 600 °C [1-92].

In 2004, a new hydrogen storage system composed of $LiBH_4$ and MgH_2 was exhibited a better reversibility than $LiBH_4$ itself [1-97]. The reaction is expressed by the following equation,

$$2LiBH_4 + MgH_2 \leftrightarrow 2LiH + MgB_2 + 4H_2. \quad (1\text{-}46)$$

It is noteworthy that a finite hydrogen pressure is necessary for the reaction of MgH_2 with $LiBH_4$ to yield MgB_2. In contrast, the Mg and B phases instead of the MgB_2 phase are produced after the dehydrogenation reaction under vacuum. This reaction is expressed by the following equation,

$$2LiBH_4 + MgH_2 \rightarrow 2LiH + Mg + 2B + 4H_2. \quad (1\text{-}47)$$

After that, many MH_n-$M(BH_4)_n$ systems have been reported [1-98~1-101]. Interestingly, almost all the reversible *M*-B-H systems form metal boride such as magnesium diboride MgB_2 or calcium hexaboride CaB_6 [1-99, 1-100].

References

[1-1] "Kyoto Protocol: Status of Ratification", United Nations Framework Convention on Climate Change, http://unfccc.int/files/kyoto_protocol/status_of_ratification/application/pdf/kp_ratification.pdf

[1-2] The Nobel Foundation, http://nobelprize.org/nobel_prizes/peace/laureates/2007/press.html

[1-3] Eejits' Guides, http://www.eejitsguides.com/environment/carbon-neutral.html

[1-4] Ministy for the Environment of Japan, http://www.env.go.jp/en/wpaper/2007/fulltext.pdf

[1-5] L. Schlapbach and A. Züttel, *Nature* **414** (2001) 353-358.

[1-6] A. Züttel, *Mitigation and Adaptation Strategies for Global Change* **12** (2007) 343-365.

[1-7] Y. Kojima, Y. Kawai, S. Towata, T. Matsunaga, T. Shinozawa, and M. Kimbara, *J. Alloys Compd.* **419** (2006) 256-261.

[1-8] New Energy and Industrial Technology Development Organization, http://www.nedo.go.jp/

[1-9] U. S. Department of Energy, http://energy.gov/

[1-10] International Energy Agency, http://www.iea.org/

[1-11] L. Schlapbach, *Hydrogen in Intermetallic Compounds I*, ed. L. Schlapbach, Springer-Verlag, **63** (1988).

[1-12] Y. Fukai, *The Metal-hydrogen System 2nd edition*, Materials Science, ed. U. Gonser, Springer-Verlag, **21** (2004).

[1-13] Y. Fukai, K. Tanaka, and H. Uchida, *Hydrogen and Metal*, Uchidarokakuho.

Japan, (1998) (in Japanese).

[1-14] L. Schlapbach, *Hydrogen in Intermetallic compounds II*, ed. L. Schlapbach, Springer-Verlag, **67** (1992).

[1-15] S. Arrenius, *Z. Phys. Chem.* **4** (1889) 226-248.

[1-16] A Züttel, C. Nutzenadel, P. Sudan, P. Mauron, C. Emmenegger, S. Rentsch, L. Schlapbach, A. Eidenkaff and T. Kiyobayashi, *J. Alloys Compd.* **330** (2002) 676-682.

[1-17] H. Kajiura, S. Tsutsui, K. Kadono, K. Kakuta, M. Ata, and Y. Murakami, *Appl. Phys. Lett.* **82** (2003) 1105-1107.

[1-18] C. Park, P.E. Anderson, A. Chambers, C.D. Tan, R. Hidalgo, and N.M. Rodriguez, *J. Phys. Chem. B* **103** (1999) 10572-10581.

[1-19] H. Li, M. Eddaoudi, M. O'Keeffe, and O.M. Yaghi, *Nature* **402** (1999) 276-279.

[1-20] N.L. Rosi, J. Eckert, M. Eddaoui, D.T. Vodak, J. Kim, M.O_Keeffe, and O.M. Yaghi, *Science* **300** (2003) 1127-1129.

[1-21] J.L.C Rowsell, A.R. Millward, K.S. Park, and O.M. Yaghi, *J. Am. Chem. Soc.* **126** (2004) 5666-5667.

[1-22] A. Dyer, *An Introduction to Zeolite Molecular Sieves*, John Wiley & Sons (1988).

[1-23] V.B. Kazansky, V.Y. Borovkov, A. Serich, and H.G. Karge, *Micropor, Mesopor, Matter.* **22** (1998) 251-259.

[1-24] H.W. Langmi, A. Walton, M.M. Al-Mamouri, S.R. Johnson, D. Book, J.D. Speight, P.P. Edwards, I. Gameson, P.A. Anderson, and I.R. Harris, *J. Alloys Compd.* **356-357** (2003) 710-715.

[1-25] Y. Osumi, *Hydrogen Storage Alloy*, AGUNE Gijutsu Center (1999) (*in Japanese*).

[1-26] *CRC Handbook of Chemistry and Physics 89*, ed. D.R. Lide, CRC Press (2008).

[1-27]N. Kariya, A. Fukuoka, and M. Ichikawa, *Applied Catalysis A: General* **233** (2002) 91-102.

[1-28]N. Kariya, A. Fukuoka, and M. Ichikawa, *Chem. Commun.* (2003) 690-691.

[1-29]N. Kariya, A. Fukuoka, T. Utagawa, M. Sakuramoto, Y. Goto, and M. Ichikawa, *Applied Catalysis A: General* **247** (2003) 247-259.

[1-30]M.H. Mintz and S.Vaknin, *J. Appl. Phys.* **52** (1981) 463-467.

[1-31]J.J. Reilly and R.H. Wiswall, *Inorg. Chem.* **7** (1968) 2254-2256.

[1-32]B. Bogdanović and M. Schwictrardi, *J. Alloys Compd.* **253-254** (1997) 1-9.

[1-33]B. Borislavć, R.A. Brand, A. Marjanovi, M. Schwickardi, and J. Tölle, *J. Alloys Compd.* **302** (2000) 36-58.

[1-34]B. Bogdanovic and M. Schwickardi, *Appl.Phys. A* **72** (2001) 221-223.

[1-35]C.M. Jensen and K.J. Gross, *Appl. Phys. A* **72** (2001) 213-219.

[1-36]C.M. Jensen, R. Zidan, N. Mariels, A. Hee, and C. Hagen, *International Journal of Hydrogen Energy* **24** (1999) 461-465.

[1-37]R.A. Zidan, S. Takara, A.G. Hee, and C.M. Jensen, *J. Alloys Compd.* **285** (1999) 119-122.

[1-38]G. Sandrock, K. Gross, G. Thomas, *J. Alloys Compd.* **339** (2002) 299-308.

[1-39]K.J. Gross, G.J. Thomas, and C.M. Jensen, *J. Alloys. Compd.* **330-332** (2002) 683-690.

[1-40]A. Zaluska, L. Zaluski, and J. O. Ström-Olsen, *J. Alloys Compd.* **298** (2000) 125-134.

[1-41]Y. Kim, E.K. Lee, J.H. Shim, Y.W. Cho, and K.B. Yoon, *J. Alloys Compd.* **422** (2006) 283-287.

[1-42]K. Komiya, N. Morisaku, Y. Shinzato, K. Ikeda, S. Orimo, Y. Ohki, K. Tatsumi,

H. Yukawa, and M. Morinaga, *J. Alloys Compd.* **446-447** (2007) 237-241.

[1-43] P. Chen, Z.T. Xiong, J.Z. Luo, J.Y. Lin, and K.L. Tan, *Nature* **420** (2002) 302-304.

[1-44] Y.H. Hu and E. Ruckenstein, *Ind. Eng. Chem. Res.* **42** (2003) 5135-5139.

[1-45] T. Ichikawa, S. Isobe, N. Hanada, and H. Fujii, *J. Alloys Compd.* **365** (2004) 271-276.

[1-46] T. Ichikawa, N. Hanada, S. Isobe, H.Y. Leng, and H. Fujii, *J. Phys. Chem. B* **108** (2004) 7887-7982.

[1-47] S. Isobe, T. Ichikawa, S. Hino, and H. Fujii, *J. Phys. Chem. B* **109** (2005) 14855-14858.

[1-48] H.Y. Leng, T. Ichikawa, S. Hino, N. Hanada, S. Isobe, and H. Fujii, *J. Phys. Chem. B* **108** (2004) 8763-8765.

[1-49] Z. Xiong, G. Wu, J. Hu, and P. Chen, *Adv. Mater.* **16** (2004) 1522-1525.

[1-50] Y. Nakamori, G. Kitahara, K. Miwa, S. Towata, and S. Orimo, *Appl. Phys. A* **80** (2005) 1-3.

[1-51] Y. Nakamori, G. Kitahara, and S. Orimo, *J. Power Sour.* **138** (2004) 309-312.

[1-52] H.Y. Leng, T. Ichikawa, S. Isobe, S. Hino, H. Hanada, and H. Fujii, *J. Alloys Compd.* **404-406** (2005) 443-447.

[1-53] G.E. Ryschkewitsch, *J. Am. Chem. Soc.* **82** (1960) 3290-3294.

[1-54] F. Baitalow, J. Baumann, G. Wolf, K. Jaenicke- Jaenicke-Rößler, and G. Leitner, *Thermochim. Acta* **391** (2002) 159-168.

[1-55] H.C. Kelly and V.B. Marriot, *Inorg. Chem.* **18** (1979) 2875-2878.

[1-56] D.P. Kim, K.T. Moon, J.G. Kho, J. Economy, C. Gervais, and F. Babonneau, *Plym. Adv. Technol.* **10** (1999) 702-712.

[1-57] G. Wolf, J. Baumann, F. Baitalow, and F.P. Hoffmann, *Thermochim. Acta* **343** (2000) 19-25.

[1-58] C.A. Jaska, K. Temple, A.J. Lough, and I. Manners, *J. Am. Chem. Soc.* **125** (2003) 9424-9434.

[1-59] H.W. Langmi and G.S. McGrady, *Coord. Chem. Rev.* **251** (2007) 925-935.

[1-60] A. Gutowska, L. Li, Y. Shin, C.M. Wang, X.S. Li, J.C. Linehan, R.S. Smith, B.D. Kay, B. Schmid, W. Shaw, M. Gutowska, and T. Autrey, *Angew. Chem. Int. Ed.* **44** (2005) 3578-3582.

[1-61] Z. Xiong, C.K. Yong, G. Wu, P. Chen, W. Shaw, A. Karkamar, T. Autrey, M.O. Jones, S.R. Johnson, P.P. Edwards, and W.I.F. David, *Nat. Mater.* **7** (2008) 138–141.

[1-62] P. Chen and M. Zhu, *Materials Today,* **11** (2008) 36-43.

[1-63] S. Orimo, G. Majer, T. Fukunaga, A. Züttel, L. Schlapbach, and H. Fujii, *J. Appl. Phys. Lett.* **75** (1999) 3093-3095.

[1-64] T. Kiyobayasi, K. Komiyama, N. Takeichi, H. Tanaka, H. Senoh, H.T. Takeshita, and N. Kuriyama, *Mat. Sci. Eng. B-Solid State Mat. adv. Technol.* **108** (2004) 134-137.

[1-65] T. Ichikawa, D.M. Chen, S. Isobe, E. Gomibuchi, and H. Fujii, *Mat. Sci. Eng B-Solid State Mat. Adv. Technol.* **108** (2004) 138-142.

[1-66] T. Fukunaga, K. Itoh, S. Orimo, and K. Aoki, *Mat. Sci. Eng. B-Solid State Mat. adv. Technol.* **108** (2004) 105-113.

[1-67] N. Ogita, K. Yamamoto, C. Hayashi, T. Matsushima, S. Orimo, T. Ichikawa, H. Fujii, and M. Udagawa, *J. Phys. Soc. Jpn.* **73** (2004) 553-555.

[1-68] G. Majer, E. Stanik, and S. Orimo, *J. Alloys Compd.* **356** (2003) 617-621.

[1-69] K. Tatsumi, S. Muto, and T. Yoshida, *J. Appl. Phys.* **101** (2007) 023523-1-7.

[1-70] H. Miyaoka, T. Ichikawa, and H. Fujii, *J. Alloys Compd.* **432** (2007) 303-307.

[1-71] T. Ichikawa, S. Isobe, and H. Fujii. *Mater. Trans.* **46** (2005) 1757-1759.

[1-72] Hiroki Miyaoka, Doctral thesis, Hiroshima University (2007).

[1-73] P. Wang, S. Orimo, T. Matsushima, H. Fujii, and G. Majer, *Appl. Phys. Lett.* **80** (2002) 318-320.

[1-74] Y. Kojima, Y. Kawai, and N. Ohba, *J. Power Sour.* **159** (2006) 81-87.

[1-75] C. Wu, H. Miyaoka, T. Ichikawa, and Y. Kojima, *Int. J. Hydrogen Energy* **33** (2008) 3128-3131.

[1-76] L. Schlapbach, A. Züttel, *Nature* **414** (2001) 353-358.

[1-77] H.J. Schlesinger and H.C. Brown, *J. Am. Chem. Soc.* **62** (1940) 3429-3435.

[1-78] E.M. Fedneva, V.L. Alpatova, and V.I. Mikheeva, *Russ. J. Inorg. Chem.* **9** (1964) 826-827.

[1-79] A. Züttel, A. Borgschulte, and S. Orimo, *Scr. Mater.* **56** (2007) 823-828.

[1-80] M. Matsuo, Y. Nakamori, and S. Orimo, *Appl. Phys. Lett.* **91** (2007) 224103 (1)-224103 (3).

[1-81] A. Züttel, P. Wenger, S. Rentsch, P. Sudan, Ph. Mauron, and Ch. Emmenegger, *J. Power Sour.* **118** (2003) 1-7.

[1-82] A. Züttel, S. Rentsch, P. Fischer, P. Wenger, P. Sudan, Ph. Mauron, and Ch. Emmenegger, *J. Alloys Compd.* **356-357** (2003) 515-520.

[1-83] M. Au and Arthur Jurgensen *J. Phys. Chem. B* **110** (2006) 7062-7067.

[1-84] Z.X. Guo, C. Shang, and K.F. Aguey-Zinsou, *J. Eur. Ceram. Soc.* **28** (2008) 1467-1473.

[1-85] X.D. Kang, P. Wang, L.P. Ma, and H.M. Cheng, *Appl. Phys. A* **89** (2007)

963-966.

[1-86] N. Ohba, K. Miwa, M. Aoki, T. Noritake, and S. Towata, *Phys. Rev. B* **74** (2006) (1)-075110 (7).

[1-87] S.W. Hwang, R.C. Bowman Jr., J.W. Reiter, J. Rijssenbeek, G.L. Soloveichik, J.C. Zhao, H. Kabbour, and C.C. Ahn, *J. Phys. Chem. C* **112** (2008) 3164-3169.

[1-88] S. Suda, N. Morinaga, Y. Iwase, and Z.P. Li, *J. Alloys Compd.* **404-406** (2005) 643-647..

[1-89] T. Matsunaga, F. Buchter, K. Miwa, S. Towata, S. Orimo, and A. Züttel, *Renew. Energy* **33** (2008) 193-196.

[1-90] J.H. Kim, S.A. Jin, J.H. Shin, and Y.W. Cho, *J. Alloys Compd.* **461** (2008) L20-L22.

[1-91] Y. Nakamori, H.W. Li, M. Matsuo, K. Miwa, S. Towata, and S. Orimo, *J. Phys. Chem. Solids* **69** (2008) 2292-2296.

[1-92] S. Orimo, Y. Nakamori, G. Kitahara, K. Miwa, N. Ohba, S. Towata, and A. Züttel, *J. Alloys. Compd.* **404-406** (2005) 427-430.

[1-93] E. Rönnebro and E. H. Majzoub, *J. Phys. Chem. B* **111** (2007) 12045-12047.

[1-94] T. Matsunaga, F. Buchter, P. Mauron, M. Bieman, Y. Nakamori, S. Orimo, N. Ohba, M. Miwa, S. Towata, and A. Züttel, *J. Alloys Compd.* **459** (2008) 583-588.

[1-95] J.H. Kim, S.A. Jin, J.H. Shim, and Y.W. Cho, *Scr. Mater.* **58** (2008) 481–483.

[1-96] H.-W. Li, K. Kikuchi, Y. Nakamori, N. Ohba, K. Miwa, S. Towata, and S. Orimo, *Acta Mater.* **56** (2008) 1342-1347.

[1-97] J. J. Vajo, S. L. Skeith, and F. Mertens, *J. Phys. Chem. B* **109** (2005) 3719-3722.

[1-98] J. Yang, A. Sudik, and C. Wolverton, *J. Phys. Chem. C* **110** (2007) 19134-19140.

[1-99] G. Barkhordarian, T. Klassen, M. Dronheim, and R. Bormann, *J. Alloys. Compd.*

440 (2007) L18-L21.

[1-100] F.E. Pinkerton and M.S. Meyer, *J. Alloys Compd.* **464** (2008) L1-L4.

[1-101] J. Purewal, S.J. Hwang, R.C. Bowman Jr., E. Rönnebro, B. Fultz, and C. Ahn, *J. Phys. Chem. C* **112** (2008) 8481-8485.

2 Purpose of this thesis

In order to realize a hydrogen energy system, the development of hydrogen storage and transportation systems is the key issue as described in Chapter 1. Especially, the improvements of hydrogen storage material having high hydrogen capacity and low operating temperature are significantly important for on-board application.

Metal borohydrides $M(BH_4)_n$ have attracted much attention because many $M(BH_4)_n$, such as $LiBH_4$ (13.8 mass% [2-1]), $Mg(BH_4)_2$ (15.0 mass% [2-2]), and $Ca(BH_4)_2$ (9.6 mass% [2-3]) have relatively higher hydrogen capacity than other light element materials such as MgH_2 (7.6 mass% [2-4]). However, because of their slow dehydrogenation kinetics, these borohydrides have relatively higher dehydrogenation temperatures than the other systems having a similar ΔH. For example, the dehydrogenation temperature of $LiBH_4$ (ΔH: 64 kJ/mol H_2) which is above 400°C [2-5] is higher than that of MgH_2 (ΔH: 76.15 kJ/mol H_2) which is 370 °C [2-6]. In addition, the rehydrogenation kinetics of the borohydrides are also slow. Therefore, a complete rehydrogenation of $M(BH_4)_n$ is quite difficult [2-7~2-11] although their enthalpy changes for the rehydrogenatoin reactions are exothermic and sufficiently large to make a progress under the moderate pressure. In order to implove the hydrogen storage properties of $M(BH_4)_n$, Vajo *et al.* proposed in an idea of combining lithium borohydride $LiBH_4$ with magnesium hydride MgH_2, *i.e.*, the Li-Mg-B-H system as described in Chapter 1 [2-12]. Although the dehydrogenation temperature of this system is still high (>400°C), it was demonstrated that rehydrogention kinetics was significantly improved by forming MgB_2 during the dehydrogention. In addition, almost all the reversible *M*-B-H systems generate metal boride $M'B_m$ such as MgB_2 or CaB_6 after the

dehydrogenation [2-13, 2-14]. However, the mechanism describing how $M'B_m$ is formed during the dehydrogenation reaction and why the rehydrogenation reaction is easily proceeded when $M'B_m$ exists have not been clarified yet.

On the other hand, with respect to the hydrogenation of the *M*-B-H systems, those kinetics are too slow to obtain the fully hydrogenated states under a moderate condition, such as below 30 MPa and 300 °C. However, in the case of small enthalpy change reaction for the hydrogenation of the reversible *M*-B-H systems, low temperature is required to make a progress of the hydrogenation reaction under the moderate pressure because of its extremely high equiliblium pressure at higher temperature than 300 °C. In order to improve the hydrogenation kinetics of the *M*-B-H systems, the hydrogenation by the milling technique would be effective as reported by Kojima *et al.* for some nitrides [2-15]. The hydrogenation by milling was applied for the *M*-B-H systems in this work.

Considering the above background, the fundamental research is required for development the *M*-B-H systems.

In this thesis, the *M*-B-H systems were focused on and their hydrogen storage properties were investigated. The purpose of this thesis is to obtain the guiding principle of material design for the *M*-B-H systems by investigating the hydrogen storage properties of the $M'H_m$-$M(BH_4)_n$ mixtures and the MH_n-$M'B_m$ mixtures which were hydrogenated by using a milling technique under hydrogen pressure. The following topics are discussed in this thesis.

(1) The condition of forming $M'B_m$ when the $M'H_m$-$M(BH_4)_n$ mixtures are dehydrogenated

(2) The milling effect on hydrogenation of the MH_n-$M'B_m$ mixtures

The content of (1) is taken up in Section 1 of Chapter 4. The dehydrogenation reactions on the MgH_2-$LiBH_4$, the CaH_2-$LiBH_4$, and the MgH_m-$Zn(BH_4)_2$ mixture (m = 0, 2) were investigated by thermogravimetry and differential thermal analysis combined with mass spectroscopy (TG-DTA-MS), high-pressure differential scanning calorimetry (p-DSC), X-ray powder diffraction (XRD), and Raman scattering in order to understand the condition of forming $M'B_m$.

The content of (2) is taken up in Section 2 of Chapter 4. Hydrogenation properties on several kinds of the MH_n-$M'B_m$ mixtures (M = Li and Sc, M' = Mg and Ca) which were milled under hydrogen pressure at room temperature were investigated by TG-MS, Fourier transform infrared spectroscopy (FT-IR), XRD, synchrotron radiation XRD (SR-XRD), and X-ray absorption spectroscopy (XAS).

References

[2-1] A. Züttel, P. Wenger, S. Rentsch, P. Sudan, Ph. Mauron, and Ch. Emmenegger, *J. Power Sour.* **118** (2003) 1-7.

[2-2] T. Matsunaga, F. Buchter, K. Miwa, S. Towata, S. Orimo, and A. Züttel, *Renew. Energy* **33** (2008) 193-196.

[2-3] J. H. Kim, S. A. Jin, J. H. Shin, and Y. W. Cho, *Scr. Mater.* **58** (2008) 481-483.

[2-4] B. Vigeholm, J. Kjoller, B. Larsen, J. Less-Common Met. **74** (1980) 341-350.

[2-5] A. Züttel, P. Wenger, S. Rentsch, P. Sudan, Ph. Mauron, and Ch. Emmenegger, *J. Power Sour.* **118** (2003) 1-7.

[2-6] N. hanada, T. Ichikawa, and H. Fujii, *J. Phys. Chem. B* **109** (2005) 7188-7194.

[2-7] S. Orimo, Y. Nakamori, G. Kitahara, K. Miwa, N. Ohba, S. Towata, and A. Züttel, *J. Alloys Compd.* **404-406** (2005) 427-430.

[2-8] E. Rönnebro and E. H. Majzoub, *J. Phys. Chem. B* **111** (2007) 12045-12047.

[2-9] T. Matsunaga, F. Buchter, P. Mauron, M. Bieman, Y. Nakamori, S. Orimo, N. Ohba, M. Miwa, S. Towata, and A. Züttel, *J. Alloys Compd.* **459** (2008) 583-588.

[2-10] J.H. Kim, S.A. Jin, J.H. Shim, and Y.W. Cho, *Scr. Mater.* **58** (2008) 481-483.

[2-11] H.-W. Li, K. Kikuchi, Y. Nakamori, N. Ohba, K. Miwa, S. Towata, and S. Orimo, *Acta Mater.* **56** (2008) 1342-1347.

[2-12] J. J. Vajo, S. L. Skeith, and F. Mertens, *J. Phys. Chem. B* **109** (2005) 3719-3722.

[2-13] G. Barkhordarian, T. Klassen, M. Dronheim, and R. Bormann, *J. Alloys Compd.* **440** (2007) L18-L21.

[2-14] F.E. Pinkerton and M.S. Meyer, *J. Alloys Compd.* **464** (2008) L1-L4.

[2-15] Y. Kojima, Y. Kawai, and N. Ohba, *J. Power Sour.* **159** (2006) 81-87.

3. Experimental procedures

3-1 Sample preparation

3-1-1 Materials

Starting materials used in this work are shown in Table 3-1. All the samples were handled in a glove-box filled with purified argon gas (purity > 99.9999 %) to minimize oxidation and water adsorption by the gas recycling purification system (Miwa Mfg. Co. Ltd., MP-P60W).

Table 3-1. General information of starting materials.

Material	purity, shape	Company
Lithium hydride (LiH)	95 %, powder	Sigma-Aldrich Co. Ltd.
Magnesium hydride (MgH_2)	95 %, powder	Gelest Inc.
Calcium hydride (CaH_2)	99.99 %, powder	Sigma-Aldrich Co. Ltd.
Lithium borohydride ($LiBH_4$)	95 %, powder	Sigma-Aldrich Co. Ltd.
Sodium borohydride ($NaBH_4$)	98 % powder	Sigma-Aldrich Co. Ltd
Magnesium diboride (MgB_2)	99 % , powder	Rare Metallic Co. Ltd.
Calcium hexaboride (CaB_6)	95+ %, powder	Alpha Aesar Co. Ltd.
Scandium (Sc)	99.9 %, powder	Sigma-Aldrich Co. Ltd.
Niobium oxide (Nb_2O_5) purity	99.5 %, powder, mesoporous, 3.2 nm	Sigma-Aldrich Co. Ltd.
Zinc chloride ($ZnCl_2$)	99.995+ % powder	Sigma-Aldrich Co. Ltd.
Scandium chloride ($ScCl_3$)	99.99 %, powder	Sigma-Aldrich Co. Ltd.

3-1-2 Mechanical ball milling method

Mechanical ball-milling method is used for various purposes such as mechanochemical reaction, preparation of mixture with close contact between

components, dispersion of catalyst, formation of small particle, and induction of defects

In this thesis, two types of ball-milling apparatuses are used. One is a rotating (planetary) ball-milling apparatus (Fritsch, P7) as shown in Fig. 3-1 (a), and another is vibrating (rocking) ball-miling apparatus (SEIWA GIKEN Co. Ltd., RM-10) as shown in Fig. 3-1 (b). A milling vessel with the inner volume of about 30 cm^3 made of Cr-steel (UMETOKU Co. Ltd., SKD-11) is specially designed, where a quick connector (Swagelok Co. Ltd.) is equipped to introduce hydrogen gas (purity: 7 N). Furthermore, either steel (SUJ-2) balls with 7 mm in diameter or zirconium oxide (ZrO_2) balls with 8 mm in diameter are chosen for the ball-milling depending on the specific purpose.

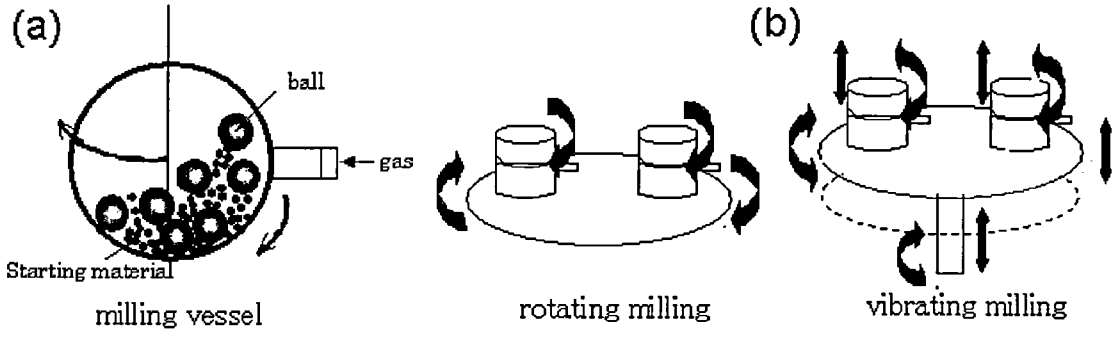

Figure 3-1. (a) Rotating (planetary) and (b) Vibrating (rocking) ball-milling apparatuses.

In this work, the samples of 300 mg and 20 balls are put into the vessel and the gas inside the milling vessel is evacuated by rotary pump (RP) and flushed with Ar. Furthermore, evacuation inside vessel was performed by turbo molecular pump (TMP). After that, the vessel is pressurized up to 1 or 6 MPa H_2 by using a Sievelt's-type equipment as shown in Fig. 3-2. Finally, the ball-milling is performed by repeatation of 1 h milling and 30 min interval, where a rotation number of the rotating milling and a

frequency of vibrating milling are fixed at 400 rpm and 10 Hz, respectively.

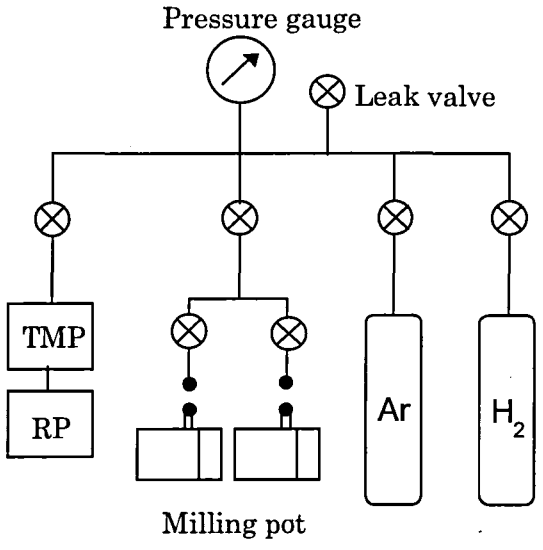

Figure 3-2. Sievelt's-type equipment.

3-1-3 Synthesis of samples

The $M'H_m$-$LiBH_4$ (M' = Mg, Ca) mixture

The $M'H_m$-$LiBH_4$ (M' = Mg, Ca) mixtures were prepared by the rotating milling method. The molar ratio of MgH_2 and $LiBH_4$ is 1 : 2 and that of CaH_2 and $LiBH_4$ is 1 : 6, respectively. These mixtures were obtained by milling at room temperature for 2 h under 1 MPa H_2.

Two-layered and hand-milled MgH_m-$Zn(BH_4)_2$ samples

First of all, the components of MgH_m-$Zn(BH_4)_2$ (m = 0 and 2) mixtures were prepared. As one component of the mixtures, Nb_2O_5-doped MgH_2 and its dehydrogenated sample (Nb_2O_5-doped Mg) were synthesized by the same procedure as reported by Hanada *et al.* [3-1]. Nb_2O_5-doped MgH_2 was prepared by rotating milling of MgH_2 and 1 mol% of

Nb_2O_5 at room temperature for 20 h under 1 MPa H_2 atmosphere. Nb_2O_5-doped Mg was obtained by the dehydrogenation reaction of Nb_2O_5-doped MgH_2 at 200 °C under vacuum condition for 8 h. As the another component of the mixtures, $Zn(BH_4)_2$ was synthesized by rotating milling of $ZnCl_2$ and $NaBH_4$ with a molar ratio of 1 : 2 at room temperature under 1 MPa H_2 pressure for 2 h [3-2]. Therefore, the as-synthesized $Zn(BH_4)_2$ contains NaCl. After that, two kinds of samples were prepared. One is denoted as two-layered MgH_m-$Zn(BH_4)_2$ sample, in which an enough amount of Nb_2O_5-doped MgH_m was placed directly on $Zn(BH_4)_2$ (a molar ratio of MgH_m and $Zn(BH_4)_2$ was around 15 : 1). Another is denoted as hand-milled MgH_m-$Zn(BH_4)_2$ samples, which were prepared by hand milling of Nb_2O_5-doped MgH_m and $Zn(BH_4)_2$ in an agate mortar for ~5 min.

The MH_n-$M'B_m$ (M = Li, and Sc, M' = Mg and Ca) mixture

The MH_n-$M'B_m$ (M = Li, and Sc, M' = Mg and Ca) mixtures were prepared by the vibrating milling method. The samples are put into a vessel and pressurized up to 6 MPa H_2. After that, they were milled at room temperature. The molar ration of samples and milling time were shown in Table 3-2. For the ScH_2-$M'B_m$ mixtures, ScH_2 was preliminary synthesized by the hydrogenation of Sc at 250 °C under 9.0 MPa H_2 for few minutes [3-3]. Furthermore, the dehydrogenation treatments for the as-milled MH_n-$M'B_m$ mixtures were performed at 500 °C under vacuum condition for 12 h.

Table 3-2. Milling conditions of the MH_n-$M'B_m$ mixtures.

Sample	Molar ratio of MH_n : $M'B_m$	Milling time (h)
LiH-MgB_2	2 : 1	80
LiH-CaB_6	6 : 1	160
ScH_2-MgB_2	2 : 3	80
ScH_2-CaB_6	2 : 1	160

Reference sample

The several kinds of reference were prepared in this work. MgH_2, $LiBH_4$, and CaH_2 were milled at room temperature under 1 MPa H_2 pressure for 2 h by using the rotating milling apparatus. Furthermore, MgB_2 and CaB_6 were milled at room temperature under 6 MPa H_2 respectively for 80 h and 160 h by using the vibrating milling apparatus. $Sc(BH_4)_3$ was synthesized by rotating milling $ScCl_3$ and $LiBH_4$ with a molar ratio of 1 : 3 at room temperature under 1 MPa H_2 pressure for 4 h [3-4] therefore the obtained $Sc(BH_4)_3$ contains LiCl. ScB_2 was synthesized by heating the mixture of scandium oxide Sc_2O_3 and boron B under the vacuum condition (at ~1300 °C for 40 min) in a high-frequency furnace.

3-2 Experimental technique

3-2-1 Thermogravimetry - Differential thermal analysis (TG-DTA) and thermal desorption mass spectroscopy (MS) analysis

Principle

Thermal analyses of samples are performed by thermogravimetry (TG) and

differential thermal analysis (DTA). The TG-DTA apparatus is equipped with a balance and thermo sensors. For TG-DTA measurement, the weight loss and thermogram during heating the samples are determined by measuring the difference of the weight and the temperature between a sample and a reference sample, respectively. In the case of hydrogen storage materials, if desorption gas from the sample is only hydrogen, the amount of hydrogen can be directly obtained from the weight loss by TG analysis. The dehydrogenation reaction can be determined whether it is endothermic or exothermic by DTA. The other thermal reactions such as phase transition and melting reaction can be also observed by DTA. The desorbed gases are led to an apparatus of thermal desorption mass spectroscopy (MS) through a capillary by flowing He gas as carrier, where the MS apparatus is connected with the TG-DTA. Thus, partial pressure of gases desorbed from the sample is removed.

MS can identify the gas desorbed from samples. The apparatus consists of three parts, an ionization source, a quadruple mass spectrometer, and a detector as shown in Fig. 3-3. The inside of the equipment is highly vacuumed by TMP.

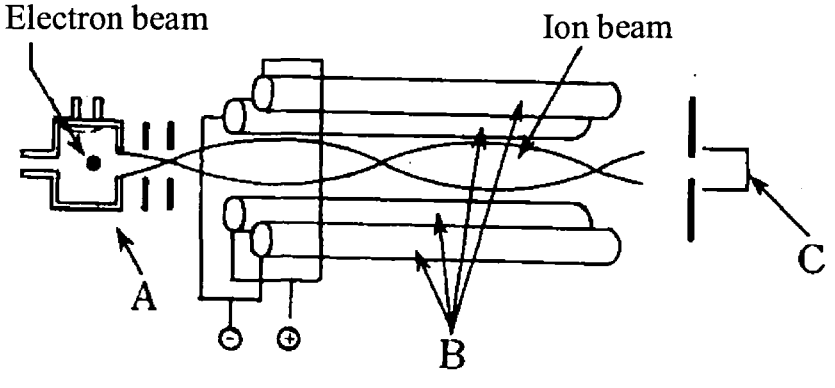

Figure 3-3. MS apparatus A: ionization source, B: quadruple mass spectrometer, and C: detector [3-5].

The gaseous molecules desorbed from the sample conflicts with electron beam and are ionized at the ionization part. And then, the molecular ions are separated by difference of the mass in the quadruple mass spectrometer. If the generated molecular ions have excess internal energy, they split to fragment ions. As shown in Fig. 3-4, a quadruple electrode consists of two twin electrodes, which are energized by modulating voltage. The voltages of the electrodes repeat the cycle as follows,

$$V_m = U + V\cos\omega t, \tag{3-1}$$

where U is D.C. voltage, ω is angular frequency, and $V\cos\omega t$ is the high frequency voltage (frequency is f [MHz] = $\omega/2\pi$). When the molecular ions enter into the quadruple mass spectrometer, the ions having specific mass/charge number m/z can pass through the electrode. The m/z is expressed by the following equation,

$$\frac{m}{z} = \frac{1}{7.22} \cdot \frac{V}{r_0^2 \cdot f^2} \tag{3-2},$$

where r_0 is the incircle radius among the quadruple electrode. Therefore, in order to separate the molecular ions by each mass number, V is continuously changed with keeping U/V value. The separated molecular ions are detected by electron multiplier tube. Finally, mass spectra of the gases from the sample are obtained.

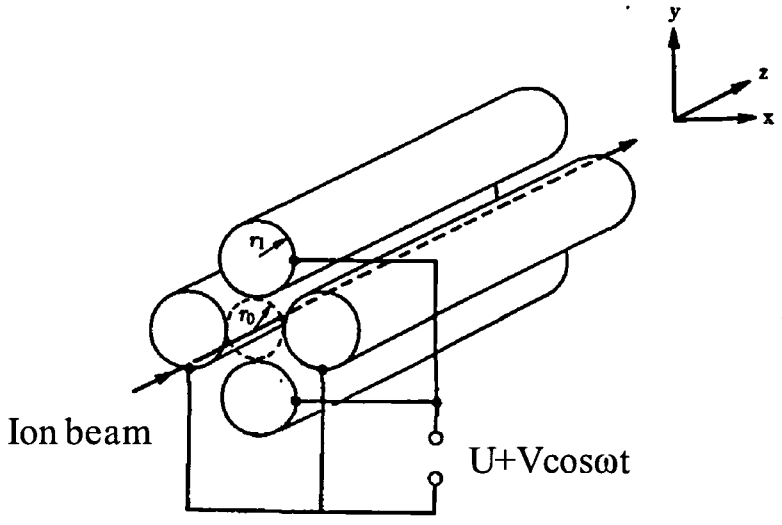

Figure 3-4. Quadruple mass spectrometer.

Procedure

The gas desorption properties of the samples were investigated by TG-DTA (Rigaku, TG8120) and MS (Anelva, M-QA200TS) equipment in the temperature range from room temperature to 150~500 °C with a heating rate of 5 °C/min under high purity He gas (purity > 99.9999 %) flow as a carrier gas with quite low partial pressure of desorbed gases. The sample pan used in this work was made by Aluminum. This equipment was located in a glove-box filled with purified Ar gas, so that the measurements of MS and TG-DTA can be simultaneously achieved without exposing the samples to air.

3-2-2 Differential scanning calorimetry (DSC)

Principle

Differential scanning calorimetry (DSC) can investigate the heat flow caused by a transition of material or chemical reaction such as gas desorption, phase transition,

melting, oxidation, and other heat related phenomena as a function of temperature and time as well as DTA. Moreover, DSC can provide quantitative and qualitative data of heat flow. There are two types of DSC systems, which are the power compensation type and the heat flux type. In this work, heat flux type DSC equipment was used. For the heat flux DSC, the sample and a reference are connected through a heat-flow path with low heat resistance (metal disc). The assembly is enclosed in a single furnace as shown in Fig. 3-5.

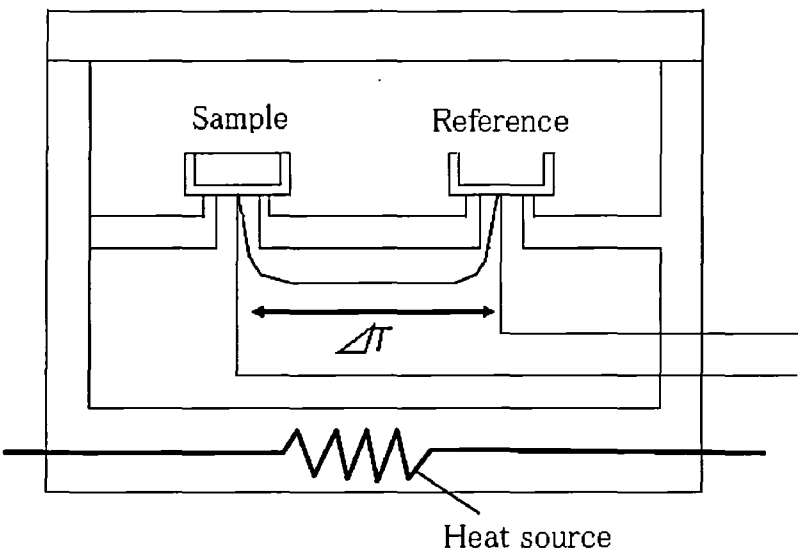

Figure 3-5. Heat flux type DSC.

In the DSC measurement, difference of temperature between the sample and a reference, which is caused by enthalpy change and heat capacity change in the sample, is recorded. From the obtained DSC profile, the thermal stability or the physical transitions of the sample can be discussed, and the enthalpy changes can be estimated by using experimental calibration. High pressure DSC (p-DSC) is able to realizes the thermal

analysis under gas pressure.

Procedure

The DSC equipment (TA Instruments, Q10 PDSC) is installed in a glove-box (Miwa MFG Co. Ltd., DBO-1.5 kPa) to avoid oxidation of the sample during the process of the measurement. The sample was put into an Al pan and set in the furnace. The DSC measurements were carried out in the heating process up to 450 °C with a heating rate of 5 °C/min under ~0.3 MPa Ar gas (purity > 99.9999 %) flow or 0.5 MPa H_2 in the closed system.

3-2-3 Powder X-ray diffraction (XRD) and synchrotron radiation XRD (SR-XRD)

Principle

Powder X-ray diffraction (XRD) is used to identify phases of materials and to determine lattice parameter and crystal structure. As shown in Fig. 3-6, incident X-ray is diffracted by each lattice plane, where each set of lattice planes is represented by Miller indices (*hkl*), and the distance between planes is denoted as d_{hkl}. The difference of the optical path between the plane P_1 and P_2 is expressed by $2d_{hkl}\sin\theta$ as shown in Fig. 3-6. Diffraction occurs when two diffracted X-rays satisfy the following equation,

$$n\lambda = 2d_{hkl}\sin\theta, \tag{3-3}$$

where n is positive integer, λ is wavelength, and θ is incident angle of X-ray. This diffraction condition is known as Bragg's law. By changing the 2θ angle between incident X-ray and diffracted one, XRD profiles can be obtained.

Synchrotron radiation XRD (SR-XRD) gives high resolution diffraction data because the synchrotron radiation X-ray has higher directivity than the laboratory source and

monochrome beam [3-6]. Therefore, the peaks corresponding to low-crystalline phase and small peaks in the profile of the crystal can be observed by SR-XRD.

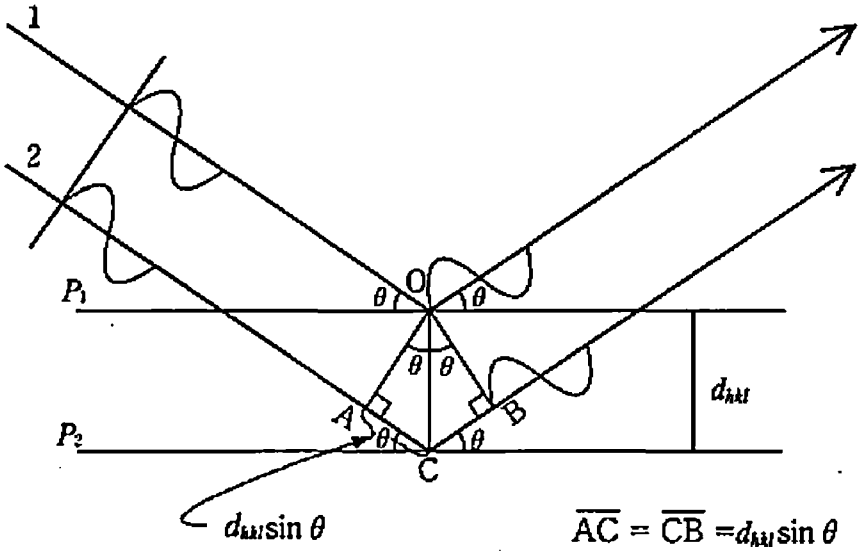

Figure 3-6. Diffraction of X-ray by lattice planes in crystal [3-6].

Procedure

In this work, powder XRD technique was used to identify the phases in the sample. The conventional X-ray diffractometer (Rigaku, RINT 2500V) using Cu-$K\alpha$ (λ = 1.54 Å) radiation at a power of 8 kW (40 kV, 200 mA) was used. The sample was spread on a glass plane with high vacuum grease (M&I Material Ltd., Apiezon®) as glue. In order to avoid the oxidization of samples, the sample was covered with a polyimide sheet (Du Pont-Toray Co. Ltd., Kapton®) of 8 μm thicknesses in a glove-box. All the XRD profiles measured in our laboratory have a broad peak at low angle (10~30 °) comes from grease and the polyimide sheet. The SR-XRD measurements were performed by using a large Debye-Schereer camera with an imaging plate as detectors at BL02B2 in SPring-8 [3-7]. The samples were stuffed into a glass capillary (thickness: 0.01 mm, diameter: 0.7 mm, Hilgenberg GmbH) then sealed by an epoxy adhesive in order to

avoid the oxidization of the sample. The wavelengthes of the X-ray used was 0.498962(11) Å calibrated by the lattice constant of ceria CeO_2 at room temperature. The obtained profiles were analyzed by comparing with powder diffraction file (PDF) [3-8]. For the analysis, the software "Jade 5.0" (Materials Data Inc.) was used.

3-2-4 Fourier transform infrared (FT-IR) and Raman scattering

Infrared (IR) and Raman scattering techniques are used to characterize the chemical bonding state in the solids, liquids, and gases. Both of them measure the vibrational energies of molecules and lattice but these methods originate in different selection rules. When a vibrational mode is IR active, the total dipole moment in the molecule must be changed. For example, the asymmetric stretching mode and bending mode in carbon dioxide CO_2 are IR active due to a change in the total dipole moment (Fig. 3-7(a)). The symmetric stretching mode in CO_2 is IR inactive because the total dipole moment is not changed (Fig. 3-7 (b)).

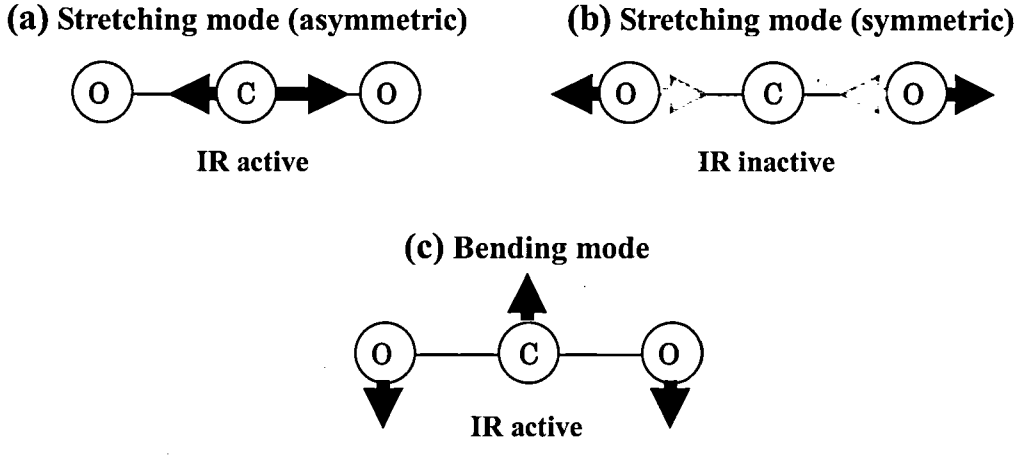

Figure 3-7. Vibrational modes of carbon dioxide.

On the other hand, the polarizability of the molecule must be changed when a vibrational mode is Raman active. As shown in Fig. 3-8, the symmetric stretching mode in carbon dioxide is Raman active because of the change of the polarizability in the molecule.

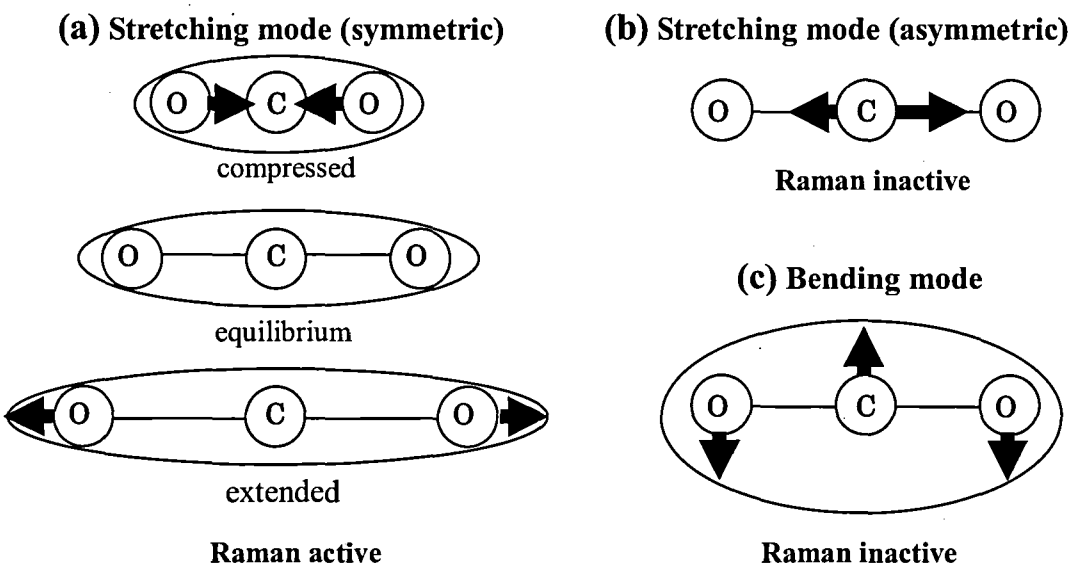

Figure 3-8. Changes of polarizability due to vibrational modes in CO_2.

Therefore, IR and Raman scattering are complemental to each other.

Procedure

The Fourier transform IR spectroscopy (FT-IR) measurements was performed at room temperature by using a diffuse reflection cell to investigate the IR active stretching modes of the groups such as B-H bonds in the samples. The FT-IR equipment (Pwekin-Elmer, Spectrum One) is installed inside a home made glove-box filled with

purified Ar gas. The samples which had a dark color were diluted by potassium bromide (KBr) down to 1 mass%. The background of IR spectra is assessed by using a mirror. With respect to the Raman scattering, the light source is an Ar ion gas laser (Spectra-physics Inc., Stabilite 2017) operated at a wavelength of 488.0 nm and Raman spectra were analyzed by a triple monochromator (JASCO, TRS-600) using a cooled charge coupled device (CCD) detector which is cooled by liquid-N_2 (Princeton Instruments Inc., model LN/CCD-1100-PB).

3-2-5 X-ray absorption spectroscopy (XAS)

Principle

X-ray absorption spectroscopy (XAS) is carried out in order to characterize electronic structure and local atomic environment of the target element in a material. When incident X-ray with energy E (= $h\nu$) transmits though the materials with thickness t, the relation between the intensity of incident X-ray I_0, and that of transmission X-ray I are described by the following equation,

$$I / I_0 = \exp(-\mu t) \qquad (3\text{-}4),$$

where μ is the linear absorption coefficient. μ has a tendency to decrease with the increase in X-ray energy, but the intensity jumps at specific energy E_0, which corresponds to the binding energy E_b of electron in each atom (Fig. 3-9). This phenomenon originates in emission of the photoelectron due to the excitation of the inner shell electron from lower energy to higher energies than E_b as shown in Fig. 3-9 (b). This energy is generally called as absorption edge. The absorption edge corresponds to electron shells in the atom as shown in Fig. 3-9 (a). In Fig. 3-9 (b), the fine structure near absorption edge energy is called as X-ray absorption near-edge structure (XANES)

and that over extended energy region is called as extended X-ray absorption fine structure (EXAFS).

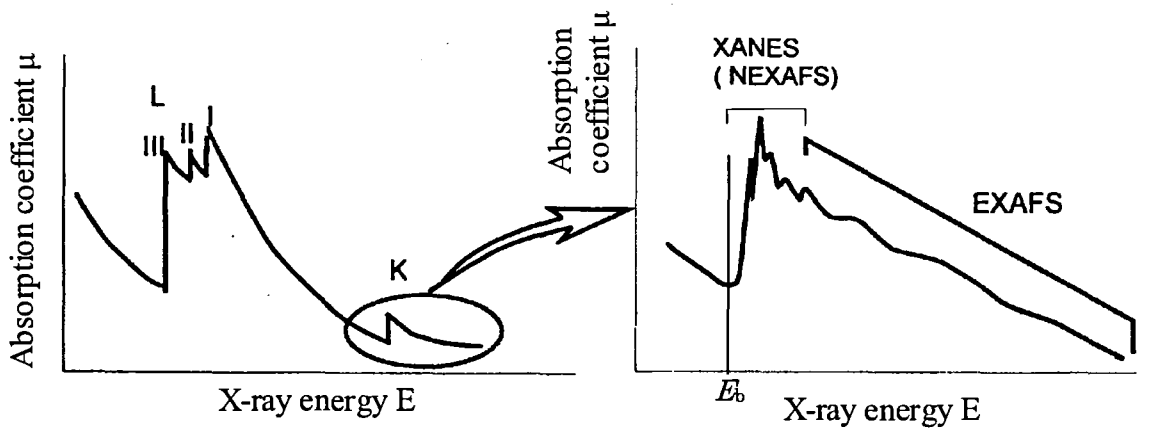

(a) (b)

Figure 3-9 (a) X-ray absorption spectrum and (b) magnified X-ray absorption spectrum near *K*-edge [3-8]

Both of XANES and EXAFS are called as X-ray absorption fine structure (XAFS). In the XANES profile, the chemical state of the target element can be recognized by the chemical shift of the absorption edge. From the EXAFS profile, the bond distance and the coordination number related to the excitation atoms can be obtained from the radial distribution function, which can be calculated by Fourier transformational analysis. In order to analyze the XAFS spectrum, some parameters such as phase shift, Debye-Waller factor, and back-scattering factor should be determined by using a standard sample or a simulation program such as FEFF [3-9]. Generally, XAFS measurements are performed in air, so the X-ray with lower energy than 5 keV (wavelength: 2Å) is significantly attenuated in the air. On the other hand, X-ray with

higher energy than 25 keV (wavelength: 0.5Å) has too large penetrating power, so that the range of X-ray energy for XAFS is limited to about 5~25 keV (wavelength: 0.5~2Å). Therefore, *K*-edge for forth and fifth period transition metals and L_{III}-edge for the heavier element than lanthanoid element is suitable for the XAFS measurement [3-10].

Procedure

The XAS measurements for Sc *K*- and Ca *K*-edges of the milled ScH_2-*M*'B_n mixture were performed at BL14B2 in SPring-8, Japan. This beam-line is a hard X-ray bending magnet beam-line and samples were measured in a transmission mode. The synchrotron radiation X-ray was monochromated by using Si (111) double-crystal monochromator in fixed-exit mode. The samples were formed into pellet with 1 cm in diameter by 600 kg press, and boron nitride BN powder (99 % purity, Kojundo chemical Lab. Co. Ltd.) was used as a diluent. To avoid the oxidation of the sample during the sample transfer and the measurement, the samples were covered with the transparent polyimide film with 8 μm thickness. The obtained data were analyzed by using the software "REX 2000 (Rigaku Co. Ltd.)". The background of obtained EXAFS spectrum was extracted by Spline Smoothing method [3-9].

References

[3-1] N. Hanada, T. Ichikawa, S. Hino, and H. Fujii, *J. Alloys Compd.* **420** (2006) 46-49.

[3-2] E. Jeon and Y.W. Cho, *J. Alloys Compd.* **422** (2006) 273-275.

[3-3] F.D. Manchester and J.M. Pitre, *J. Phase Equilib.* **18** (1997) 194-205.

[3-4] Y. Nakamori, H. Li, K. Miwa, S. Towata, and S. Orimo, *Mater. Trans.* **47** (2006) 1898-1901.

[3-5] S. Tanaka and Y, Iida, *Instrumental analysis*, Shokabo, Japan, (2000) 229 (in Japanese).

[3-6] I. Nakai, *X-ray Powder Analysis --- Introduction to the Rietveld Method*, ed. I. Nakai and F. Izumi, Asakura Publishing, (2002) (in Japanese).

[3-7] E. Nishibori, M. Takata, K. Kato, M. Sakata, Y. Kubota, S. Aoyagi, Y. Kuroiwa, M. Yamataka, and N. Ikeda, *J. Phys. Chem. Solids* **62** (2001) 2095-2098.

[3-8] T. Oota, *X-ray absorption spectroscopy method*, IPC, Japan, (2002) 2 (in Japanese).

[3-9] A.L. Ankudinov, B. Ravel, J.J. Rehr, and S.D. Conradson, *Phys. Rev. B* **58** (1998) 7565-7576.

[3-10] Y. Udagawa, *X-ray absorption fine spectroscopy*, Japan Scientific Societies Press (JSSP), Japan, (1999) Section 4.1.1 (in Japanese).

4 Results and discussion

4-1 Dehydrogenating properties of the M-B-H systems

4-1-1 Background and purpose

In 2004, Vajo *et al.* developed a new hydrogen storage system composed of $LiBH_4$ and MgH_2, which exhibited a much better reversibility than $LiBH_4$ itself [4-1]. The reaction is expressed by the following reaction equation,

$$MgH_2 + 2LiBH_4 \leftrightarrow 2LiH + MgB_2 + 4H_2. \quad (4\text{-}1)$$

It is noteworthy that a finite hydrogen pressure is necessary for the reaction of MgH_2 with $LiBH_4$ to yield MgB_2. In contrast, the Mg and B phases instead of the MgB_2 phase are produced after the dehydrogenation reaction under vacuum condition. This reaction is expressed by the following reaction equation,

$$MgH_2 + 2LiBH_4 \rightarrow 2LiH + Mg + 2B + 4H_2. \quad (4\text{-}2)$$

Almost all reversible $M'H_m$-$M(BH_4)_n$ systems form metal boride $M'B_m$ such as MgB_2 or CaB_6 by dehydrogenating under hydrogen pressure [4-2, 4-3]. At present, it is not yet clarified how $M'B_m$ forms during the dehydrogenation process. Therefore, in this section, the condition of forming metal boride in the dehydrogenated state of the *M*-B-H systems was investigated. Thermal analysis for the $M'H_m$-$LiBH_4$ (M' = Mg and Ca) mixtures were performed and hydrogen storage property of the MgH_m-$Zn(BH_4)_2$ mixtures were investigated in order to understand how $M'B_m$ is formed during the dehydrogenation process.

4-1-2 Results

4-1-2-1 The MgH_2-$LiBH_4$ mixture

The results of the thermal analyses for MgH_2 are shown in Fig. 4-1, where the above thermal analyses were performed by (a) TG-DTA under He flow, (b) p-DSC under ~0.3 MPa Ar flow, and (c) ~0.5 MPa H_2 in the closed system. Under He flow condition, it can be seen as an endothermic peak corresponding to the decomposition reaction of MgH_2 at ~330 °C (Fig.4-1 (a)), which is almost the same as that under Ar flow condition (Fig. 4-1 (b)). These results indicate that the dehydrogenation properties of MgH_2 were not influenced by the different inert gases. On the other hand, in the p-DSC profile under ~0.5 MPa H_2 (Fig. 4-1 (c)), the decomposition temperature of MgH_2 (~380 °C) is higher than that under an inert gas flow, and then the hydrogen pressure in the closed system rises to ~0.6 MPa at this temperature. This indicates that the decomposition reaction of MgH_2 is suppressed by hydrogen pressure until ~380 °C because the calculated decomposition temperature of MgH_2 under 0.6MPa is ~376 °C [4-4]. Additionally, it is noted that a sharp endothermic reaction at 445 °C in Fig. 4-1 (c) is not an essential because this reaction corresponds to a reaction between Mg and an Al pan to form Mg-Al compound and this reaction occurs partially. After performing these thermal analyses, the existence of Mg was confirmed by XRD (results are not shown) for all the conditions.

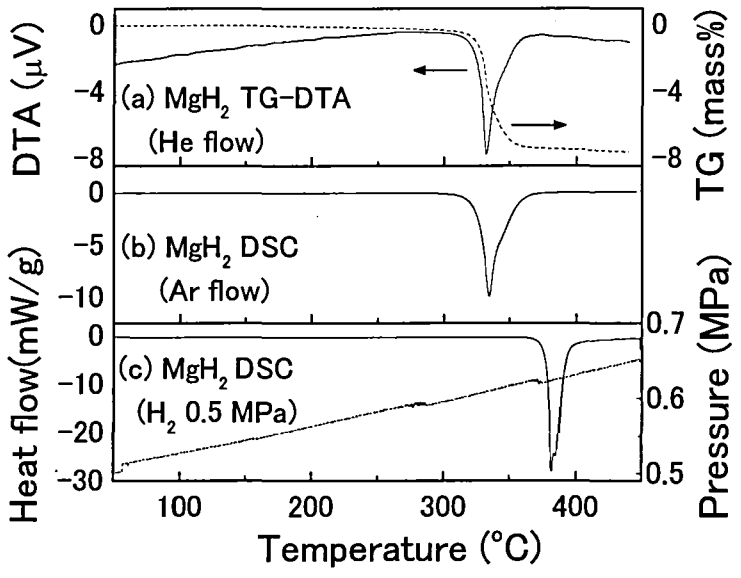

Figure 4-1. (a) TG-DTA profile under He flow and p-DSC profile (b) under Ar flow (c) under ~0.5 MPa H_2 for MgH_2.

Figure 4-2 shows the results of the thermal analyses for the $LiBH_4$. Two endothermic peaks and an endothermic profile are observed in the DTA and p-DSC profile under He flow (Fig. 4-2 (a)), which is almost the same as the p-DSC profile under Ar flow condition as shown in Fig. 4-2 (b). Respective peak temperatures are located at ~115 and ~280 °C, and the starting temperature of the endothermic profile is observed above 400 °C. By comparing the present results with the results reported by Fedneva *et al.* [4-5] and Soulié *et al.* [4-6], these peaks are assigned to the phase transition (~115 °C, orthorhombic to hexagonal phase), the melting phenomenon (~280 °C), and the decomposition reaction of $LiBH_4$ into LiH, B, and H_2 (above 400 °C), respectively. No peak is observed during the cooling process (Fig. 4-2 (b)), indicating that the decomposition reaction of $LiBH_4$ has been completed under an inert gas flow condition. On the other hand, under ~0.5 MPa H_2 in the closed system, two endothermic peaks are observed below 300 °C as shown in Fig. 4-2 (c), but there is no other reaction above

300 °C. These two peaks are shown at the same temperatures as those under an inert gas flow conditions, indicating that the hydrogen pressure does not affect the temperatures of phase transition and melting phenomenon of $LiBH_4$. However, the third endothermic profile above 400 °C disappears in the p-DSC profile under ~0.5 MPa H_2, where the pressure rises to ~0.7 MPa at 450 °C. In addition, two sharp exothermic peaks appear during the cooling process (Fig. 4-2 (c)), which correspond to solidification (~260 °C) and phase transition (~100 °C) of $LiBH_4$. These results indicate that the hydrogen dissociation pressure of $LiBH_4$ is lower than 0.7 MPa at 450 °C because the calculated hydrogen dissociation pressure of $LiBH_4$ is ~0.2 MPa [4-7]. The existences of LiH or $LiBH_4$ were confirmed after performing thermal analyses under an inert gas flow or under H_2 by XRD, respectively (results are not shown).

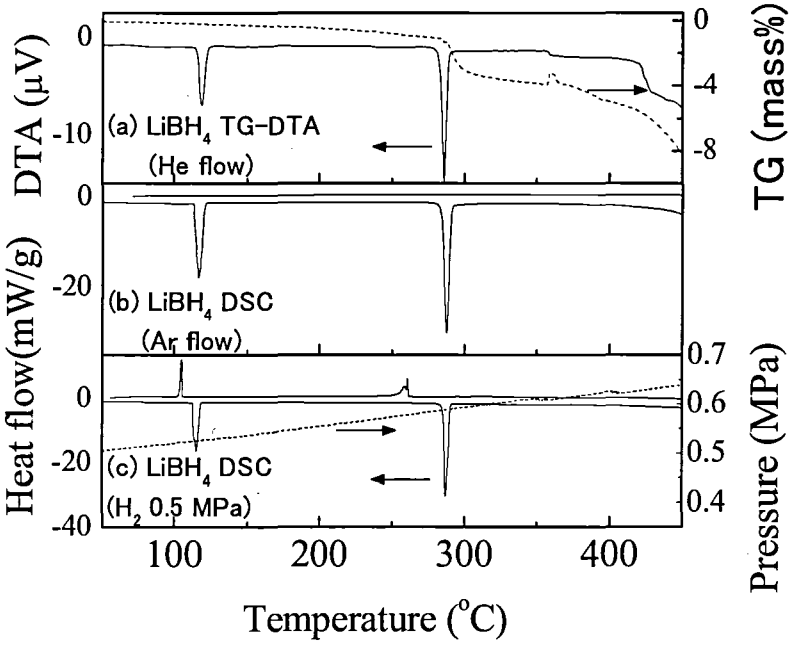

Figure 4-2. (a) TG-DTA profile under He flow and p-DSC profiles (b) under Ar flow and (c) under ~0.5 MPa H_2 for $LiBH_4$.

Figure 4-3 shows a TG-DTA profile under He flow and a p-DSC profiles under ~0.3 MPa Ar flow and ~0.5 MPa H_2 in the closed system for the MgH_2-$LiBH_4$ mixture which was obtained by ball-milling method described in Chapter 3. Additionally, XRD profiles of the MgH_2-$LiBH_4$ mixture before and after the dehydrogenation reaction are shown in Fig. 4-5. The result of the XRD indicates the presence of $LiBH_4$ and MgH_2 after milling (Fig. 4-5 (a)). In all the profiles, the two endothermic reactions below 300 °C are found as common behaviors. Comparing with the thermal analyses of MgH_2 and $LiBH_4$ (Figs. 4-1 and 4-2), these peaks correspond to the phase transition (~115 °C, orthorhombic to hexagonal phase) and the melting phenomenon (~280 °C) of $LiBH_4$. Above this temperature, the endothermic peak at ~370 °C under an inert gas flow and at ~390 °C under ~0.5 MPa H_2 correspond to the decomposition reaction of MgH_2. The most important behavior is observed above 400 °C. In the case of an inert gas flow condition (Figs. 4-3 (a) and (b)), the endothermic profile is observed above 400 °C, indicating that this profile corresponds to the decomposition reaction of $LiBH_4$ as shown in Fig. 4-2. Actually, LiH and Mg peaks are observed in the XRD profiles of these products (Fig. 4-5 (b)) although the peaks from boron were too weak to be detected by our XRD equipment. On the contrary, in the case of the measurement under hydrogen pressure in the closed system (Fig. 4-3 (c)), there is no reaction peak at 400~450 °C except for the unessential sharp endothermic peak corresponding to the reaction between Mg and an Al pan at 445 °C. This result indicates no decomposition reaction of $LiBH_4$ occurs. In the cooling process, strong exothermic peaks corresponding to solidification (~260 °C) and phase transition (~100 °C) was observed if $LiBH_4$ remains, but their peak intensities are too weak, indicating that $LiBH_4$ reacted with Mg during keeping at 450 °C. As shown in Fig. 4-4 (b), a weak endothermic peak appears in the case of keeping at

450 °C. This result indicates that this peak corresponds to a reaction between $LiBH_4$ and Mg to form MgB_2, LiH, and H_2. In fact, there are peaks corresponding to MgB_2 and LiH in the XRD profile of the product via keeping at 450 °C (Fig. 4-5 (c)). On the contrary, no peaks is observed in the keeping at 450 °C and cooling process under Ar flow (Fig. 4-3 (a)), indicating $LiBH_4$ decomposed at 400~450 °C. From above results, it is clarified that the solid-liquid reaction between solid Mg and liquid $LiBH_4$ to form MgB_2 proceeds by suppressing the decomposition reaction of $LiBH_4$.

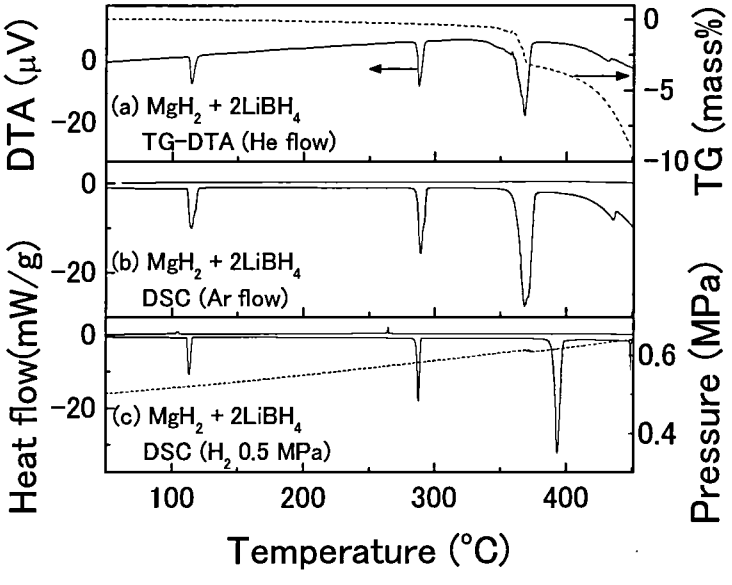

Figure 4-3. (a) TG-DTA profile under He flow and p-DSC profiles (b) under Ar flow and (c) under ~0.5 MPa H_2 for the mixture of MgH_2 and $2LiBH_4$.

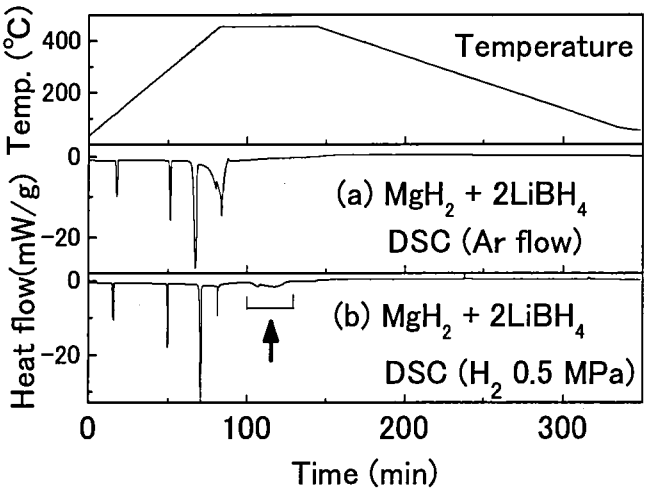

Figure 4-4. Time dependence of the p-DSC profiles of the mixture of MgH_2 and $2LiBH_4$ (a) under Ar flow and (b) under ~0.5 MPa H_2.

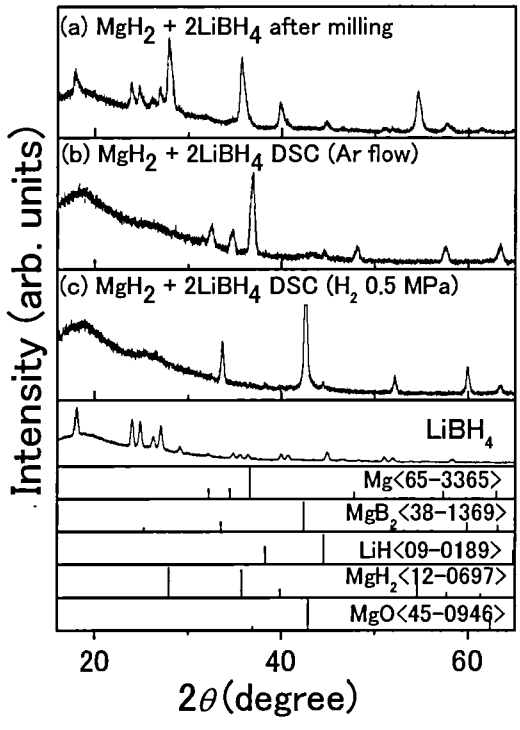

Figure 4-5. XRD profiles of (a) after milling (b) after TG-DTA measurement under He flow, which is same profile as that of p-DSC measurement under Ar flow, and (c) after p-DSC measurement under ~0.5 MPa H_2 for the MgH_2-$LiBH_4$ mixture together with the data of the JCPDS files.

In principle, MgB_2 should be formed by heating under an inert gas flow condition because the reaction between Mg and B to form MgB_2 is exothermic (ΔH: -91.96 kJ/mol [4-7]) and proceeds above 900 °C [4-8]. These facts indicate that the activation energy of the reaction between Mg and B to form MgB_2 (E_{ss}) would be quite high. Therefore, MgB_2 should be formed by the decomposition reaction of the MgH_2-$LiBH_4$ mixture regardless of the atmosphere. In addition, comparing the calculated Gibbs free energy of dehydrogenated states of this system at 450 °C [4-7], ΔG for the reaction of Eq. (4-2) is lower than that of Eq. (4-1) even under quite low hydrogen pressure (Fig. 4-6). However, the reaction of Eq. (4-1) proceeds under an inert gas condition. These results indicate that the activation energy of the reaction between Mg and $LiBH_4$ (E_{sl}) is higher than that of the decomposition reaction of $LiBH_4$ (E_{dec}). Considering above results, it is deduced that the hydrogen pressure changed the reaction path of forming MgB_2 into the reaction between Mg and $LiBH_4$, in other words, the hydrogen pressure thermodynamically suppressed the decomposition reaction of $LiBH_4$ and the direct reaction between Mg and $LiBH_4$ was realized at 450 °C without forming boron. Threfore, it is suggested that the relationship of the activation energies of E_{ss}, E_{sl}, and E_{dec} can be described as follows,

$$E_{ss} > E_{sl} > E_{dec}. \qquad (4\text{-}3)$$

The reason, why E_{sl} is lower than E_{ss}, would be because a diffusion of B is accelerated by the existence of the liquid phase of $LiBH_4$. The rate-determining step would be the atomic diffusion process.

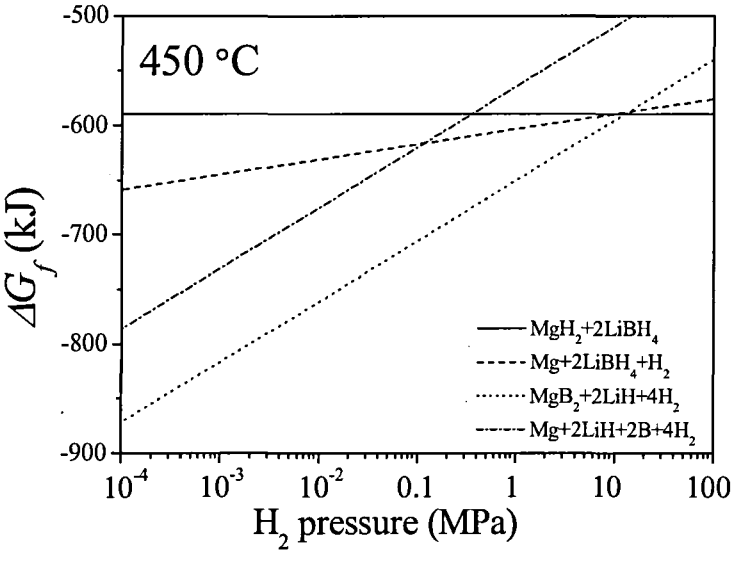

Figure 4-6. Pressure dependence of Gibbs free energy for the Li-Mg-B-H system.

4-1-2-2 The CaH_2-$LiBH_4$ mixture

The thermal decomposition properties of the CaH_2-$LiBH_4$ mixture, which is obtained by milling of CaH_2 and 6$LiBH_4$, were investigated by thermal analyses. Figure 4-7 shows the TG-DTA profile of CaH_2 and Fig. 4-8 shows the TG-DTA and the p-DSC profiles of the CaH_2-$LiBH_4$ mixture under different conditions. As shown in Fig. 4-7, CaH_2 does not decompose below 450 °C because the weight loss is ~0 mass%. For the CaH_2-$LiBH_4$ mixture, two endothermic peaks are clearly observed at ~115 °C and ~280 °C regardless of the atmosphere (Figs. 4-8 (a) and (b)), and a endothermic profile is observed above 350 °C under an inert gas flow (Fig. 4-8 (b)). These profiles are almost the same as those of $LiBH_4$ itself (Fig. 4-2). Thus, it is authenticated that three endothermic peaks in Figs. 4-8 (a) and (b) correspond to the phase transition (~115 °C), the melting phenomenon (~280 °C), and the decomposition reaction of $LiBH_4$ (above 350 °C under an inert gas flow), respectively. An endothermic profile is observed at

~450 °C under ~0.5 MPa H_2. In the case of the isothermal measurement at 450 °C under ~0.5 MPa H_2, a small endothermic peak is observed as shown in Fig. 4-9.

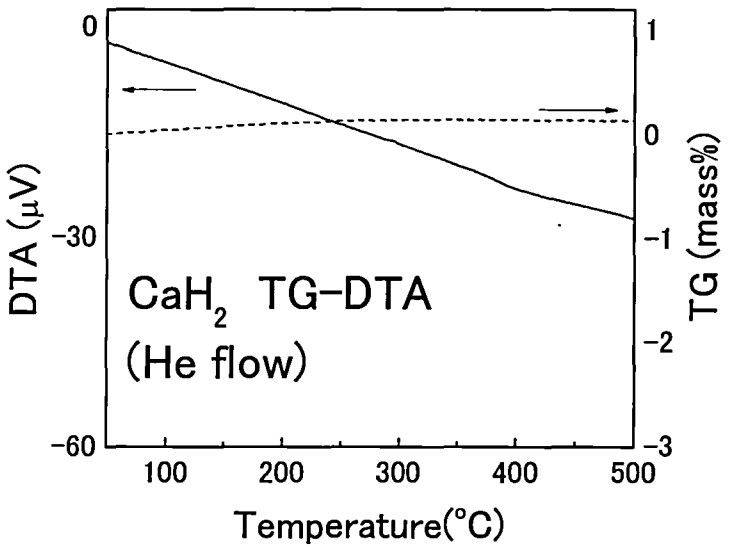

Figure 4-7. TG-DTA profile under He flow for CaH_2.

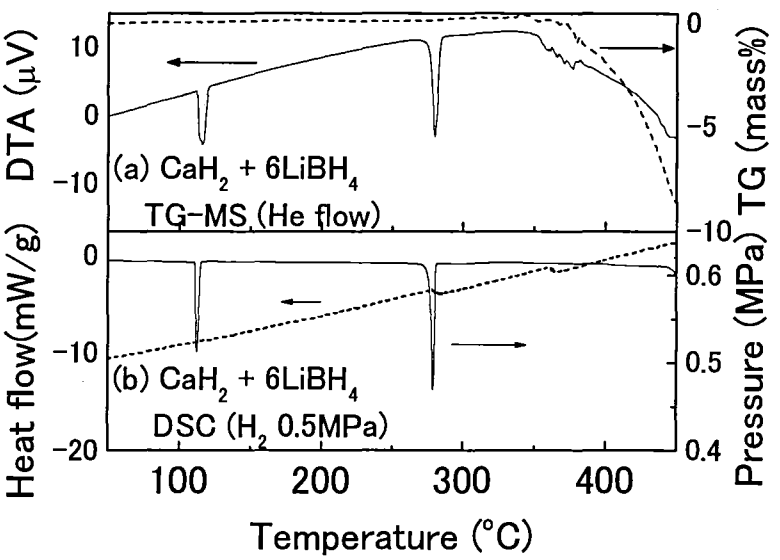

Figure 4-8. (a) TG-DTA profile under He flow and (b) p-DSC profile under ~0.5 MPa H_2 for the CaH_2-$LiBH_4$ mixture.

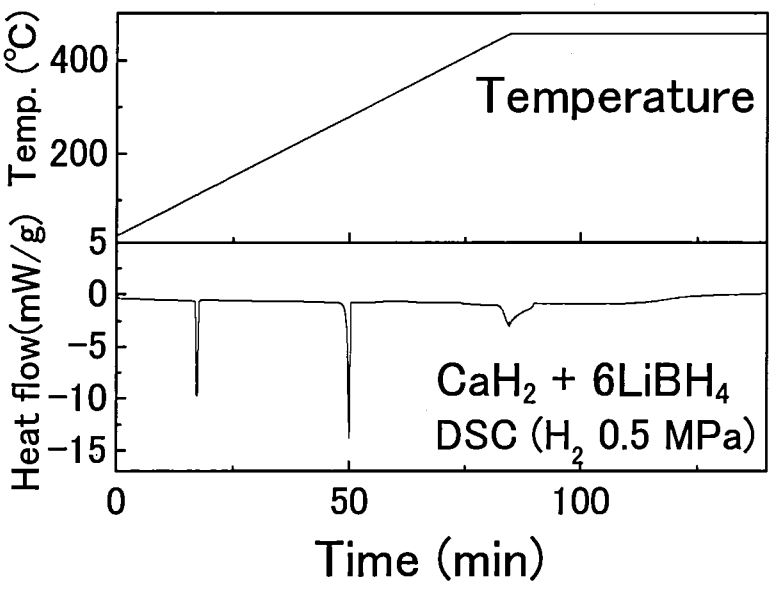

Figure 4-9. Time dependence of the p-DSC profile for the CaH_2-$LiBH_4$ mixture under ~0.5 MPa H_2.

Figure 4-10 shows the XRD profiles of the CaH_2-$LiBH_4$ mixture before and after the dehydrogenation reaction under different conditions. Before heating, both CaH_2 and $LiBH_4$ peaks are observed (Fig. 4-10 (a)). After the dehydrogenation reaction under an inert gas flow, CaH_2 and LiH peaks are observed (Fig. 4-10 (b)), although the peaks from boron were too weak to be detected by our XRD equipment. On the contrary, the small peaks corresponding to CaB_6 are observed after the isothermal measurement at 450 °C under ~0.5 MPa H_2 (Fig. 4-10 (c)). The peaks corresponding to LiH would exist on the analogy of the MgH_2-$LiBH_4$ mixture, suggesting the LiH peaks would be too weak to be detected.

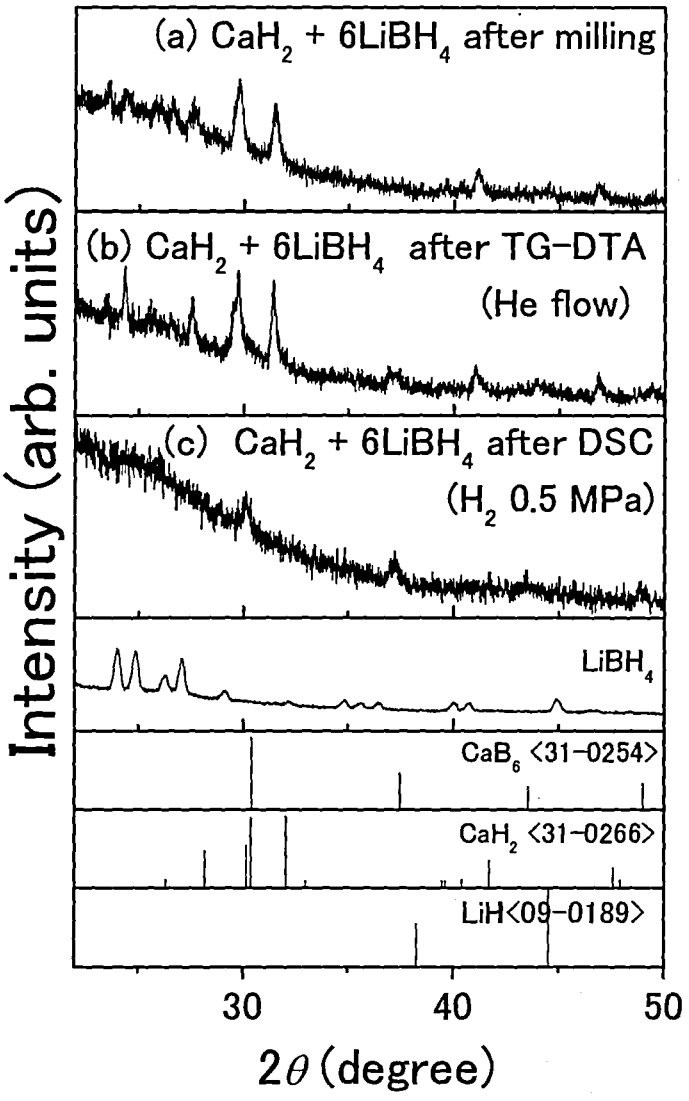

Figure 4-10. XRD profiles of (a) after milling, (b) after TG-DTA measurement under He flow and (c) after p-DSC measurement under ~0.5 MPa H_2 for the CaH_2-$LiBH_4$ mixture together with the data of neat $LiBH_4$ and the JCPDS files.

From above results, it is found that the reaction steps of the CaH_2-$LiBH_4$ mixture can be described as follows. Below 350 °C, the following phase transitions proceed with increasing temperature regardless of the atmosphere,

$$CaH_2 + 6LiBH_4(o) \rightarrow CaH_2 + 6LiBH_4(h), \quad (4\text{-}4)$$

$$\rightarrow CaH_2 + 6LiBH_4(liq), \quad (4\text{-}5)$$

where $LiBH_4$(o), $LiBH_4$(h), and $LiBH_4$(liq) are the orthorhombic, hexagonal and liquid phases of $LiBH_4$, respectively. At higher temperatures above 350 °C, the reaction path depends on atmosphere. In the case under an inert gas flow condition, the following decomposition reaction proceeds,

$$CaH_2 + 6LiBH_4(liq) \rightarrow CaH_2 + 6B + 6LiH + 9H_2. \quad (4\text{-}6)$$

On the other hand, the following reaction proceeds under hydrogen pressure,

$$CaH_2 + 6LiBH_4(liq) \rightarrow CaB_6 + 6LiH + 10H_2. \quad (4\text{-}7)$$

Here, Eq. (4-7) would be a solid-liquid reaction. As shown in Fig. 4-11, the calculated Gibbs free energy of the reaction of Eq. (4-6) is lower than that of Eq. (4-7) at 450 °C in even under quite low hydrogen pressure as well as Li-Mg-B-H system [4-7, 4-9]. In principle, CaB_6 should be formed at higher temperature under an inert gas flow condition because CaH_2 decomposes at 675 °C [4-10] and CaB_6 forms at 1000 °C by the reaction between Ca and B [4-11]. Considering these results and the results of the Li-Mg-B-H system, hydrogen would suppress the decomposition reaction of $LiBH_4$ and would change the reaction path of forming CaB_6 into the reaction between CaH_2 and $LiBH_4$. In addition, in the case under hydrogen pressure condition, the dehydrogenation temperatures of the CaH_2-$LiBH_4$ mixture which forms CaB_6 and that of the MgH_2-$LiBH_4$ mixture which forms MgB_2 are almost identical. However, the calculated enthalpy changes of the reaction between Mg and $LiBH_4$ to form MgB_2 (~36.0 kJ/mol H_2) are different from that of the reaction between CaH_2 and $LiBH_4$ to form CaB_6 (~47 kJ/mol H_2) [4-7, 4-9]. From these results, it is deduced that the kinetics of the decomposition of $M'H_m$ does not so effect on the dehydrogenation kinetics of the

forming $M'B_m$ by the reaction between $M'H_m$ and $M(BH_4)_n$, though the stability of $M'H_m$ was thought to be important for the thermodynamics of the system.

Considering the results of the MgH_2-$LiBH_4$ and the CaH_2-$LiBH_4$ mixtures, it is suggested that the following conditions are required to form $M'B_m$ by the reaction between $M'H_m$ and $M(BH_4)_n$; (1) to suppress the decomposition of $M(BH_4)_n$ by hydrogen pressure (2) to accelerate the diffusion of B by existence of liquid phase of $M(BH_4)_n$ at the reaction temperature.

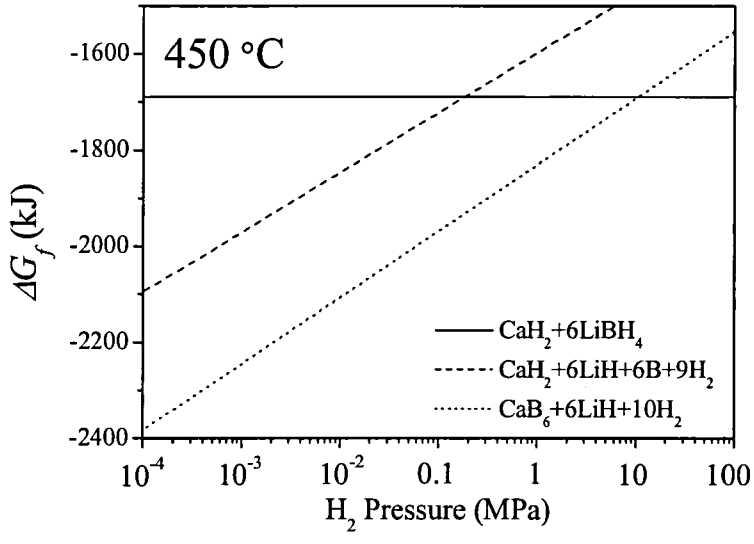

Figure 4-11. Pressure dependencies of Gibbs free energy for the Li-Ca-B-H system.

4-1-2-3 The MgH_m-$Zn(BH_4)_2$ mixtures

In the Section 4-1-2-1 and 4-1-2-2, it was clarified that $M'B_m$ is formed by the solid-liquid reaction between solid $M'H_m$ (m = 0 and 2) and liquid $LiBH_4$. Therefore, it was deduced that a diffusion of B atom would be important for the kinetics of the reaction between $M'H_m$ and $M(BH_4)_n$. In this point of view, gas-solid reaction would be more effective for the diffusion of B atom. Here, $Zn(BH_4)_2$ desorbs not only H_2 but also

gaseous diborane B_2H_6 at low temperature after melting phenomenon [4-12]. B_2H_6 is active gas, so it is expected that the gas-solid reactions occur between B_2H_6 and $M'H_m$. On the other hand, in the Li-N-H system, the reaction between LiH and $LiNH_2$ proceed through the following two elementary reaction steps mediated by ammonia [4-13],

$$2LiNH_2 \rightarrow Li_2NH + NH_3, \quad (4\text{-}8)$$

$$LiH + NH_3 \rightarrow LiNH_2 + H_2. \quad (4\text{-}9)$$

This mechanism was clarified by comparing the gas emission profiles of $LiNH_2$ and two-layered samples, in which LiH is put directly on the $LiNH_2$ [4-13]. By analogy with these results, it is expected that the reactions between MgH_m and $Zn(BH_4)_2$ proceed to form MgB_2 through the following two elementary reaction steps,

$$Zn(BH_4)_2 \rightarrow Zn + B_2H_6 + H_2, \quad (4\text{-}10)$$

$$MgH_m + B_2H_6 \rightarrow MgB_2 + (3 + m/2)H_2, \quad (4\text{-}11)$$

where $m = 0$ and 2. Therefore, in this work, the reactions between MgH_m and $Zn(BH_4)_2$ were investigated in order to examine the condition of forming MgB_2.

Preliminary, $Zn(BH_4)_2$ were synthesized by milling of $ZnCl_2$ and $2NaBH_4$. Therefore, $Zn(BH_4)_2$ contains sodium chloride NaCl as a by-product. Usually, this kind of by-product is removed by using solvent and then the solvent is removed by the heat treatment. However, because $Zn(BH_4)_2$ is too unstable to heat up, NaCl could not be removed from $Zn(BH_4)_2$ by using this method. .And then, in order to obtain obvious results of reactivity between MgH_m and B_2H_6, active MgH_m were prepared because neat MgH_2 and Mg are inactive. As active MgH_m, Nb_2O_5-doped MgH_2 and its dehydrogenated sample (Nb_2O_5-doped Mg) were used in this work. These samples are quite active because Nb_2O_5-doped MgH_2 desorbs hydrogen at 200~250 °C and Nb_2O_5-doped Mg absorbs hydrogen at room temperature as reported by Hanada *et al.*

[4-14]. The details of sample preparations for $Zn(BH_4)_2$ and MgH_m were described in Chapter 3.

First of all, reactivity between MgH_m and B_2H_6 were examined. By analogy with Li-N-H system, the gas emission properties of the two-layered MgH_m-$Zn(BH_4)_2$ (m = 0 and 2) samples, in which a large amount of MgH_m are put directly on $Zn(BH_4)_2$, respectively, are investigated. Figures 4-12 (a), (b), and (c) show the gas emission properties of $Zn(BH_4)_2$ and the two-layered MgH_m-$Zn(BH_4)_2$ (m = 0, 2) samples. In Fig. 4-12 (a), the $Zn(BH_4)_2$ powder starts to emit H_2 and diborane B_2H_6 from ~85 °C and the peak temperatures of these gases are located at around 125 °C. The peak area ratio of B_2H_6/H_2 in the profile of gas emission of $Zn(BH_4)_2$ is 17.2% (Fig. 4-12 (a)). For the two-layered MgH_m-$Zn(BH_4)_2$ samples as shown in Figs. 4-12 (b) and (c), the B_2H_6 emission is significantly suppressed compared with that from $Zn(BH_4)_2$ itself, where the B_2H_6/H_2 ratios of the two-layered MgH_m-$Zn(BH_4)_2$ (m = 0 and 2) samples are 2.1 % and 5.4 %, respectively, as shown in Figs. 4-12 (b) and (c). These results indicate that MgH_m react with B_2H_6 desorbed from $Zn(BH_4)_2$ by a gas-solid reaction.

Secondly, the thermal decomposition properties of the hand-milled MgH_m-$Zn(BH_4)_2$ (m = 0 and 2) samples, which are prepared by hand milling Nb_2O_5-doped MgH_m and $Zn(BH_4)_2$ in agate mortar, were investigated. As shown in Figs. 4-12 (d) and (e), B_2H_6 emission is also suppressed in both cases compared with that of $Zn(BH_4)_2$ itself, where the B_2H_6/H_2 ratios of the hand-milled MgH_m-$Zn(BH_4)_2$ samples are 6.0% and 8.0%, respectively. In addition, it is noteworthy that the shape of gas emission curves in Figs. 4-12 (d) and (e) is significantly different from those of Figs. 4-12 (b) and (c). Furthermore, the peak temperatures corresponding to the decomposition reaction of the hand-milled MgH_m-$Zn(BH_4)_2$ samples are decreased below 100 °C, where the peak

temperatures of the hand-milled MgH_2-$Zn(BH_4)_2$ and hand-milled Mg-$Zn(BH_4)_2$ samples are ~100 and ~89 °C, respectively. Their structures or chemical states should not be changed before heating because hand-milled MgH_m-$Zn(BH_4)_2$ samples are only mixed by hand milling for 5 min, so the kinetics of the reaction between MgH_m and $Zn(BH_4)_2$ seems to be improved. These results indicate that MgH_m interacted with $Zn(BH_4)_2$, and then gaseous B_2H_6 emitted from $Zn(BH_4)_2$ quickly reacted with the solid state of MgH_m even under an inert gas flow condition. In other words, the reaction between MgH_m and $Zn(BH_4)_2$ can be understood by a gas-mediated model, which is similar to the reaction between LiH and $LiNH_2$ [4-13]. Thus, the reaction between MgH_m and $Zn(BH_4)_2$ would consist of two elementary reaction steps as described in Eqs. (4-10) and (4-11). However, both the reactions of hand-milled MgH_m-$Zn(BH_4)_2$ samples are exothermic (Figs. 4-13 (b) and (c)) in contrast to the endothermic reaction of $Zn(BH_4)_2$, which has a broad endothermic peak at ~125 °C after a sharp endothermic peak corresponding to the melting phenomenon at ~95 °C as reported by Jeon *et al.* (Fig. 4-13 (a)) [4-12]. This result indicates that the rehydrogenation reaction of this system would not proceed because exothermic dehydrogenation reaction requires extremely high pressure to proceed the hydrogenation reaction according to van't Hoff equation (see Eq. 1-25).

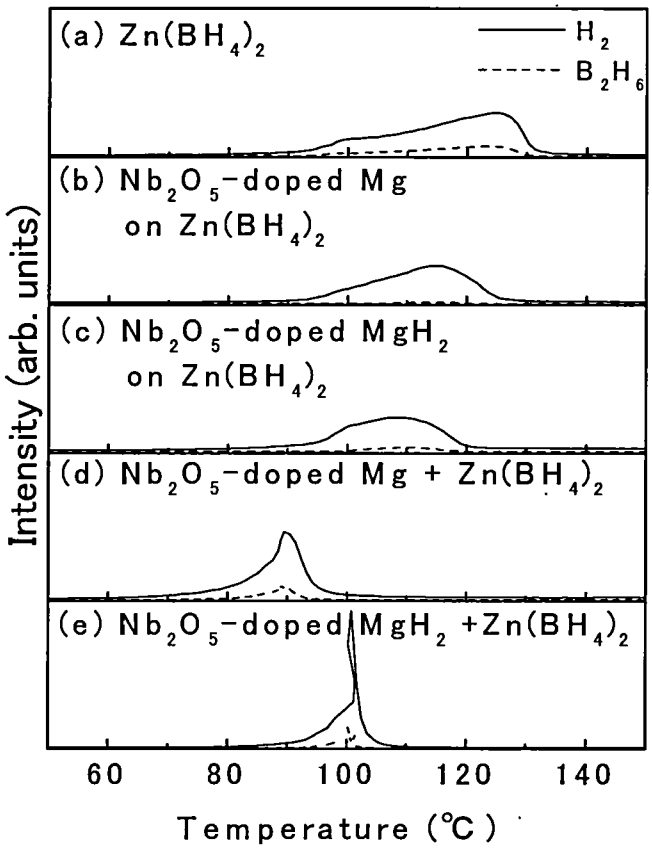

Figure 4-12. The gas emission properties of (a) $Zn(BH_4)_2$, (b) two-layered Mg-$Zn(BH_4)_2$ sample, (c) two-layered Mg H_2-$Zn(BH_4)_2$ sample, (d) the hand-milled Mg-$Zn(BH_4)_2$ sample, and (e) the hand-milled Mg H_2-$Zn(BH_4)_2$ sample. All samples contain NaCl.

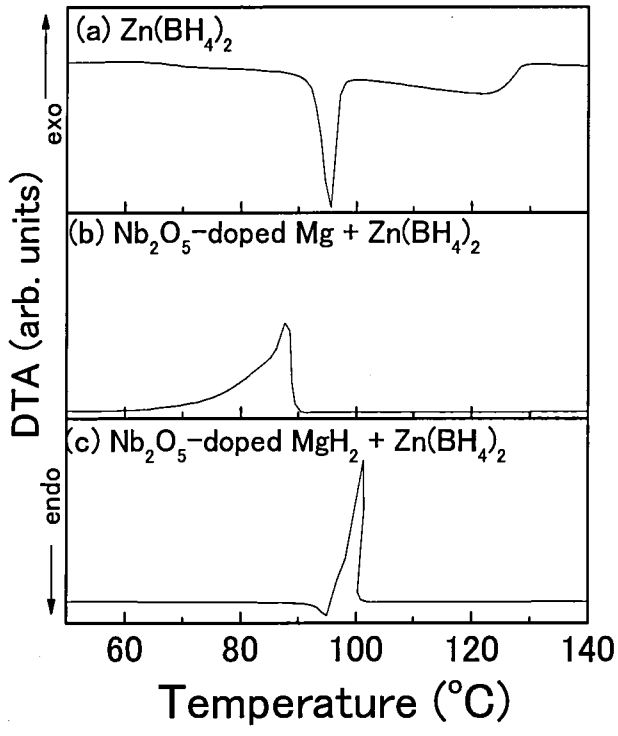

Figure 4-13. DTA profiles of (a) $Zn(BH_4)_2$, (b) hand-milled MgH_2-$Zn(BH_4)_2$ sample, and (c) hand-milled MgH_2-$Zn(BH_4)_2$ sample. All samples contain NaCl.

Figure 4-14 shows the XRD profiles of the hand-milled MgH_m-$Zn(BH_4)_2$ samples after heating up to 150 °C. In Figs. 4-14 (a) and (b), Zn and NaCl peaks observed. Zn and NaCl are the product of the $Zn(BH_4)_2$ after the decomposition reaction. In addition, in Figs. 4-14 (a) and (b), many unidentified peaks are observed although Mg or MgH_2 peaks are not observed. Here, the most important point in this system is to reveal whether MgB_2 is formed or not after the dehydrogenation reaction. However, no peak corresponding to MgB_2 was observed in both the XRD profiles (Figs. 4-14 (a) and (b)). To clarify the formation of MgB_2 in further detail, Raman scattering was carried out, and the results are shown in Fig. 4-15. As a result, MgB_2 peak should appear at ~500 cm^{-1}, but no peak is observed around 500 cm^{-1} in the Raman spectra of the hand-milled

MgH_m-$Zn(BH_4)_2$ samples after heating (Fig. 4-15). This result indicates that MgB_2 was not formed by the reaction between MgH_m and $Zn(BH_4)_2$. Although, the FT-IR spectra shows B-H vibrational modes in the hand-milled MgH_m-$Zn(BH_4)_2$ samples after heating as shown in Fig. 4-16. This result indicates that the reacted B atoms would be stored in the Mg atom by forming B-H bonding.

Considering the above results, it is supposed that the reaction between $M'H_n$ and $M(BH_4)_n$ does not form $M'B_m$ although the diffusion of B atom is accelerated by the gas-solid reaction between $M'H_n$ and B_2H_6 emitted from $M(BH_4)_n$. Thus, it would be required that no emission of B_2H_6 from $M(BH_4)_n$ would be used for forming $M'B_m$ by the reaction between $M'H_m$ and $M(BH_4)_n$.

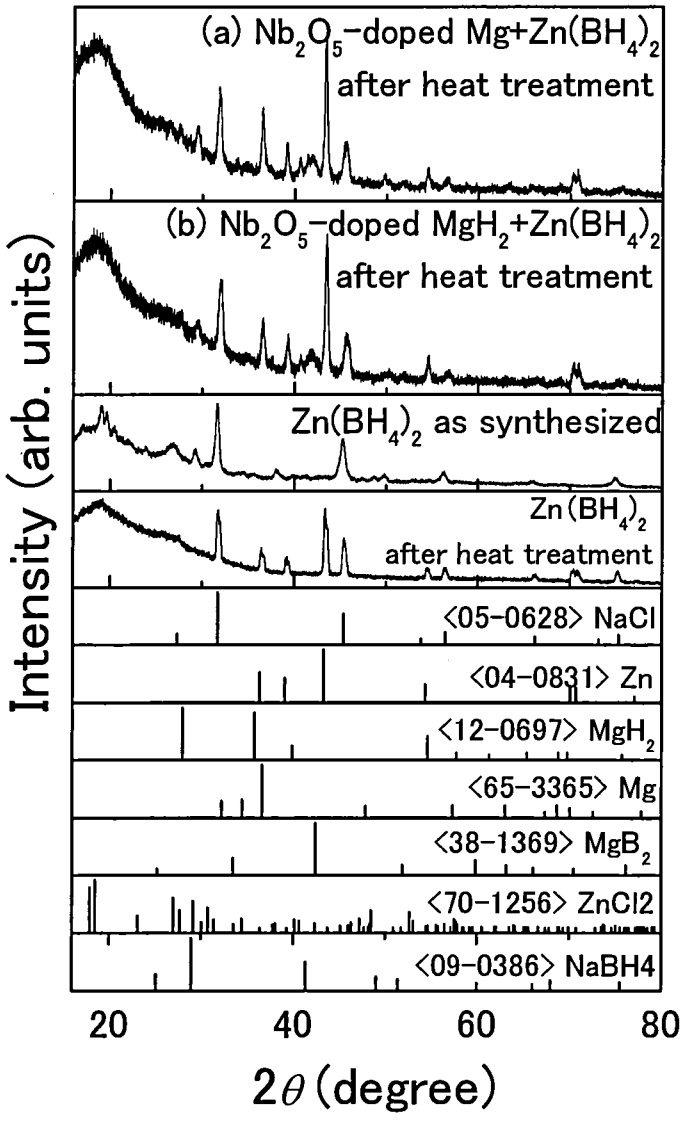

Figure 4-14. XRD profiles of the hand-milled (a)Mg-$Zn(BH_4)_2$ and (b) MgH_2-$Zn(BH_4)_2$ samples after heat treatment at 150 °C together with the data of the JCPDS files. Those of $Zn(BH_4)_2$ (+ 2NaCl) synthesized by milling and its after heat treatment at 150°C are also shown. All samples contain NaCl as by-product.

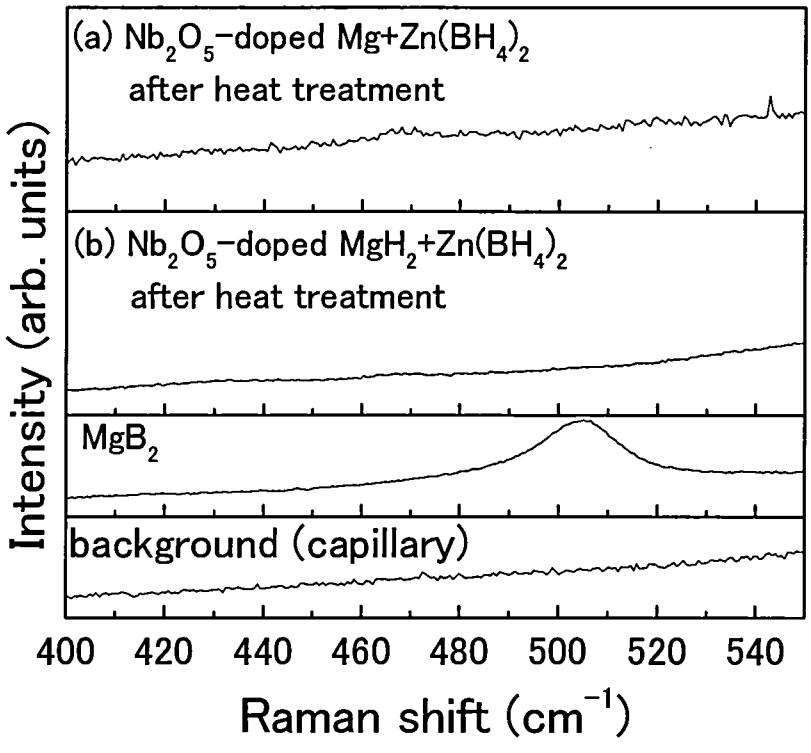

Figure 4-15. Raman spectra of the hand-milled (a) Mg-$Zn(BH_4)_2$ and (b) MgH_2-$Zn(BH_4)_2$ samples after heat treatment at 150 °C. Those of MgB_2 and background are also shown.

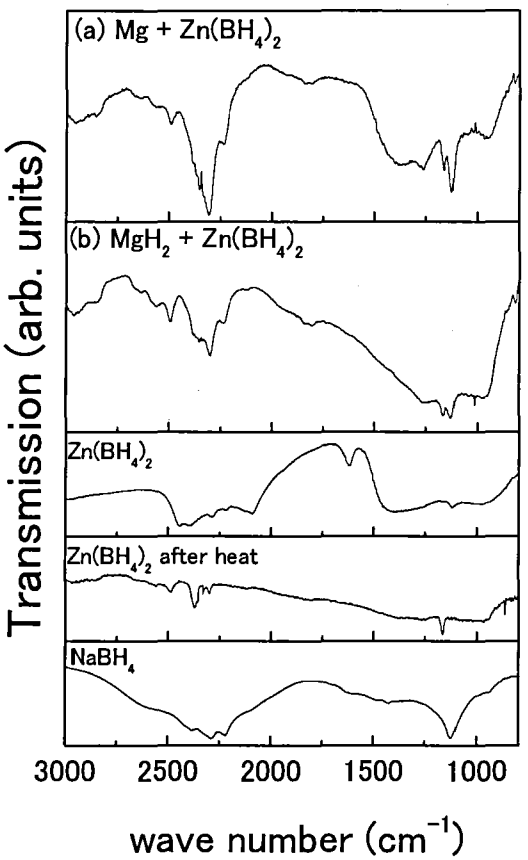

Figure 4-16. FT-IR spectra of the hand-milled (a) Mg-$Zn(BH_4)_2$ and (b) MgH_2-$Zn(BH_4)_2$ samples after heat treatment at 150 °C. Those of $Zn(BH_4)_2$ before and after heat treatment at 150 °C and $NaBH_4$ as references.

4-1-3 Summary

In this work, the condition of forming metal boride during the dehydrogenation process of the $M'H_n$-$M(BH_4)_n$ mixtures was investigated in order to understand how $M'B_m$ is formed in the process.

The thermal analyses of the MgH_2-$LiBH_4$ mixture and the MgH_2 and $LiBH_4$ powders were performed under the inert gas flow conditions and under ~0.5 MPa H_2 by TG-DTA and p-DSC measurements in order to examine these dehydrogenation processes. The

results showed that the endothermic peaks corresponding to the phase transition and melting of $LiBH_4$ and the decomposition reaction of MgH_2 were observed regardless of the atmosphere in the TG-DTA and p-DSC profiles of the MgH_2-$LiBH_4$ mixture. After that, the endothermic peak corresponding to the decomposition reaction of $LiBH_4$ was observed under inert gas condition. Under ~0.5 MPa H_2, the isothermal measurement at 450 °C showed that the small endothermic peak was observed although $LiBH_4$ does not decompose at 450 °C under ~0.5 MPa H_2. The XRD profile of the MgH_2-$LiBH_4$ mixture after heating up to 450 °C under an inert gas flow showed the existence of Mg and LiH, and that under ~0.5 MPa H_2 showed the existence of MgB_2 and LiH. From above results, it was clarified that the hydrogen pressure suppresses the decomposition reaction of $LiBH_4$ and MgB_2 is formed by the solid-liquid reaction between solid Mg and melted $LiBH_4$. From thermodynamic point of view, it was deduceed that the activation energy of the reaction between Mg and $LiBH_4$ should be lower than that of the reaction between Mg and B by accelerating the diffusion of B atom. This reason would be because of existence of liquid $LiBH_4$. However, activation energy of this solid-liquid reaction would be higher than that of the decomposition reaction of $LiBH_4$. Finally, it was suggested that the existence of hydrogen changes the reaction path of the reaction to form MgB_2 from Mg and $LiBH_4$ by thermodynamically suppressing the decomposition reaction of $LiBH_4$.

On the analogy of the MgH_2-$LiBH_4$ mixture, the thermal analysis of the CaH_2-$LiBH_4$ mixture was performed by TG-DTA and p-DSC measurements under an inert gas flow condition or under ~0.5MPa of hydrogen pressure. As a result, the same profile as $LiBH_4$ was observed below 440 °C under both conditions by TG-DTA and p-DSC. However, an endothermic peak was observed in the profile of the isothermal

measurement at 450 °C under ~0.5 MPa H_2. In the XRD profile, CaB_6 peaks observed after heat treatment under ~0.5 MPa H_2, while LiH and CaH_2 peaks were observed after heat treatment under an inert gas flow. These results indicated that CaH_2 reacted with $LiBH_4$ to form CaB_6 by solid-liquid reaction during the isothermal meaturement at 450 °C under ~0.5 MPa H_2 though decompositon reaction of $LiBH_4$ proceeded above 400 °C under an inert gas flow. Considering that CaH_2 should decompose to Ca and H_2 and CaB_6 should form by reacting between Ca and B at higher temperature, it was deduced that presence of hydrogen changes the reaction path into the reaction to form CaB_6 from CaH_2 and $LiBH_4$ by suppressing the decomposition reaction of $LiBH_4$ as well as for the case of the MgH_2-$LiBH_4$ mixture.

The thermal decomposition properties of the MgH_m-$Zn(BH_4)_2$ (m = 0 and 2) samples were investigated by DTA-MS measurement. The results showed that the B_2H_6 emission from the two-layered MgH_m-$Zn(BH_4)_2$ (m = 0 and 2) samples significantly decreased. The desorption temperatures of the hand-milled MgH_m-$Zn(BH_4)_2$ samples were lower than that of $Zn(BH_4)_2$ itself. These results indicated that the reaction between MgH_m and $Zn(BH_4)_2$ is composed of the two elementary reaction steps, which are B_2H_6 emission by the decomposition reaction of $Zn(BH_4)_2$ and the reaction between MgH_m and B_2H_6. However, these reactions are exothermic and no evidence of forming MgB_2 in the dehydrogenated state of the hand-milled MgH_m-$Zn(BH_4)_2$ samples was obtained by XRD and Raman scattering although the B-H vibrational modes were observed in the FT-IR profile of the after the dehydrogenation reaction of the hand-milled MgH_m-$Zn(BH_4)_2$ samples. Finally, it is supposed that no emission of B_2H_6 from $M(BH_4)_n$ is required for forming $M'B_m$ by the reaction between $M'H_m$ and $M(BH_4)_n$

4-2 Hydrogenation reaction of the MH_n-$M'B_m$ mixtures by milling technique

4-2-1 background and purpose

As mentioned in Chapter 2, hydrogenation kinetics of the *M*-B-H system at low temperature below 300 °C is too slow for the reaction to proceed completely. For example, the LiH-MgB_2 and the LiH-CaB_6 mixtures form the MgH_2-$LiBH_4$ and the CaH_2-$LiBH_4$ mixtures by hydrogenating at 350 °C under 10 MPa H_2 [4-1] and at 400 °C under 8.3 MPa H_2 [4-3], respectively. Considering these hydrogenation temperatures, more improvement of the hydrogenation kinetics is required.

Generally, the hydrogenation reaction is performed at high temperature under hydrogen pressure in the static condition. Recently, Kojima *et al.* has reported that the hydrogenation reaction of some nitrides proceed by millng at room tempearture under hydrogen pressure [4-15], indicating that the hydrogenation kinetics drastically improved by milling. On the analogy of this results, in order to improve the hydrogenation kinetics, using the milling under hydrogen pressure could be effective for the hydrogaenation reaction of the *M*-B-H systems. In this work, therefore, the milling effect on the *M*-B-H systems during hydrogenation was examined. First of all, the hydrogen storage properties of the LiH-$M'B_m$ (M' = Mg and Ca) mixtures which was milled under hydrogen pressure at room temperature were investigated by TG-MS, XRD, and FT-IR.

On the analogy of the LiH-$M'B_m$ (M' = Mg and Ca) mixtures, it is an interesting issue to determine how the reaction occurs by hydrogenating unreported MH_n-$M'B_m$ mixture. In this work, scandium hydride ScH_2 was used instead of LiH because it is predicted that the hydrogen storage system using ScH_2 would have a moderate enthalpy change

for hydrogen storage material of the fuel cell vehicle [4-9, 4-16]. Therefore, the hydrogen storage properties of the ScH_2-$M'B_m$ mixtures which were milled under hydrogen pressure at room temperature were investigated by TG-MS, FT-IR, SR-XRD, and XAS.

4-2-2 Results

4-2-2-1 Milling effect on the hydrogenation reaction of the LiH-$M'B_n$ (M' = Mg, Ca) mixture

Figures 4-17 (a) and (b) show the TG-MS profiles of the as-milled LiH-$M'B_m$ (M' = Mg and Ca) mixtures. As references, $M'B_m$ (M' = Mg and Ca) are also milled under hydrogen atmosphere and the results are shown in Fig. 4-17. Here, both MS profiles of the as-milled LiH-$M'B_m$ mixtures show the hydrogen desorption curves, indicating that hydrogen is stored in the LiH-$M'B_m$ mixtures during milling (Figs. 4-17 (a) and (b)). The as-milled LiH-MgB_2 and LiH-CaB_6 mixtures desorb ~3.6 mass% and ~1.9 mass% of hydrogen with a peak at ~350 °C and two peaks at ~240 and ~300 °C, respectively. Their weight losses with the hydrogen desorption are larger than that of the as-milled $M'B_m$, indicating that the LiH would have an ability to provide hydrogen to $M'B_m$. The expected weight losses of the MgH_2-$LiBH_4$ and the CaH_2-$LiBH_4$ mixtures are 11.4 mass% and 10.5 mass%, respectively if the following reactions proceed,

$$2LiH + MgB_2 + 4H_2 \rightarrow MgH_2 + 2LiBH_4, \quad (4\text{-}12)$$

$$6LiH + CaB_6 + 10H_2 \rightarrow CaH_2 + 6LiBH_4. \quad (4\text{-}13)$$

The weight losses of the as-milled LiH-$M'B_m$ mixtures are lower than the expected weight losses.

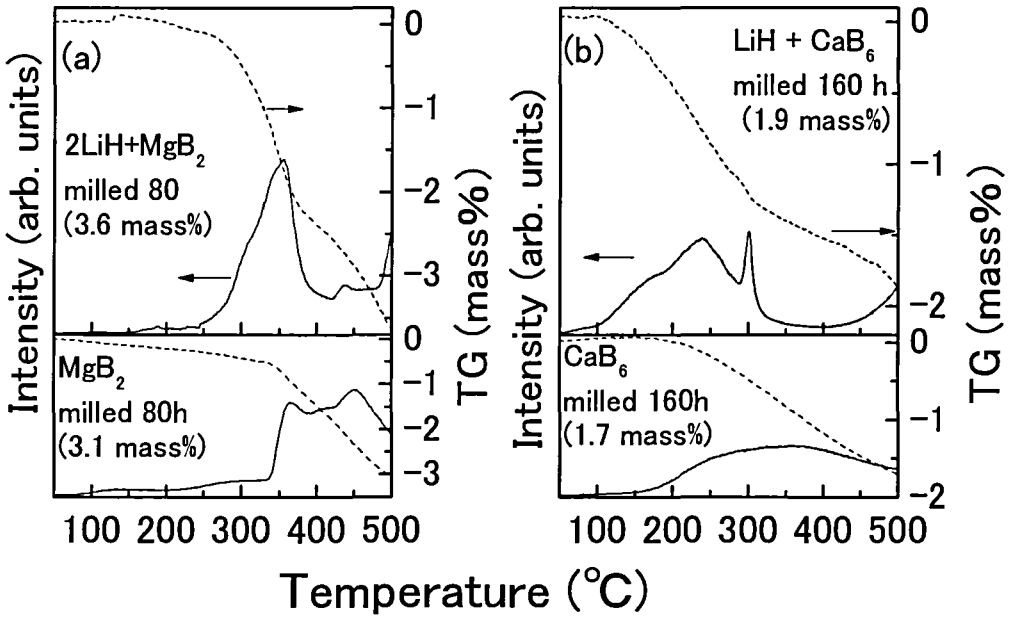

Figure 4-17. TG-MS profiles of the as-milled (a) LiH-MgB_2 and (b) LiH-CaB_6 mixtures. As references, those of as-milled MgB_2 and CaB_6 are also shown.

Figure 4-18 shows the XRD profiles of the as-milled LiH-$M'B_m$ mixtures before and after the dehydrogenation reaction. In the XRD profiles, weak peaks corresponding to unreacted $M'B_m$ and Fe (or unreacted LiH) are observed. This result is consistent with the TG-MS results. However, peaks corresponding to $M'H_m$ and $LiBH_4$ are not observed in the XRD profiles of the as-milled samples (the top profile in Fig. 4-18 (a) and (b)), indicating that $M'H_m$ and $LiBH_4$ peaks are too weak to detect because $M'H_m$ and $LiBH_4$ would be nanocrystalline phase or small amount of them would be generated. After the dehydrogenation reaction, the peaks corresponding to Mg and CaH_2 are also not observed in the XRD profiles.

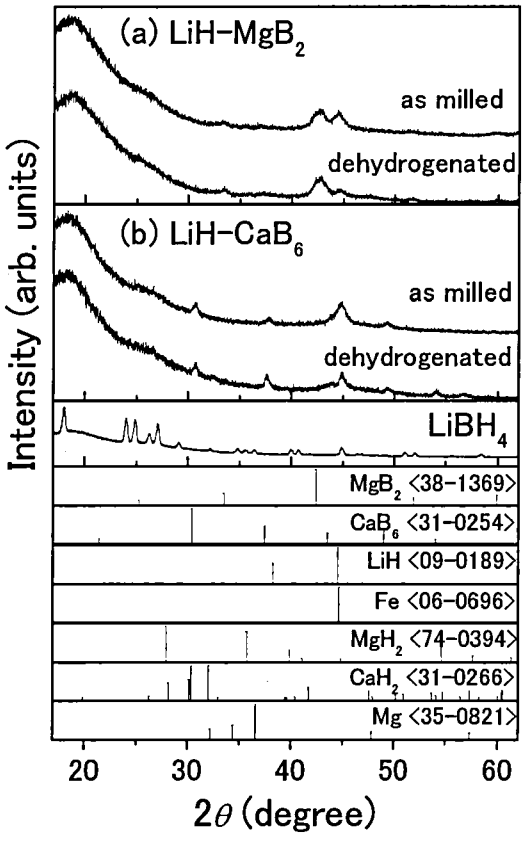

Figure 4-18. XRD profiles of the as-milled (a) LiH-MgB_2 and (b) LiH-CaB_6 mixtures before and after the dehydrogenation reaction.

Figure 4-19 shows the FT-IR spectra of the as-milled LiH-$M'B_m$ mixtures. The absorption peak corresponding to the B-H_t stretching mode at ~2300 cm^{-1} observed in both FT-IR spectra of the as-milled LiH-$M'B_m$ mixtures [4-17]. This result indicates that hydrogen is stored in the as-milled LiH-$M'B_m$ mixtures by forming the B-H bonding. However, These peaks are slightly different from that of $LiBH_4$. Considering that the $LiBH_4$ has a intermediate state such as $LiB_{12}H_{12}$ [4-18] as mentioned in Chapter 1, the intermediate state of $LiBH_4$ might be generated by milling the LiH-$M'B_m$ mixtures. From above results, it is expected that the hydrogenation reactions of the as-milled

LiH-$M'B_m$ mixtures are not completed and a longer milling time and/or a higher temperature are required to obtain complete hydrogenated samples.

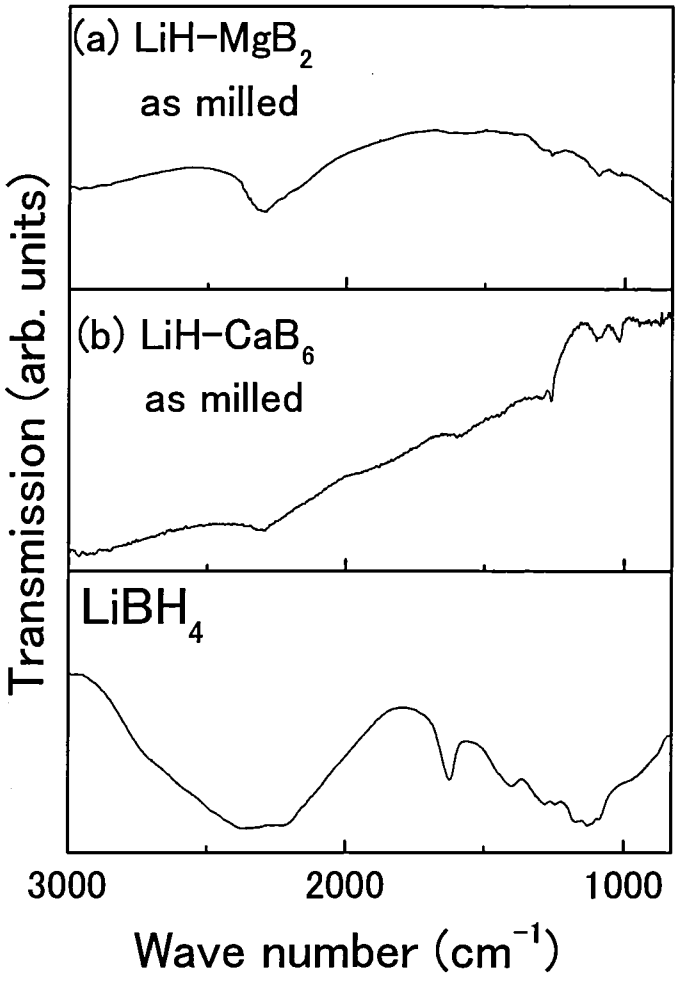

Figure 4-19. FT-IR spectra of the as-milled (a) LiH-MgB_2 and (b) LiH-CaB_6 mixtures. As a reference, the FT-IR spectrum of $LiBH_4$ is also shown.

4-2-2-2 Milling effect on the hydrogenation reaction of the ScH_2-$M'B_n$ (M' = Mg, Ca) mixture

Figures 4-20 (a) and (b) show the TG-MS profiles of the as-milled ScH_2-$M'B_m$ (M' =

Mg and Ca) mixtures with that of the as-milled $M'B_m$ (M' = Mg and Ca). Both MS profiles of the as-milled ScH_2-$M'B_m$ mixtures show the hydrogen desorption curves as well as that of the as-milled LiH-$M'B_m$ (M' = Mg and Ca) mixtures, indicating that hydrogen is also stored in the ScH_2-$M'B_m$ mixtures by milling (Figs. 4-20 (a) and (b)). The as-milled ScH_2-MgB_2 and ScH_2-CaB_6 mixtures desorb ~3.4 mass% and ~1.8 mass% of hydrogen, respectively (Figs. 4-20 (a) and (b)). These weight losses are larger than that of as-milled $M'B_m$, indicating the ScH_2 would have an ability to provide hydrogen to $M'B_m$ as well as LiH. The MS profiles of the as-milled ScH_2-MgB_2 and ScH_2-CaB_6 mixtures have a peak at ~240 °C and at ~250 °C, respectively (Figs. 4-20 (a) and (b)). The hydrogenated states of the ScH_2-$M'B_m$ mixtures have not been reported yet. By analogy with the reported results [4-1~3], the formation of $Sc(BH_4)_3$, which is reported by Nakamori *et al.* [4-19], as a component of the hydrogenated state of the ScH_2-$M'B_m$ mixtures are expected. If $Sc(BH_4)_3$ is formed by hydrogenating the ScH_2-$M'B_m$ mixtures, the following reactions are expected,

$$2ScH_2 + 3MgB_2 + 13H_2 \rightarrow 3MgH_2 + 2Sc(BH_4)_3 \quad (10.2 \text{ mass\%}), \quad (4\text{-}14)$$

$$2ScH_2 + CaB_6 + 11H_2 \rightarrow CaH_2 + 2Sc(BH_4)_3 \quad (10.0 \text{ mass\%}). \quad (4\text{-}15)$$

However, the weight losses obtained in this study are much less than the above expected values.

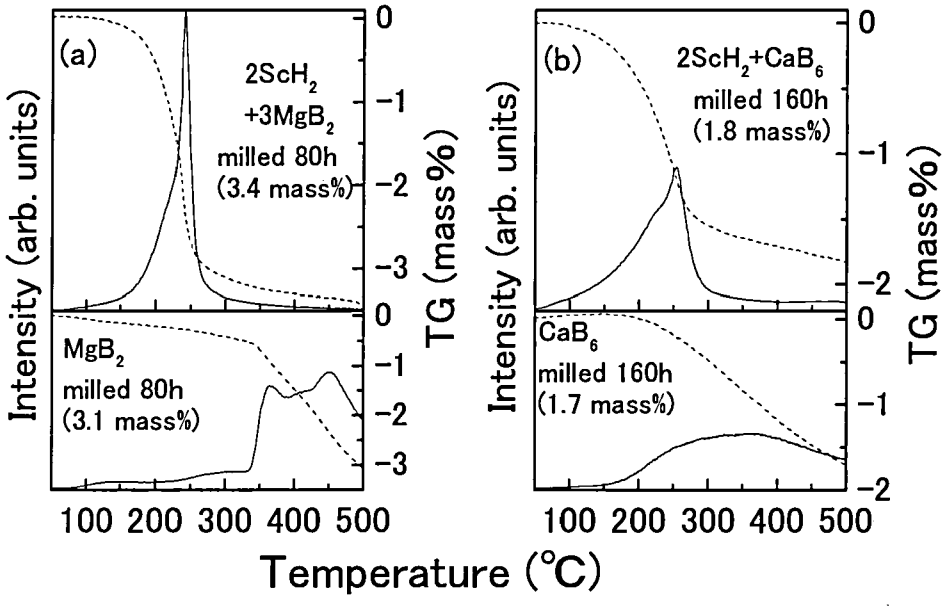

Figure 4-20. TG-MS profiles of the as-milled (a) ScH_2-MgB_2 and (b) ScH_2-CaB_6 mixtures. As references, those of as-milled MgB_2 and CaB_6 are also shown.

Figure 4-21 shows the FT-IR results of the as-milled ScH_2-$M'B_m$ mixtures and $Sc(BH_4)_3$ which is synthesized by milling $ScCl_3$ and $3LiBH_4$ [4-19]. First of all, it should be mentioned that an absorption peak at ~1600cm^{-1} and a convex peak at ~1400cm^{-1} are originated from the background as shown in Fig. 4-21 (d). The FT-IR spectra of the as-milled ScH_2-$M'B_m$ mixtures show the absorption peak corresponding to the B-H_t stretching and B-H_2 deformation modes around 2000~2500 cm^{-1} and 900~1500 cm^{-1} (Figs. 4-21 (a) and (b)), respectively [4-17]. However, their fine structures are different from that of $Sc(BH_4)_3$ (Fig. 14-21 (c)). Comparing their as-milled and dehydrogenated samples, the B-H vibrational modes disappear after the dehydrogenation reaction at 500 °C for 12 h (Figs. 4-21 (a) and (b)). These results indicate that hydrogen is stored in the as-milled ScH_2-$M'B_m$ mixtures by forming the B-H bonding, and is released by heating.

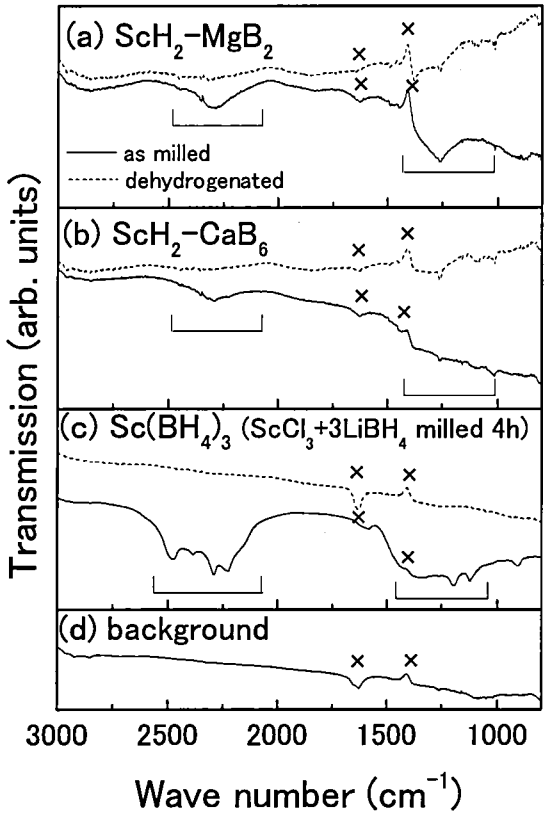

Figure 4-21. FT-IR spectra of the as-milled (a) ScH_2-MgB_2 and (b) ScH_2-CaB_6 mixtures before and after the dehydrogenation reaction. FT-IR spectra of (c) $Sc(BH_4)_3$ (synthesized by milling $ScCl_3$ and $LiBH_4$) before and after the dehydrogenation reaction and (d) background are also shown as a reference.

In order to characterize these products, the SR-XRD experiments were performed and the results are shown in Fig. 4-22. In the case of the as-milled ScH_2-CaB_6 mixture, ScH_2 peaks disappear but the peaks corresponding to ScB_2 are observed (Fig. 4-22 (a)). These results indicate that CaB_6 reacted with ScH_2 to form ScB_2 instead of $Sc(BH_4)_3$ by milling. In addition, it seems that ScB_2 remains after the dehydroganation reaction and the SR-XRD profile of the dehydrogenated ScH_2-CaB_6 mixture is almost the same as

that of the as-milled ScH_2-CaB_6 mixture. Moreover, it is noteworthy that two small peaks appeared at 5.5 ° and 5.9 ° in the as-milled ScH_2-CaB_6 mixture. These peaks disappear after the dehydrogenation reaction (inset of Fig. 4-22 (a)), indicating that these peaks could correspond to the hydrogenated state. It is also mentioned that unreacted CaB_6 is observed in the XRD profiles of the as-milled and the dehydrogenated ScH_2-CaB_6 mixtures.

For the as-milled ScH_2-MgB_2 mixture, ScH_2 peaks also disappear and the peaks corresponding to MgB_2 or ScB_2 are observed in the SR-XRD profile of the as-milled ScH_2-MgB_2 mixture (Fig. 4-23 (b)). This profile is almost the same as that of the dehydrogenated ScH_2-MgB_2 mixture. Since the XRD profile of MgB_2 is similar to that of ScB_2, it is difficult to identify which exists in the as-milled ScH_2-MgB_2 mixture. However, the observed peaks above 20 ° are slightly differnt from the MgB_2 peaks (Fig. 4-22 (b)). On the analogy of the as-milled ScH_2-CaB_6 mixtures, there is a possibility of forming ScB_2 by milling. Therefore, these peaks correspond to ScB_2 rather than MgB_2. These results indicate that ScH_2 also reacted with MgB_2 by milling. Considering the stoichiometric reaction and FT-IR results, MgB_2 is expected to change into other material which has B-H bonding. In addition, a broad and weak peak appears at around 5 ~ 7.5 ° in the as-milled ScH_2-MgB_2 mixture. This broad peak seems to grow up after the dehydrogenation reaction (inset of Fig. 4-22 (b)), indicating that this broad peak corresponds to Mg-related compound which may be nanocrystalline or amorphous phase and it is slightly crystallized by heating.

In both the as-milled and dehydrogenated ScH_2-$M'B_m$ mixtures, the peaks of Fe are also observed, which come from the steel balls and the vessel during milling process. Fe takes no effect on the hydrogen storage properties in these sytems because the same

hydrogen storage properties are shown in the case of the sapmles synthesized by using ZrO_2 balls.

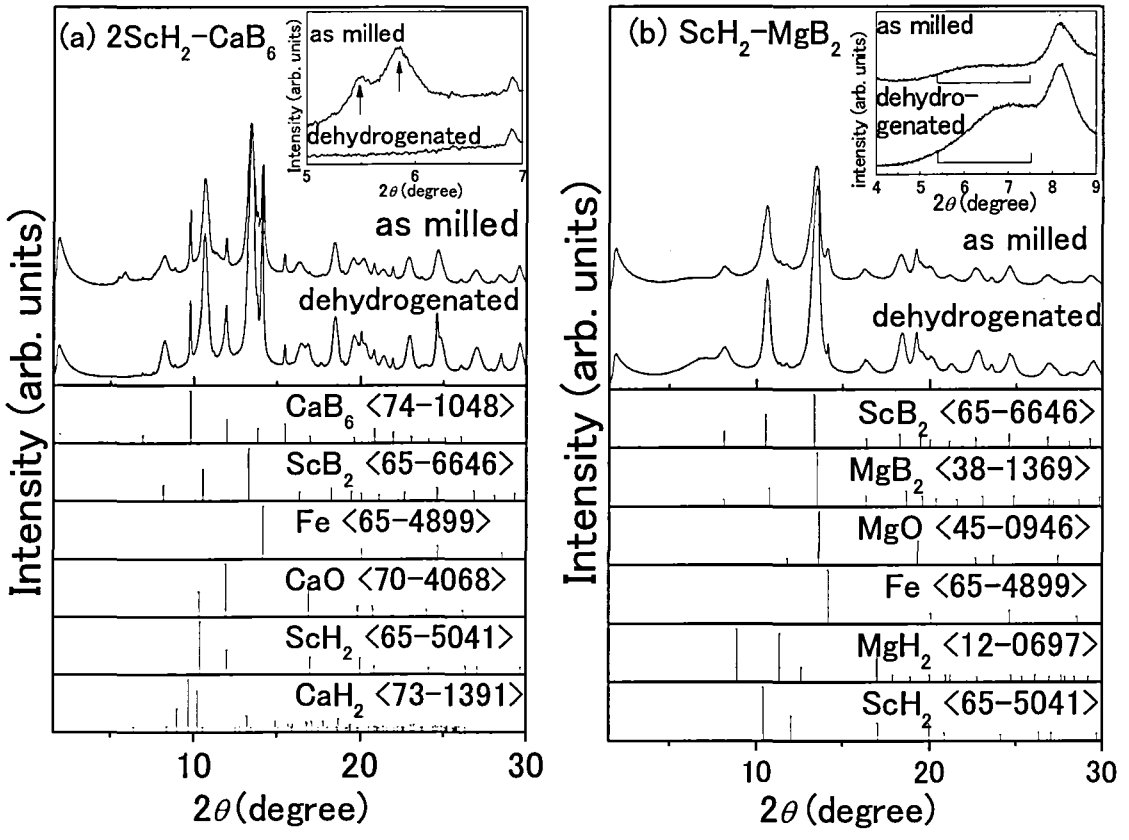

Figure 4-22. SR-XRD profiles of the as-milled (a) ScH_2-CaB_6 and (b) ScH_2-MgB_2 mixtures before and after the dehydrogenation reaction together with the data of JCPDS files.

The results of XAS corresponding to Sc *K*- and Ca *K*-edges are shown in Figs. 4-23. The samples of the as-milled and the dehydrogenated ScH_2-$M'B_m$ mixtures exhibit almost the same profiles in Sc *K*-edge XANES and EXAFS (Figs. 4-21 (a) and (b)). In addition, all the EXAFS profiles are close to that of ScB_2 measured as a reference (Fig. 4-21 (b)). These results indicate that ScH_2 reacted with $M'B_m$ to form ScB_2 by milling

the ScH_2-$M'B_m$ mixtures, and ScB_2 remains in the ScH_2-$M'B_m$ mixtures even after the dehydrogenation process. This result agrees well with the SR-XRD results although their XANES profiles are slightly different from ScB_2 profile.

Furthermore, Ca *K*-edge XANES and EXAFS profiles of the as-milled ScH_2-CaB_6 mixture is obviously different from that of the dehydrogenated one (Figs. 4-21 (c) and (d)). However, these profiles do not correspond to any references. Considering CaB_6 remains, the Ca-related phase would be composed of multiple phases. XAS analysis is not suitable to characterize the mixture composed of different compounds of the target elemnt, therefore it is difficult to identify what materials are genarated. Consequently, these results indicate that Ca atom in the CaB_6 releases some B atoms to Sc atom and is hydrogenated by milling. After that, this material would desorb hydrogen. This result is consistent with the results of Sc *K*-edge XAS measurement and SR-XRD although hydrogenated state could not be characterized.

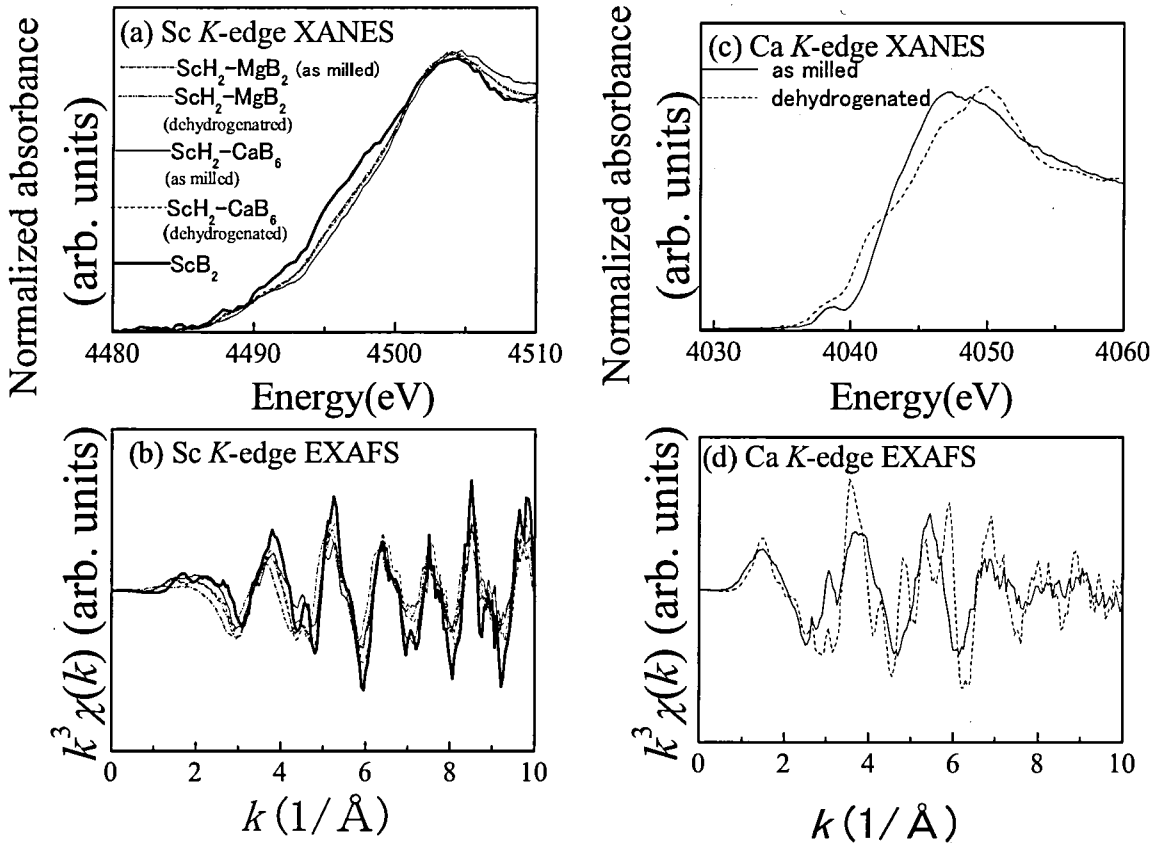

Fig. 4-23. (a) XANES profiles and (b) EXAFS profiles of Sc *K*-edge of the as-milled ScH_2-*M*'B_m mixtures before and after the dehydrogenation reaction, and (c) XANES profiles and (d) EXAFS profiles at Ca *K*-edge of the ScH_2-CaB_6 mixture before and after the dehydrogenation reaction.

Considering above results, it is clarified that the following reaction proceeds by milling under hydrogen pressure in this work,

$$ScH_2 + xM'B_m + yH_2 \rightarrow ScB_2 + x\text{“}M'\text{-B-H”}, \qquad (4\text{-}16)$$

where *M'* = Mg and Ca. It is suggested that the "*M'*-B-H" compounds dehydrogenate without reacting with ScB_2.

Finally, from the results of this section, it is suggested that MH_n would have an ability

to provide hydrogen to $M'B_m$ and hydrogen is stored in the MH_n-$M'B_m$ mixture by forming B-H bonding during milling under hydrogen pressure.

4-2-3 Summary

In this work, hydrogen storage properties of the MH_n-$M'B_m$ (M = Li and Sc, M' = Mg and Ca) mixtures which were milled under hydrogen pressure were investigated by TG-MS, FT-IR, XRD, SR-XRD, and XAS in order to examine the milling effect on the M-B-H systems during the hydrogenation reaction. As a result, all of the as-milled MH_n-$M'B_m$ mixtures revealed different MS profiles from that of the as-milled $M'B_m$ and their weight losses with the hydrogen desorption were larger than that of the as-milled $M'B_m$. For the LiH-$M'B_m$ mixtures (M' = Mg and Ca), the as-milled LiH-MgB_2 and the as-milled LiH-CaB_6 mixtures desorbed ~3.6 mass% and ~1.9 mass% of hydrogen, but their weight losses did not reach the expected weight losses of 11.4 mass% and 10.5 mass%, respectively. The XRD result showed that the unreacted $M'B_m$ were observed in the as-milled LiH-$M'B_m$ mixtures but the FT-IR results indicated that hydrogen was stored in the as-milled LiH-$M'B_m$ mixtures by forming the B-H bonding. From these results, it is deduced that the hydrogenation reactions of the LiH-$M'B_m$ mixtures were not completed. Therefore, a longer milling time and/or a higher temperature are required to obtain complete hydrogenated samples.

For the hydrogen storage properties of the ScH_2-$M'B_m$ mixture (M' = Mg and Ca), the as-milled ScH_2-MgB_2 and the as-milled ScH_2-CaB_6 mixtures desorbed ~3.4 mass% and ~1.8 mass% of hydrogen at ~240 °C and at ~250 °C, respectively. These weight losses were larger than the as-milled $M'B_m$, indicating that ScH_2 would have an ability to provide hydrogen to $M'B_m$ as well as LiH. In the FT-IR profiles, the absorption peak

corresponding to the B-H vibrational mode were observed and the peak disappeared after the dehydrogenation reaction, indicating that hydrogen was stored in the as-milled ScH_2-$M'B_m$ mixtures by forming the B-H bonding, and was released by heating. The SR-XRD and Sc *K*-edge XAS results showed that the ScB_2 was generated in the as-milled ScH_2-$M'B_m$ mixtures instead of ScH_2 and remained after dehydrogenation reaction. In addition, the Ca *K*-edge XAS profiles of the as-milled ScH_2-CaB_6 mixture were obviously different from dehydrogenated sample. This result indicated that Ca-related compound desorbed hydrogen. From above results, it was clarified that ScB_2 and "*M'*-B-H" compounds (*M'* = Mg and Ca) were generated during hydrogenation reaction by milling the ScH_2-$M'B_m$ mixtures at room temperature. It was suggested that hydrogen desorbed from B-H bonding in the "*M'*-B-H" compounds, which does not react with ScB_2.

Finally, from above results, it is suggested that MH_n would have an ability to provide hydrogen to $M'B_m$ and hydrogen is stored in the MH_n-$M'B_m$ mixture by forming B-H bonding during milling under hydrogen pressure.

References

[4-1] J. J. Vajo, S. L. Skeith and F. Mertens, *J. Phys. Chem. B* **109** (2005) 3719-3722.

[4-2] G. Barkhordarian, T. Klassen, M. Dronheim, and R. Bormann, *J. Alloys Compd.* **440** (2007) L18-L21.

[4-3] F.E. Pinkerton and M.S. Meyer, *J. Alloys Compd.* **464** (2008) L1-L4.

[4-4] Y. Fukai, K. Tanaka, and H. Uchida, *Hydrogen and Metal*, Uchidarokakuho, Japan, (1998) (in Japanese).

[4-5] E.M. Fedneva, V.L. Alpatova, and V.I. Mikheeva, *Russ. J. Inorg. Chem.* **9** (1964) 826-827.

[4-6] J-Ph. Soulié, G. Renaudin, R. Černỳ, and K. Yvon, *J. Alloys Compd.* **346** (2002) 200-205.

[4-7] National Institute of Standards and Technology, http://webbook.nist.gov/chemistry/.

[4-8] Y. Nakamori, S. Orimo, T. Ekino, and H. Fujii, *J. Alloys Compd.* **335** (2002) L21-L24.

[4-9] S.V. Alapati, J.K. Johnson, D.S. Sholl, *Phys. Chem. Chem. Phys.* **9** (2007) 1438-1452.

[4-10] P.P. Alexander, US patent, patent number: 2038402.

[4-11] R.W. Johnson and A.H. Daane, *J. Chem. Phys.* **38** (1963) 425-432.

[4-12] E. Jeon and Y.W. Cho, *J. Alloys Compd.* **422** (2006) 273-275.

[4-13] T. Ichikawa, N. Hanada, S. Isobe, H.Y. Leng, and H. Fujii, *J. Phys. Chem. B* **108** (2004) 7887-7892.

[4-14] N. Hanada, T. Ichikawa, S. Hino, and H. Fujii, *J. Alloys Compd.* **420** (2006)

46-49.

[4-15] Y. Kojima, Y. Kawai, and N. Ohba, *J. Power Sour.* **159** (2006) 81-87.

[4-16] D.J. Siegel, C. Wolverton, and V. Ozolins, *Phys. Rev. B* **76** (2007) 134102(1)-134102-(6).

[4-17] T.J. Marks and J.R. Kolb, *Chem. Rev.* **77** (1977) 263-293.

[4-18] S.J. Hwang, R.C. Bowman Jr., J.W. Reiter, J. Rijssenbeek, G.L. Soloveichik, J.C. Zhao, H. Kabbour, and C.C. Ahn, *J. Phs. Chem. C* **112** (2008) 3164-3169.

[4-19] Y. Nakamori, H. Li, K. Miwa, S. Towata, and S. Orimo, *Mater. Trans.* **47** (2006) 1898-1901.

5 Conclusion

In order to obtain the guiding principles of material design for the *M*-B-H systems, hydrogen storage properties of the $M'H_m$-$M(BH_4)_n$ mixtures (M' = Mg and Ca, M = Li and Zn) and the hydrogenated MH_n-$M'B_m$ mixtures (M = Li and Sc, M' = Mg and Ca) by using a milling technique were investigated by TG-DTA-MS, p-DSC, FT-IR, XRD, SR-XRD, Raman scattering, and XAS. The results obtained in this study are summarized as follows:

(1) The condition of forming $M'B_m$ was examined in order to understand how $M'B_m$ is formed during the dehydrogenation process of the $M'H_m$-$M(BH_4)_n$ mixtures. The thermal analyses of the MgH_2-$LiBH_4$ mixture and each composition were performed by TG-DTA and p-DSC under an inert gas flow and ~0.5 MPa H_2 pressure conditions in order to investigate these dehydrogenation processes. In the case of the MgH_2-$LiBH_4$ mixture, phase transition, the melting phenomenon of $LiBH_4$, and the decomposition reaction of MgH_2 proceeded below 400 °C regardless of the atmosphere. After that, the decomposition reaction of $LiBH_4$ proceeded above 400 °C under the inert gas flow, while no reaction occurred below 450 °C under ~0.5 MPa H_2. However, the result of the isothermal measurement at 450 °C under ~0.5 MPa H_2 showed that the small endothermic peak was observed. The results of the XRD measurements showed that the peaks of MgB_2 and LiH were observed in the profile after heating up to 450 °C under ~0.5 MPa H_2, while under an inert gas flow, the peaks of Mg and LiH were observed in the profile of the MgH_2-$LiBH_4$ mixture after heating up to 450 °C. From the above results, it was clarified that Mg

reacted with $LiBH_4$ to form MgB_2 during the isothermal measurement at 450 °C by the solid-liquid reaction. From thermodynamic point of view, it was deduced that the presence of hydrogen changes the reaction path into the reaction to form MgB_2 from Mg and $LiBH_4$ by suppressing the decomposition reaction of $LiBH_4$. This reason can be understood because a diffusion of B atom is accelerated by the existence of the liquid phase of $LiBH_4$.

In the case of the CaH_2-$LiBH_4$ mixture, the phase transition and the melting phenomenon of $LiBH_4$, were observed regardless of the atmosphere. After that, an endothermic profile was observed above 400 °C under an inert gas condition, while no peak was observed below 440 °C under ~0.5 MPa H_2 in the closed system. However, an endothermic peak was observed in the profile of the isothermal measurement at 450 °C under ~0.5 MPa H_2. After heating up to 450 °C under ~0.5 MPa of hydrogen pressure, CaB_6 peaks were observed in the XRD profile, while under an inert gas flow condition, CaH_2 and LiH peaks were observed after heating up to 450 °C. From these results, it was found that the CaB_6 was formed during the isothermal measurement at 450 °C under ~0.5 MPa of hydrogen pressure by reacting between CaH_2 and $LiBH_4$ by solid-liquid reaction. It was deduced that existence of hydrogen changes the reaction path into the reaction to form CaB_6 from CaH_2 and $LiBH_4$ by suppressing the decomposition reaction of $LiBH_4$ as well as the case of the MgH_2-$LiBH_4$ mixture.

In the case of the the MgH_m-$Zn(BH_4)_2$ system (m = 0 and 2), the gas emission properties of the two-layered MgH_m-$Zn(BH_4)_2$ samples (m = 0 and 2), in which a large amount of activated MgH_m were put directly on $Zn(BH_4)_2$, showed that the B_2H_6 emission was significantly suppressed in both samples compared with that of

$Zn(BH)_2$ itself. In the case of the hand-milled MgH_m-$Zn(BH_4)_2$ samples by agate mortar, the B_2H_6 emission and its desorption temperatures decreased compared with those of $Zn(BH_4)_2$ itself. From these results, it was found that MgH_m quickly reacted with emitted B_2H_6 on the surface of $Zn(BH_4)_2$ and the hydrogen desorption reaction of hand-milled MgH_m-$Zn(BH_4)_2$ samples were accelerated. However, these reactions were exothermic in contrast to endothermic decomposition reaction of $Zn(BH_4)_2$, indicating that the rehydrogenation reaction of this system would not proceed from the thermodynamic point of view. Moreover, no MgB_2 peak was observed in the XRD and Raman profiles after heating of the hand-milled MgH_n-$Zn(BH_4)_2$ mixtures although B-H vibrational modes were observed by FT-IR. Thus, it was clarified that MgB_2 was not formed by the reaction between MgH_m and $Zn(BH_4)_2$ via gas-solid reaction.

(2) The hydrogen storage properties of the MH_m-$M'B_m$ mixtures by milling under hydrogen pressure were investigated by TG-MS, FT-IR, and SR-XRD and XAS in order to examine the milling effect on the M-B-H systems during hydrogenation reaction. Hydrogen storage properties of the MH_n-$M'B_m$ mixtures (M = Li and Sc, M' = Mg and Ca) hydrogenated at room temperature by the milling method were investigated by TG-MS, FT-IR, SR-XRD, and XAS. As a result of these investigations, all the as-milled MH_n-$M'B_m$ mixtures revealed different MS profiles from that of the as-milled $M'B_m$ and their weight losses with the hydrogen desorption were larger than that of the as-milled $M'B_m$. These results indicated that MH_n would have an ability to provide hydrogen to $M'B_m$. For the LiH-$M'B_m$ (M' = Mg and Ca) mixtures, the as-milled LiH-MgB_2 and the as-milled LiH-CaB_6

mixtures desorbed ~3.6 mass% and ~1.9 mass% of hydrogen, but their weight losses did not reach the theoretical weight losses of 11.4 mass% and 10.5 mass%, respectively if we assume the following reactions: $2LiH + MgB_2 + 4H_2 \rightarrow MgH_2 + 2LiBH_4$ and $6LiH + CaB_2 + 10H_2 \rightarrow CaH_2 + 6LiBH_4$. This result indicated that the hydrogenation reactions of them were not completed and prolonged milling time and/or higher temperature are needed to obtain the more hydrogenated products. The as-milled ScH_2-MgB_2 and the as-milled ScH_2-CaB_6 mixtures desorbed ~3.4 mass% and ~1.8 mass% of hydrogen at ~240 °C and at ~250 °C, respectively. In the FT-IR spectra, B-H vibrational modes were observed in the as-milled samples and disappeared after the dehydrogenation reaction, indicating that hydrogen was stored in the as-milled ScH_2-$M'B_m$ mixtures by forming the B-H bonding, and released this hydrogen by heating. In the SR-XRD profiles, the peaks corresponding to ScB_2 were observed in both the samples before and after the dehydrogenation reaction. In addition, new peaks appeared at low angle in the SR-XRD profile of the as-milled ScH_2-CaB_6 mixture and these peaks disappeared after the dehydrogenation reaction, indicating that these peaks could correspond to the hydrogenated state of the ScH_2-CaB_6 mixture. On the other hand, weak peak appeared at low angle in the SR-XRD profile of the as-milled ScH_2-MgB_2 mixture and grew up after the dehydrogenation reaction, indicating that this peak corresponds to Mg-related compound. The XAS results showed that all the samples of the as-milled ScH_2-$M'B_m$ mixtures before and after the dehydrogenation reaction had almost the same profiles in Sc *K*-edge XANES and EXAFS and their EXAFS profiles were close to that of ScB_2. This result agrees well with the SR-XRD results. Furthermore, Ca *K*-edge XANES and EXAFS profile of the as-milled ScH_2-CaB_6

mixture was obviously different from dehydrogenated sample. This result indicated that Ca-related compound desorbed hydrogen. From the above results, it was clarified that ScB_2 and "*M*-B-H" compounds (*M* = Mg and Ca) were generated during hydrogenation reaction by milling the ScH_2-*M*'B_m mixtures at room temperature. It was suggested that hydrogen desorbed from B-H bonding in the "*M*-B-H" compounds, which does not react with ScB_2. Finally, from above results, it is suggested that MH_n would have an ability to provide hydrogen to *M*'B_m and hydrogen is stored in the MH_n-*M*'B_m mixture by forming B-H bonding during milling under hydrogen pressure.

公表論文

[1] Thermal analysis on the Li-Mg-B-H systems

Tessui Nakagawa, Takayuki Ichikawa, Nobuko Hanada, Yoshitsugu Kojima, and Hironobu Fujii

Journal of Alloys and Compounds, **446-447**, 306-309 (2007).

[2] Gas emission properties of the MgH_x-$Zn(BH_4)_2$ systems

Tessui Nakagawa, Takayuki Ichikawa, Yoshitsugu Kojima, and Hironobu Fujii

Matreials Transactions, **48**, 556-559 (2007).